Multiscale mechanics of soft tissues

Florent Wijanto

université PARIS-SACLAY

NNT : 2019SACLX093

Thèse de doctorat

Multi-scale mechanics of soft tissues

Thèse de doctorat de l'Université Paris-Saclay
préparée à l'École polytechnique

École doctorale n°573 Interfaces
Approches interdisciplinaires: Fondements, Application et Innovations (Interfaces)
Spécialité de doctorat : Physique

Thèse présentée et soutenue à Palaiseau, le 17 Décembre 2019, par

FLORENT WIJANTO

Composition du Jury :

Atef Asnacios Professeur, Université Paris Diderot (LMSC)	Président
Martin Lenz Directeur de Recherche, Université Paris Sud (LPTMS)	Rapporteur
Claude Verdier Directeur de Recherche, Université Grenoble Alpes (LiPhy)	Rapporteur
Hervé Turlier Directeur de Recherche, Collège de France (CIRB)	Examinateur
Jean-Marc Allain Professeur, Ecole Polytechnique (LMS)	Directeur de thèse
Matthieu Caruel Maître de Conférences, Université Paris Est Créteil Val de Marne (MSME)	Co-directeur de thèse

Contents

Acknowledgements

Le nom qui apparaît à l'avant de ce manuscrit est uniquement le mien, mais cette thèse doit beaucoup à la contribution de nombreuses personnes rencontrées ou pas lors de la gestation de ce manuscrit. En premier lieu je tiens à remercier mon directeur de thèse Jean-Marc Allain. Merci pour ses lumières, sa patience et son soutien pendant ces années de thèse, la conclusion de ce manuscrit lui doit beaucoup. Merci aussi à Matthieu Caruel qui a su me guider et m'encourager à travers les nombreuses discussions que nous avons pu avoir. Je tiens également à remercier Dominique Chapelle et Philippe Moireau qui m'ont accueilli au sein de l'équipe M3DISIM et qui directement et indirectement ont permi la réalisation de ce travail dans des conditions matérielles optimales. Cette thèse doit beaucoup également à mes collègues et compagnons de thèse qui ont partagé, encouragé et écouté durant toutes ces années. Merci à vous Barbara, Brenna et Micaela, Ustim, Federica, François et Arthur, Cécile et Nicole. Merci également à Laurent, Alexandre Jouan, Anthony, Anchal, Blandine, Arthur, Jean-Pierre, Frédérique, Othmane, Yanis, Alexandre El-Sabbagh et Nicolas. Votre amitié m'a été précieuse. J'adresse également mes remerciement à toute l'équipe du LMS: Patrick Letallec, Hakim, Alexandra, Christiane, Anna et Valérie. Vous avez rendu mon séjour au LMS des plus agréables. De chaleureux remerciement aussi à l'équipe M3DISIM dans son ensemble: Jean-Sébastien, Alexandre Laurin, Sébastien Impériale, Sébastien Gilles, Martin, Jérôme, Frédérique, Radek, Francesco et Fabrice. Un grand merci également à Peter Baumgartner que j'ai eu le plaisir et l'honneur

d'encadrer durant son stage. J'ai également une pensée pour mes amis dont la chaleureuse bienveillance m'a grandement aidé durant toutes ces années. Merci Rayane et Antoine, Dimitri, Benoît Mauss et Benoît Mahault. Enfin, pour toute la joie et le bonheur que tu m'as apporté et que tu m'apportes toujours, merci Angeliqua.

Résumé

Les réseaux de fibre sont une structure omniprésente dans les tissus biologiques. Ils sont bien souvent présents dans les structures chargées d'assurer un support mécanique à l'organisme en question. En effet, un réseau de fibre offre un compromis intéressant entre la quantité de matière ou la masse de la structure et la résistance mécanique au chargement. On retrouve ces structures aussi bien au niveau macroscopique, où ils sont l'ingrédient principal des tissus mous, qu'au niveau microscopique, en tant que constituants des structures collagèniques ou du cytosquelette. Ainsi, les réseaux de fibres forment des structures très hiérarchisées, où les fibres d'un niveau du réseau forment le réseau d'un niveau inférieur. Au sein des tissus biologiques animaux, la minéralisation du tissu constitue une caractéristique importante de la réponse mécanique du tissu. Les tissus minéralisés, à savoir, les os, exhibent une réponse mécanique dure et cassante, tandis que les tissus non-minéralisés comme la peau ou le tendon affichent une réponse mécanique molle et hyperélastique. Dans ce manuscrit, nous nous concentrons sur la modélisation de tissus mous non-minéralisés, tels que les structures collagèneuses. Alors que les paquets de fibres de collagène constituent un indicateur important du comportement mécanique de la structure, la matrice de tissu conjonctif qui assure l'interconnection du réseau, assure quant à elle des fonctions importantes dans le stockage de l'énergie. Un travail de modélisation réaliste doit donc prendre en compte aussi bien le comportement des fibres que celle de la structure d'interconnection. La réponse mécanique macroscopique des

tissus collagèneux résume les intéractions fibres-matrice. Lors d'un chargement mécanique, le réseau de fibre exhibe une réponse en forme de "J". Cette réponse mécanique peut être classiquement décomposée en trois étapes: le "pied", le "talon" et la phase linéaire. Lors de la première étape, ou le "pied" de la courbe, le réseau peut être déformé sans augmentation significative de la force dans le matériau. Cela correspond au dépliement des ondulations microscopiques au sein du matériau. Lors de la deuxième étape, ou le "talon" de la courbe, les fibrilles de collagène au sein du réseau s'alignent pour suivre la direction de sollicitation du matériau et la distance latérale entre les fibrilles diminue alors. On observe une augmentation exponentielle de la force au sein du réseau. Enfin, lors de la phase linéaire de la sollicitation, les fibrilles de collagène elles-mêmes sont sollicitées, donnant lieu à une réponse raide et linéaire, caractéristique de l'élasticité des fibrilles. En outre, des résultats expérimentaux sondant l'intéraction fibres-matrice suggère l'existence d'un mécanisme de dommage réversible au sein du réseau de fibres collagèneuses. Les structures en réseau de fibre existent aussi bien dans les tissus mous à l'échelle macroscopique, qu'à l'échelle microscopique au sein des structures constitutives des fibrilles de collagène ou bien matérialisé au sein des cellules par le cytosquelette. L'objectif de ce travail de thèse est de proposer un modèle unidimensionnel basé sur la microstructure physique des réseaux de fibres afin d'obtenir une compréhension du comportement mécanique des réseaux de fibres biologiques. Le modèle est basé sur une description de fibres glissant les unes par rapport aux autres et interagissant via des ponts qui se comportent comme des ressorts. Ces ponts peuvent s'attacher et se détacher de manière stochastique avec un taux de détachement qui dépend de la force subie. L'attachement et le détachement dynamique des têtes d'intéraction, lorsqu'elles sont sommées, donne les propriétés mécanique à l'échelle de la fibre, à travers les variables telles que la vitesse de glissement de la fibre ou la force totale ressentie par la fibre. Comparé aux modélisations existantes, notre travail met en jeu une configuration en

glissement dynamique des fibres, ainsi que des sites d'attachement discrets ne permettant l'attachement qu'à des endroits localisés de la fibre. Ainsi, nous faisons un choix de modélisation qui implique un potentiel harmonique pour l'attachement des têtes et une localisation spatiale finie de ce potentiel, qui donne naissance à une zone de détachement forcé en dehors de la localisation du site. Le détachement des ponts est basé sur la diffusion thermique hors d'un puit de potentiel suivant la théorie de Kramers. Cette théorie donne un contexte physique à la dynamique du détachement ainsi qu'une dépendance naturelle du détachement au chargement via l'inclinaison du paysage énergétique par la force de chargement. Ainsi, plus le pont d'attachement est chargé, plus la barrière énergétique de sortie est inclinée dans la direction du mouvement. Le taux de détachement est ensuite donné par l'exponentielle de l'opposé de la barrière d'énergie à surmonter. Cette barrière existe dans les deux sens de l'axe du mouvement et donne lieu à deux taux de détachement, qui sont sommés pour obtenir le taux de détachement total du système, qui augmente au fur et à mesure qu'une tête s'éloigne du site d'attachement et qui est infini une fois que la tête est étirée hors de la localisation spatiale du site d'attachement. Ce taux qui est obtenu de la théorie de Kramers est valable tant que le temps mis par la tête pour atteindre l'équilibre est rapide comparé au temps de sortie par la barrière d'énergie, c'est-à-dire que le site d'attachement représente un minimum bien défini de l'énergie du système attaché. Finalement, ces descriptions de l'attachement et du détachement sont appliquées à un système exhibant une fibre face à un enchaînement de sites périodiques. On montre que dans certains cas, on peut appréhender ce système de N têtes face à une infinité de sites d'attachement périodique comme plutôt N systèmes face à un site d'attachement avec des conditions de bord périodiques. Le modèle donne deux modes de contrôle du système : un contrôle à vitesse imposée, appelé système dur, et un contrôle à force imposée, appelé système mou. Notre travail permet également de visualiser le comportement du système à travers une simulation stochastique. Les simulations offrent

deux algorithmes, chacun adapté à la méthode de contrôle du système, en système dur ou mou et respectant la causalité dans chacun des modes. Les résultats de la simulation sont explorés via la visualisation des données sortantes de la simulation, qui servent de support pour l'investigation paramétrique du comportement du modèle et ancrent l'interprétation physique des résultats. En particulier, l'influence de l'espacement des sites d'attachement du système, un point caractéristique du modèle, est examiné. De même, nous explorons l'effet de chargements complexes (transitoires, cycliques, etc.) qui représentent les chargements physiologiques des tissus fibreux.

1 Introduction

1.1 General Introduction

Fibre networks are ubiquitous structures in the make-up of biological tissues. Most organs which appear continuous to the naked eye have an underlying microstructure made of various types of fibre networks. In this work we aim to give a model that accounts for the mechanical properties of structures, which possess a fiber network microstructure. In order to take into account the rearrangement potential of fiber network microstructure, we propose a model with elements capable of bonding and debonding stochastically. We then develop a stochastic simulation scheme to perform simulation of the behaviour of a one-dimensional fibre system. The behaviour of the system under various loading conditions can then be examined.

1.2 Macroscopic Fibre Networks in Biology

In this section, we aim to give the reader an overview of fibrous structures at the tissue level to serve as a biological justification of the design choices made in the fibre network model presented further on. Due to the imperative of the growth process, life structures, both plant and animal, are simultaneously a form—they have a distinct shape and function— and material—they are a constitutive part of a larger structure. This is a way of saying that biological structures are hierarchical in nature [1]. In contrast

with human engineering where construction of strong and stiff structure may employ bulk metals or alloys such as steel, natural structures rely mostly on composite materials, which is where fibre network come into its own offering these properties with relatively low material density.

In the plant realm, wood is one such network, composed of hollowed-out tubes of cellulose as shown on figure 1.1. The tubes themselves are the walls of the plant cells which grow

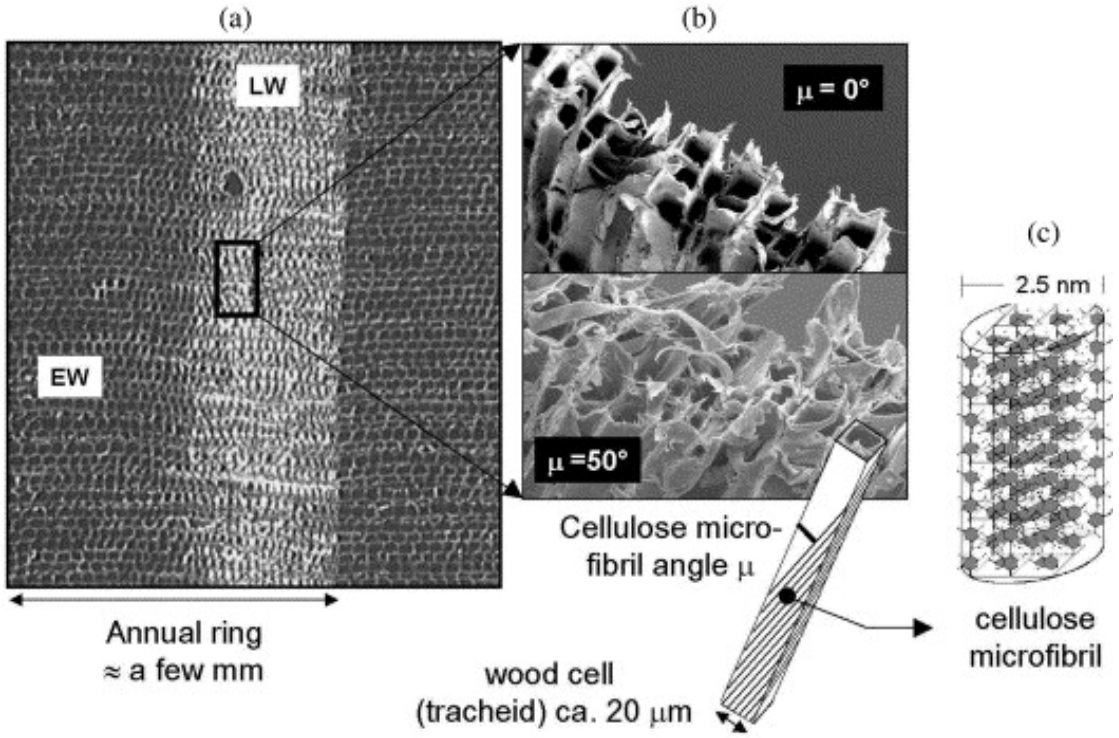

Figure 1.1: Hierarchical structure of spruce wood. (a) Cross-section of the wood showing earlywood (EW) and latewood (LW). Scanning electron microscopy of the fracture surface of spruce wood. Sketch of the crystalline structure of a cellulose micro-fibril. From Fratzl et al. [2].

into the structure, then die and hollow out, leaving the stronger cellular wall behind. These cell walls give the mechanical properties of the wood and are made of a cellulose fibre network, embedded in a hemicellulose and lignin matrix [3]. Wood, viewed at the

centimetre level is therefore a cellular material, where cellular arrangement and dimensions regulate the mechanical properties at the macroscopic level. As an example, wood layers in the trunk is further arranged with an alternating thick and thin annual layers, participating in the orthotropic properties of the wood [1]. Another striking example of macroscopic fibre networks not based on hydrocarbons is the skeleton of glass sponges of the *euplectella* species, shown on figure 1.2. These sponges possess skeletons made

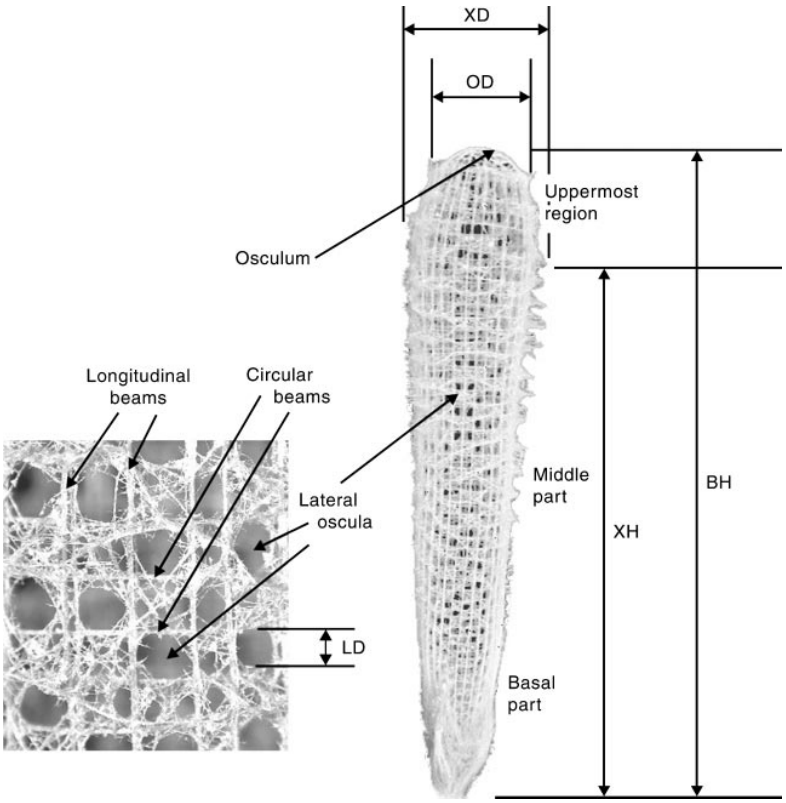

Figure 1.2: Structure of a whole *euplectella oweni* specimen. BH=body height, typically of the order of 100 mm. The zoom on the left hand side shows the network of silica fibres constituting the mechanical support of the sponge body. From Saito et al. [4].

entirely out of siliceous minerals, despite the usual brittleness of these materials. In fact, tests have shown that the natural silica glass skeleton of these animals possess superior

flexibility and toughness compared to man-made glass rods of similar dimensions [5]. This is attributed to the complex reinforcing structure visible on the network of the skeleton [1].

Finally, in the animal realm, we focus on tissues formed by network arrangements of collagen, since this particular family of fibre is ubiquitous in animal tissues. Bone is one such tissue. The hierarchical structure of bones has been described in a number of reviews [6, 7, 8], where bones are generally divided into three groups: long bones such as the femur, short bones such as vertebrae and plate bones such as the skull. The microstructure of these vary with long bones possessing dense mineralized cortical zones and spongy trabecular zones, short bones being mostly composed of trabecular bone whereas plate bones have a succession of plywood-like lamellae. The mineral crystals present in bone tissue are hydroxyapatite, a mineral composed of calcium, phosphate and hydroxyl groups: $Ca_5(PO_4)_3OH$. The variations at the end of the hierarchy scale belie a common structure at the dozens of nanometre fibril scale. Indeed, the trabecular, cortical or lamella structures are themselves various geometrical arrangements and density of organic collagen fibres, interspersed with mineralized particles, as illustrated on figure 1.3. Variations in mineral density and fibril alignment of the same underlying components are responsible for the variety of bone micro and macro-structure, as shown by tomography analyses [9].

Tendons are another example of animal tissue composed of collagen fibres. The underlying collagen fibres constituting tendon tissue are the same as in bone, except that they do not contain mineral elements (with some exceptions such as in turkey leg tendon [10, 11, 12]). The mineralization of the tissue creates a large difference in mechanical response, where mineralized tissue responds in a hard and brittle way, whereas non-mineralized tissue have a soft and hyper-elastic response [13]. In this work, we focus mainly on non-mineralized soft tissues. Tendons are typically composed of type I collagen fibres embedded in an

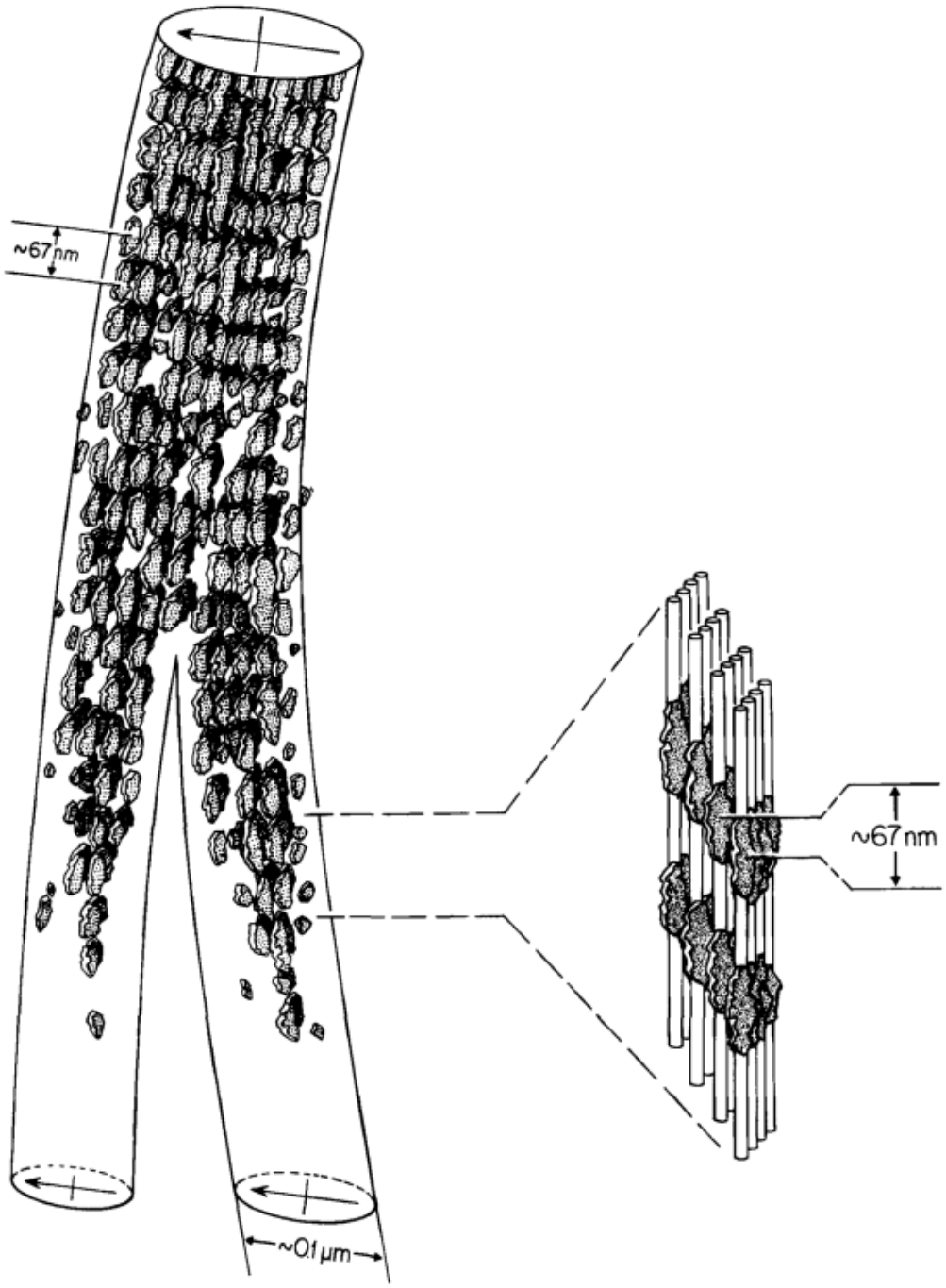

Figure 1.3: Representation of the structural relation between collagen fibres and mineral crystals. At the molecular fibril level, minerals follow fibril alignment and are nucleated at the gap site between two collagen fibrils. From Hodgens et al. [9].

extracellular matrix of hydrated chains of proteoglycans. As shown schematically on figure 1.4, this collagen-proteoglycan composite forms fascicles which themselves form bundles, ultimately constituting the tendon tissue. Tendons play a mechanical support

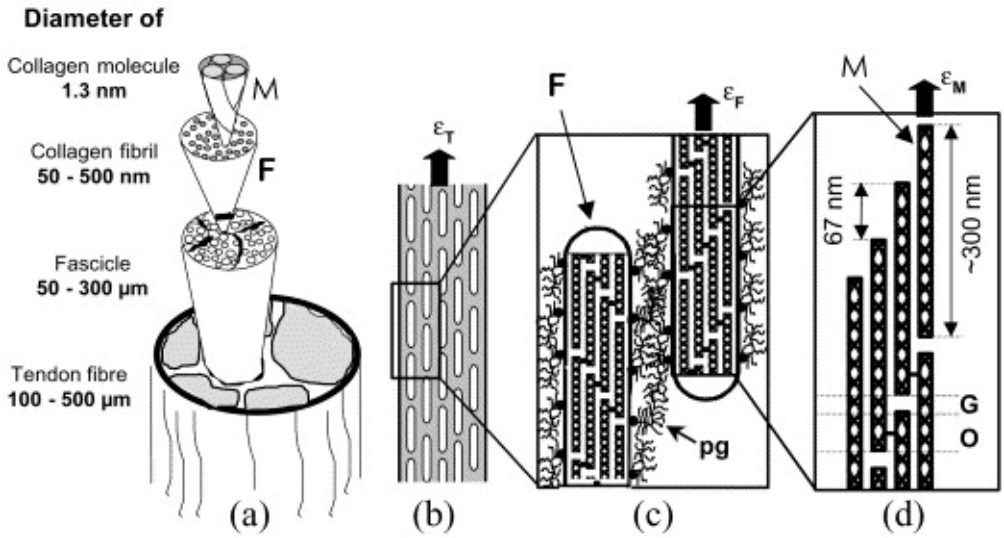

Figure 1.4: (a) Tendon is made of parallel assemblies of collagen fibres (F), itself a triple helical assembly of tropocollagen molecules (M). (b) The tendon fascicle can be considered as a composite material, made of type I collagen fibres embedded in an extracellular matrix, subjected to a total mechanical strain ϵ_T. (c) Part of the total strain is transmitted to the proteoglycan-rich matrix (pg), while the rest ϵ_F is transmitted to the fibrils (F). (d) The triple helix of tropocollagens which constitute a collagen fibril are staggered by an axial spacing of 67 nm. This creates gap zones (G) and overlap zones (O) in the collagen molecule. From Fratzl [2].

role for muscle and bones and also store kinetic energy at various locomotion related zones such as in the Achilles tendon [14]. Furthermore, tendon fibre bundles follow a pronounced alignment along the muscle contraction direction. While the properties of collagen bundles is an important predictor of mechanical behaviour, it has been shown [15]

that the properties of the connective matrix, which allow sliding between collagen fascicles, as shown on figure 1.4 (b), (c) and (d), also play an important role in energy storing. Tendons which have a more active role in locomotion show superior elasticity overall in the connective matrix.

Furthermore, the macroscopic mechanical response of tendon, shown on figure 1.5 can be interpreted with respect of its fibre network microstructure. Three distinct phases

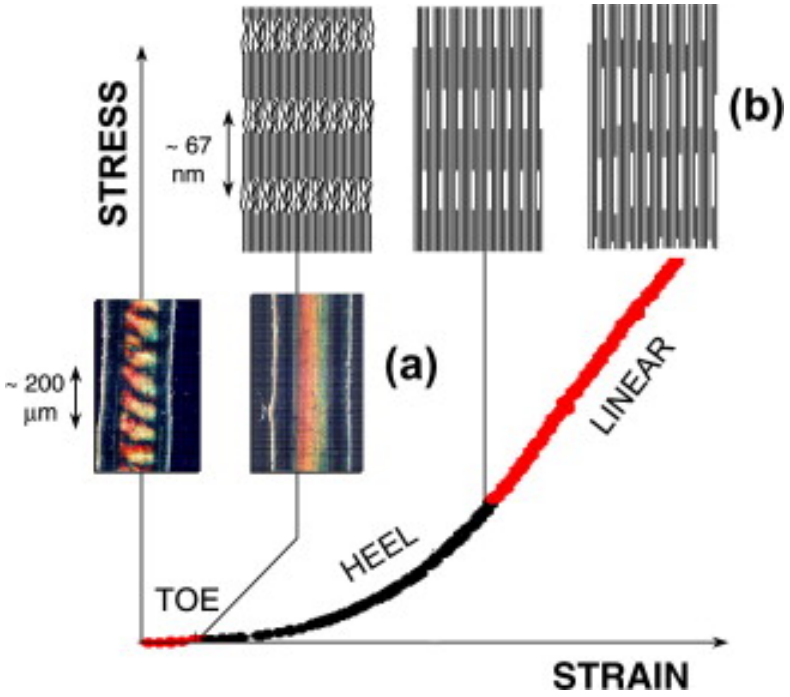

Figure 1.5: Stress strain curve of the tendon. The different response phases are visualized (a) at the microstructure level using polarized light and (b) schematically represented. From Fratzl [1].

of the stress-strain response can be singled out: toe, heel and linear phases [13], with a classical interpretation as follows. In the toe phase, the tendon can be stretched without significant increase in stress; this is the phase where the microscopic folds in the collagen fibres, or "crimps", are stretched out. In the heel phase, the alignment of collagen fibrils

is straightened out and lateral distance between fibrils decreases. Finally, in the linear region, the fibril themselves are solicited mechanically, giving a linear and stiffer response. Furthermore, synchrotron X-ray diffraction experiment of loaded tendon tissue [16] has shown that overall strain in the loaded tissue is greater than the strain observed in individual fibrils, thus implying that significant sliding exists in the extracellular matrix connecting fibrils. Similarly, preconditioning of tendon fibres is associated with a drift of the response curve towards increased strain for the same load [17, 18]. Experiments show that this preconditioning drift is reversible [18]. Together, these experimental observations point toward the existence of a reversible damage mechanism in tendon tissues. Recent ex-vivo multiscale experiments in skin [19] show a similar macroscopic behaviour as in tendon, however the microscopic interpretation of the behaviour curve seems to be different, as fibre re-orientation still seems to occur in the linear region.

Nevertheless, it is clear that relating the behaviour of the microstructure to the macroscopic tissue response is key to a thorough understanding of the mechanical properties of collagenous soft tissues. Ultimately, we've seen that materials as different as wood, bone or tendon, exhibit a remarkably similar underlying microstructure, which is that of a fibre network joined together by a glue-like matrix, which is then loaded under shear. This simple observation is one of the driving idea behind our modelling choices.

1.3 Microscopic Fibre Networks in Biology

1.3.1 Collagen Fibrils

We've seen that cross-linked fibre network models have widespread applicability in various macroscopic biological tissues. Since biological tissues possess a highly hierarchical nature, tissues which are structured as cross-linked fibre networks at the centimetre to millimetre level also often possess the same structure of cross-linked network at the micrometre to

nanometre level as illustrated in the tendon case (see figure 1.4). In fact, tendon is a member of soft collagen rich tissues, together with skin, arteries, cornea, and so on. All these tissues share the property of being made out of collagen fibres, as seen on figure 1.6. Each collagen molecule consists of an amino acid sequence coding for an α-chain and has

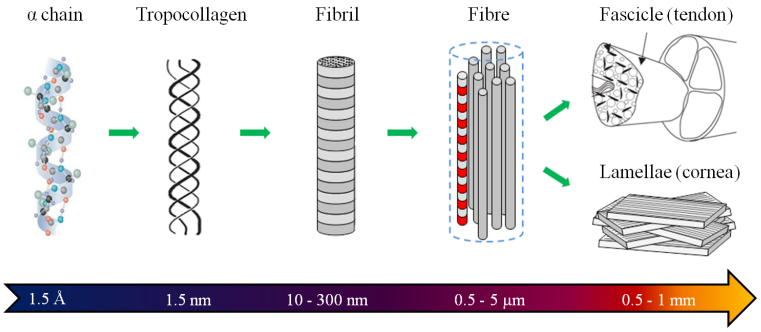

Figure 1.6: Natural hierarchy of the collagen molecule, from the α chain precursor at the nanometre scale, to the millimetric collagen fibre. Adapted from Bancelin [20].

a length of around 300 nm and an approximate diameter of 1.5 nm [21, 22, 23, 16, 24, 25]. The tropocollagen is made of a trimere of collagen, assembled in a triple helical coiled coil, as illustrated on figure 1.6. The collagen molecules constituting the tropocollagen are held together by weak non-covalent interactions between the hydrogen bonds of the α chains. Tropocollagen is then assembled into fibrils at the microscopic scale, which are themselves bundled as collagen fibres which are the building block of soft collagenous tissues.

In order to understand the mechanical properties at the molecular level, simulations of the molecular dynamics of the tropocollagen trimere have been performed [26, 27], taking into account atomistic and chemical interactions between the collagen molecules themselves and the surrounding water solvent. Such simulations can also be tuned to take into account the effect of localized cross-links of varying density between collagen monomeres [28]. Such tuning takes place by adjusting the interatomic potential at the

cross-link location by a factor β to model the increased interaction between the chains. The resulting stress-strain curves of the collagen molecule are given in figure 1.7 and generally show that cross-link density affects the behaviour of the fibre at high strains and causes brittleness in the molecule at high densities.

The assembly of collagenous structures follows a hierarchy, meaning that modelling approaches at the fibril level can be applied at the collagen fibre level, where the junction between molecules is no longer made of covalent cross-links, but rather a soft hydrated extracellular matrix composed in large parts of proteoglycans.

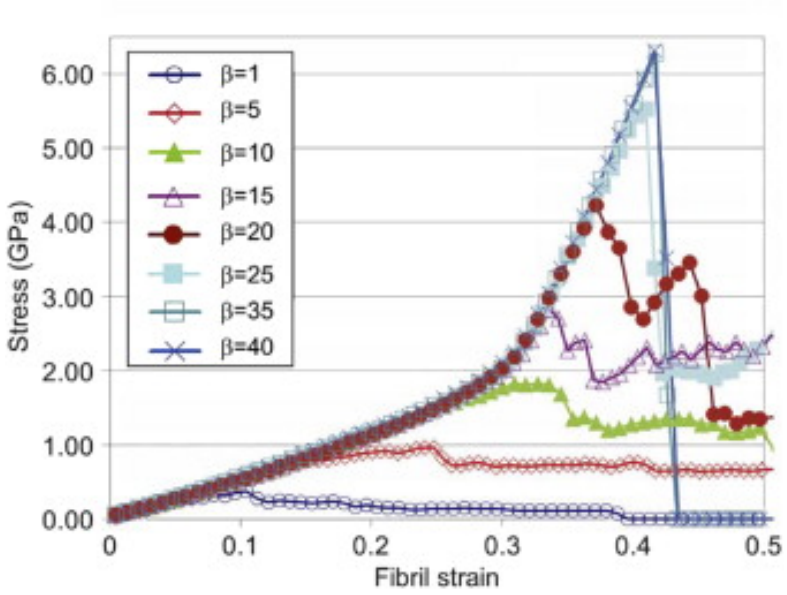

Figure 1.7: Simulated stress versus strain for increasing values of cross-link density β. $\beta = 25$ corresponds to an approximation of two covalent cross-links between two tropocollagen chains. From Buehler [28].

1.3.2 Cytoskeleton Network

Another example of microscopic cross-linked network is the cell cytoskeleton. The cell cytoskeleton is a collection of polymerizing fibres located inside the cell which, in most

cell types, is responsible for much of the cell's mechanical properties, as well as some molecular transport within the cell [29, 30]. While the proteins that constitute the cytoskeleton fibres measure in the nanometre range, the polymerized structures formed by these proteins may span the length of the cell, in the tens of micrometres. Three families are generally distinguished within cytoskeleton fibres as visualised on figure 1.8: the cable-like actin microfilaments, the rope-like intermediate filaments and the tube-like microtubules.

Microtubules, as sketched in figure 1.9, are a head-to-tail assembly of α and β tubulin

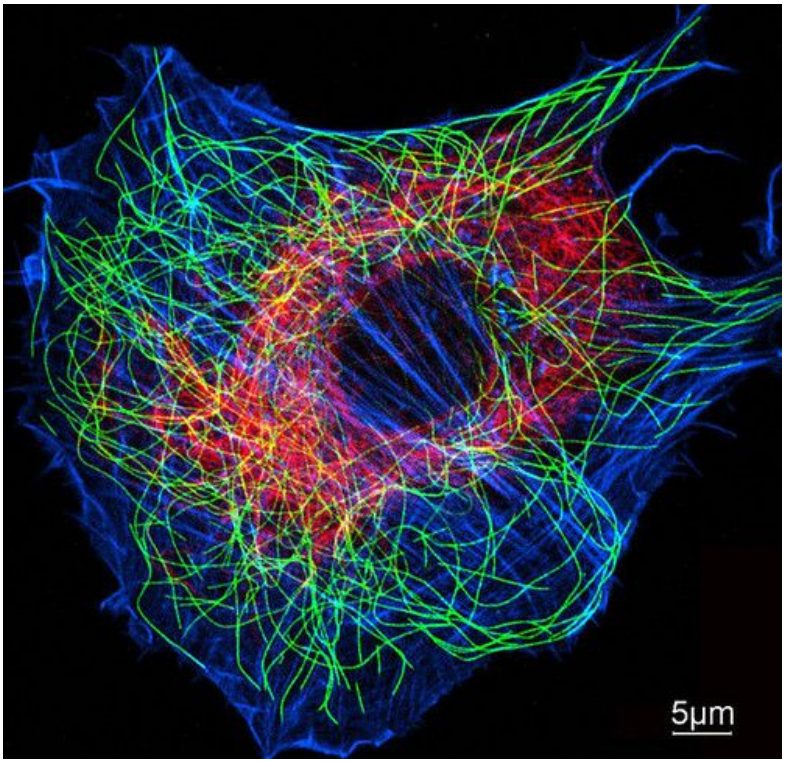

Figure 1.8: Immunofluorescence micrograph of a rat fibroblast cell, stained for microtubules (green), actin microfilaments (blue) and vimentin intermediate filaments (red). From Pollard and Goldman [31].

dimers which is rolled on itself to form a hollow-tube. Microtubules generally originate

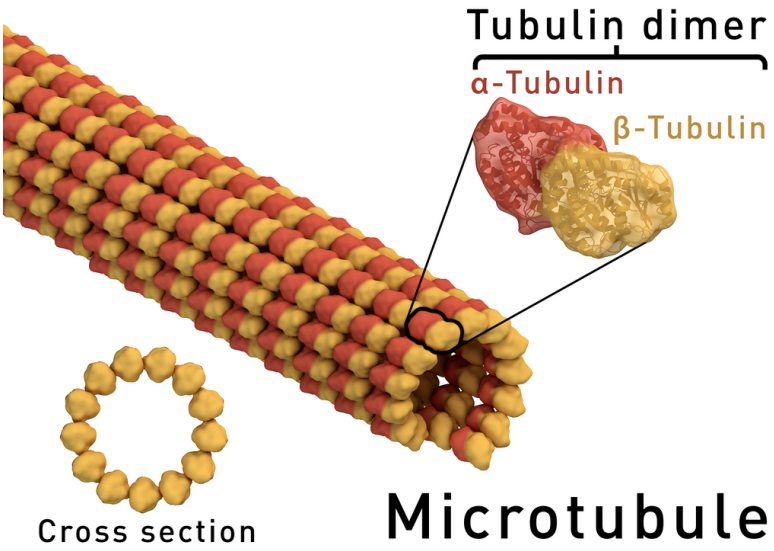

Figure 1.9: Schematic of microtubule structure. Figure by Thomas Splettstoesser, CC-BY-SA 4.0.

from a single nucleating point, the centrosome, and span the length of the cell. They polymerize dynamically during normal cell life and play a role in intracellular vesicle transport and cellular division. A way to gauge the flexibility of polymers is by their persistence length, which is defined as the length beyond which correlation of a tangent vector along the polymer is lost. Since microtubules behave as rigid tubes inside the cell, they exhibit a high persistence length, on the order of the millimeter [29, 30], for a diameter of around 25 nm.

Intermediate filaments comprise a family of proteins which are apolar assemblies of rope-like coiled-coil dimers, as shown on figure 1.10. Intermediate filament families comprise nuclear lamins, vimentin, desmin, keratins and neurofilaments and are generally found in the cytoplasm of cells subjected to mechanical stresses. The diameter of intermediate filaments is around 10 nm. Intermediate filaments exhibit lower persistence length compared to other cytoskeleton fibres. These are in the order of the micrometre [32, 33, 34], indicating that the filaments are flexible inside the cell. Mechanical tests on horsehair,

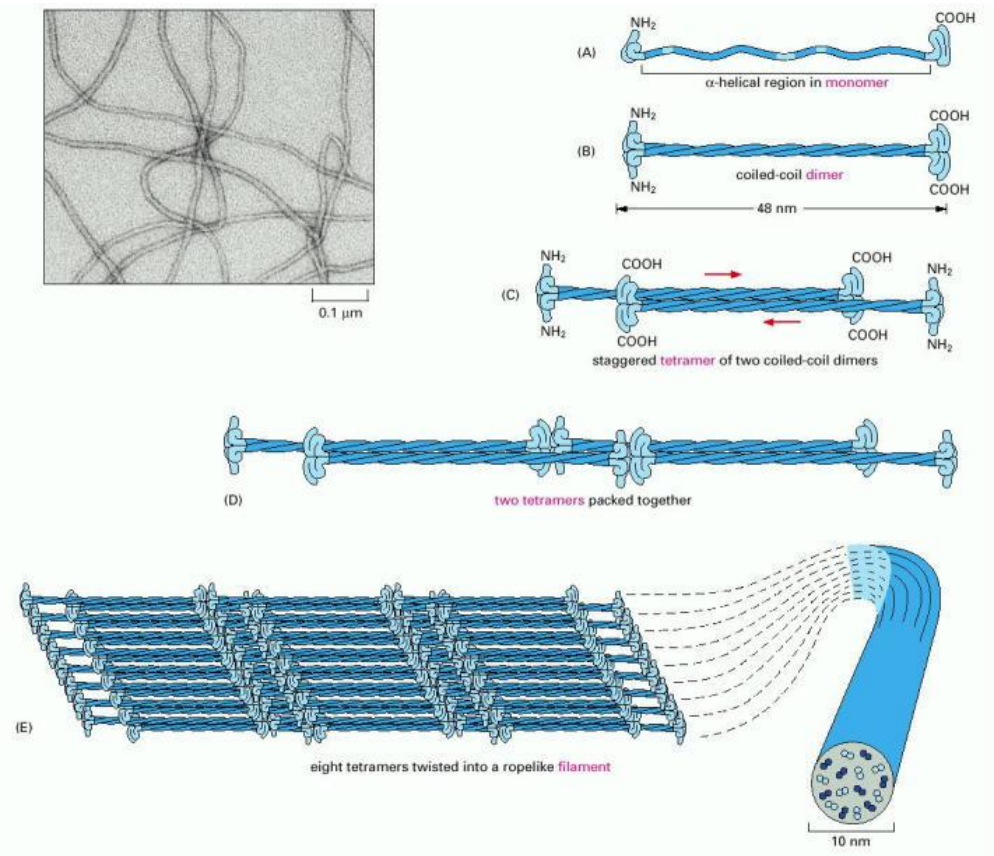

Figure 1.10: Intermediate filament assembly. The monomer shown in (A) assembles into a coiled coil dimer (B) through α-chains side interactions. (C) Dimers then assemble to form staggered tetramers, which (D) bundle up laterally. (E) the final assembly is a packed helical array of 16 dimers. The inset shows an electron micrograph of isolated intermediate filaments. Figure from Alberts et al. [29].

which is composed of keratin, show softening of the connecting matrix, which is able to resist sliding in the transverse direction when dry, but lets intermediate filaments shear and glide past each other when hydrated [35, 30]. A cross-linked fibre model may account for this phenomenon by integrating the matrix properties in the mechanical behaviour of the cross-links.

Actin microfilaments are an assembly of the globular actin protein. The microfilament has extensive monomer-monomer contact between alternating monomers, as well as large rotation (166°), so the actin filament is more appropriately viewed as a double-stranded right hand helix, with a diameter of 6 nm, as shown on figure 1.11. With a persistence

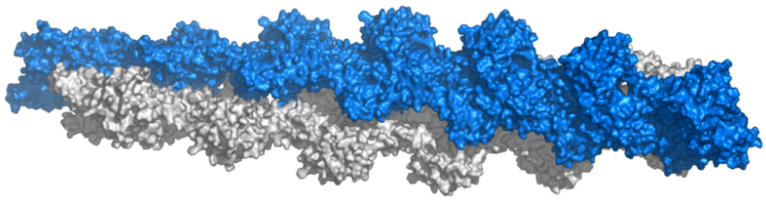

Figure 1.11: Diagram of actin three-dimensional structure, with the two protofilaments shown in separate colours. Figure by Thomas Splettstoesser, CC-BY-SA 3.0.

length of around 10 µm, actin microfilaments which are shorter than the cell size behave like cables: rigid in tension, but able to buckle under compression [36], while longer filaments may bend due to thermal agitation [37]. Within the animal cell, actin microfilaments assemble to form a variety of structures, summarized in figure 1.12, most of which play an important role in cell motility. At the front of the moving cell, a nearly two-dimensional network of branched and cross-linked actin network polymerizes against the membrane, forming the lamellipodium. Aligned parallel bundles of actin make up filopodia which poke out of the lamellipodium and orients cell movement direction. A layer of cross-linked actin coats the inner plasma membrane and plays an important role

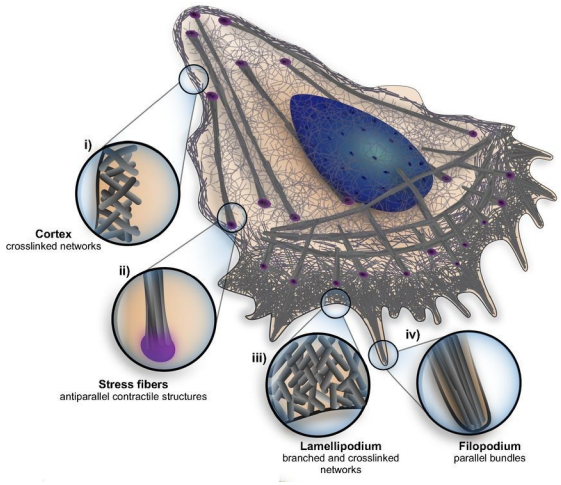

Figure 1.12: Various forms of actin assembly wihin the animal cell. i) Cell cortex, which coats the inner plasma membrane. ii) Contractile stress fibre. iii) Lamellipodium, the leading edge in cell movement. iv) Filopodium protrusion. Adapted from Blanchoin et al. [38].

in maintaining and changing the cell's shape. The interior of the cell itself contains a three-dimensional network of cross-linked actin, along with contractile stress fibres which connect to the exterior substrate at focal adhesion points. We hereby give a description of the four types of assembled actin structure, summarized in figure 1.13. The presence of a complex of 7 proteins, called Arp2/3 (for Actin related protein) causes rapid elongation of actin into a branched network, as seen on figure 1.13A. Indeed, as schematized on figure 1.13A, capping proteins (CP) are needed to inhibit the growth of branches from the Arp2/3 branching site in order to produce a network that is dense enough for force production at the leading edge of the cell [39, 40, 41, 42, 43, 44]. Without these capping proteins, the unchecked growth of branches will tend to form bundles, seen on figure 1.13A which is less optimal than dense branched network for force production. The actin branched network can therefore be viewed as a series of clustered subnetworks which interact with each other via a spring-like structure, visualised in figure 1.13A.

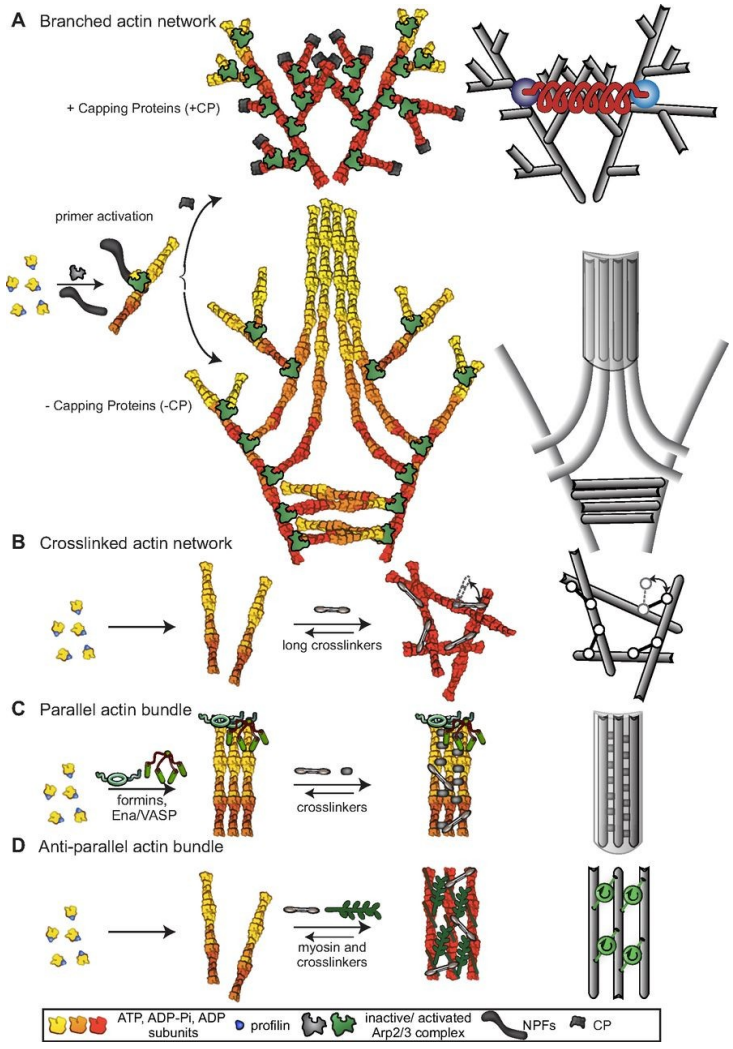

Figure 1.13: Different types of assembled actin structures and their mechanical description on the right, in grey. A: Branching in actin networks occurs at the attachment site of Arp2/3 complexes, which are activated by nucleation promoting factors (NPF). In the presence of capping proteins (+CP), a network with shorter branches is formed, leading to entangled meshes. The entagled subnetworks generate mechanical interactions which can be modelled by a spring (in red) linking the subnetworks together. In the absence of capping proteins (-CP) branches grow longer and can either align into antiparallel bundles or bend and form parallel bundles. These stable parallel bundles then behave as a solid body. B: Long cross-linkers create rigid links in the actin network. The mechanical properties of these networks become dependent of cross-linker kinetics and concentration. C: Short cross-linkers such as formins or ENA/VASP proteins tie unbranched actin filaments together into a parallel bundle. D: Myosin motors assemble anti-parallel bundles into contractile units. From Blanchoin et al. [38].

Another type of actin architecture is the cross-linked network, which is defined as actin filaments cross-linked together by proteins other than the Arp2/3 complex mentioned previously, as in figure 1.13B. Cross-linked networks, like those located in the cell cortex are involved in maintaining cell shape and the mechanical integrity of the cell [45, 46, 47, 48, 49, 50]. As shown on figure 1.13B and C, the length of the cross-linking distance determines the structures formed in the end. Shorter cross-linkers such as fimbrin or fascin will pack actin filaments into tight, parallel bundles, whereas longer cross-linkers like filamin or α-actinin will form networks or bundles, depending on their concentration [51, 52, 53, 54, 55, 56]. Parallel bundles of actin filaments, as shown on figure 1.13C, are present in a number of cellular structures, including filopodia, microvili and hair cell stereocilia [57, 49, 44, 58, 59]. Parallel bundles are made of actin filaments oriented with the same end facing one direction, generally the cell membrane [45]. The cross-linkers hold bundles tightly together but adjacent bundles are allowed to shear with respect to one another, as seen in the case of stereocilia [60]. Anti-parallel bundles also exist within the cell. These bundles, associated with myosin motors, are responsible for the contractile work done by the cell. The resulting contractile units play an important role in cell shaping for cell division and the establishment of stress fibre at the cell-cell and cell-matrix junctions [61, 62, 63, 64, 65, 66, 67]. We've seen that actin microfilaments assemble into either cross-linked structures or bundles. That is to say that the various geometric configurations of actin structures can be modelled by sliding fibres with interacting dynamic cross-links to represent the dynamic reorganisation of actin architectures. Stochastic cross-links are one way to represent the dynamically detaching and reattaching cross-links or branched structures of actin microfilaments.

1.4 Conclusion

We've described how fibre networks represent tissues with complex mechanical properties, be it at the macroscopic scale with collagenous soft tissues or at the microscopic scale with the cytoskeleton. This brings us to investigate the role of cross-links in the load transmission of networks.

2 Review of Modelling Approaches

In this chapter, we present an overview of modelling approaches which serve as a foundation for the work presented herein. We first detail foundational work on static adhesive clusters before examining work done on sliding surfaces.

2.1 Static Adhesive Clusters

The stability of adhesive molecular cluster was first discussed by Bell [68]. A molecular adhesive cluster can be modelled by a series of N_t bonds near the adhesive surface. Figure 2.1 summarizes the configuration of an adhesive cluster.

At anytime t, a number $N(t)$ of the bonds are attached, and a number $N_t - N(t)$ are detached. Each bound bond can break at a rate k_{off} and each detached bond can bind at a rate k_{on}.

When the system is loaded with a force F, it reacts by increasing the rate of unbinding as $k_{off} = k_0 e^{\frac{F}{F_0}}$, where F_0 is a normalizing force of molecular scale (typically in the order of pN) and k_0 is the detachment rate at zero force. Meanwhile the binding rate k_{on} is unaffected. Bell uses this exponential dependence as a phenomenological expression based on fracture mechanics, but this expression can be motivated by the Kramers theory of thermally assisted escape from a metastable state [70, 71, 72, 73]. The idea behind this force dependence is that the force F lowers the height E_b of the transition barrier between a closed and an open bond, as shown on figure 2.2. Since the escape rate from the

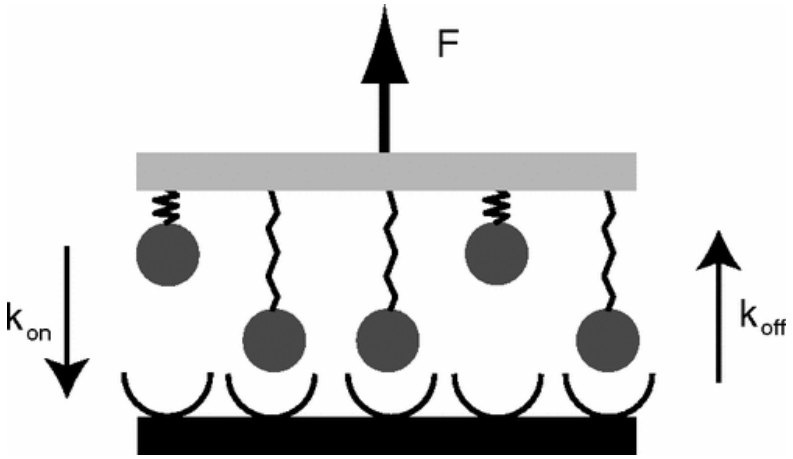

Figure 2.1: Schematic model of an adhesive cluster with $N_t = 5$ bonds capable of attachment and detachment. From Safran and Schwarz [69].

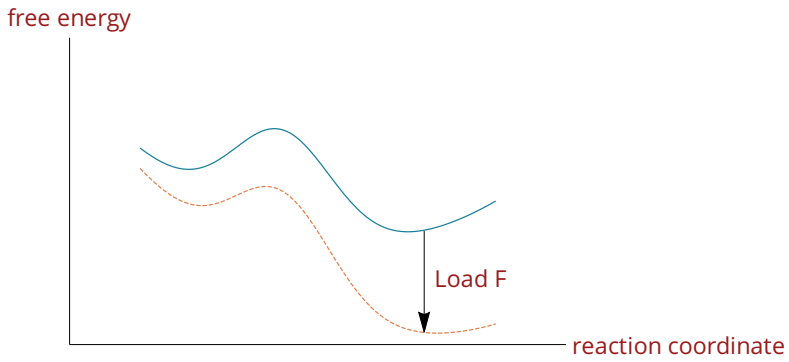

Figure 2.2: Schematic energy profile of a bond which is tilted (dashed line) when an external load F is applied. The resulting energy barrier between the different conformational states is lowered, which increases the transition rate.

closed state scales as $\exp\left(-\frac{E_B}{k_bT}\right)$, where k_BT is the energy scale of thermal fluctuations, adding a force term to the energy changes the escape rate by a factor $\exp\left(\frac{Fx_b}{k_BT}\right)$, where x_b is the distance between the energy minimum and the barrier so that $F_0 = \frac{k_BT}{x_b}$. This viewpoint has been verified through dynamic force microscopy [70].

We now introduce the dimensionless time $\tau = k_0 t$, force $f = \frac{F}{F_0}$ and rebinding rate $\gamma = \frac{k_{on}}{k_0}$. Assuming a constant force f that is equally distributed among all bonds, the following rate equation predicts the number of closed bonds $N(t)$:

$$\frac{dN}{d\tau} = -Ne^{\frac{f}{N}} + \gamma\left(N_t - N\right) . \tag{2.1}$$

While the second term in equation 2.1 is linear in the number closed bonds N, the first term is highly non-linear and leads to some feedback effect on the system. When one bond opens, the remaining closed bonds must share the remaining force applied on the system, thus leading to a cooperative system. A bifurcation analysis of the system shows that the system is unstable with no steady-state solution when the force exceeds a critical value f_c. This critical value occurs when [68]

$$f_c = N_t W\left(\frac{\gamma}{e}\right) , \tag{2.2}$$

where $W(x)$ is the Lambert W function, or sometimes called the product logarithm, defined as the solution to $We^W = x$. Figure 2.3 gives the critical force f_c, plotted as a function of $\gamma = \frac{k_{on}}{k_0}$. As seen on figure 2.3, f_c scales linearly with k_{on} for small values of k_{on}. An adhesion cluster is therefore completely unstable with zero rebinding and its stability grows in proportion with the degree of rebinding. For large values of k_{on}, the scaling becomes slow (less than logarithmic): once k_{on} exceeds k_0, large changes in k_{on} are required to significantly change the stability of the cluster.

Equation 2.1 in Bell's analysis is a mean-field description which doesn't include fluctuation effects, which are expected to be significant in the biological context for small clusters [69].

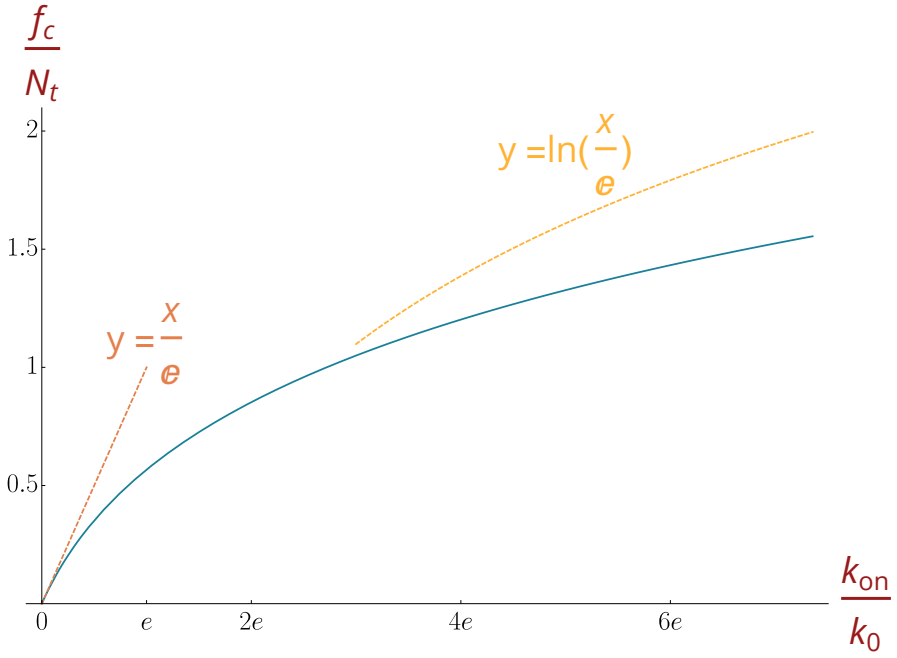

Figure 2.3: Critical force $\frac{f_c}{N_t}$ plotted versus $\gamma = \frac{k_{on}}{k_0}$, for $N_t = 10$, based on equation 2.2.

An extension of Bell's analysis is the one-step master equation in the number i of bonded cross-bridges, with $0 \leq i \leq N_t$. The master equation gives the time evolution of the probability $p_i(t)$ that i bonds are formed at time t [74, 75, 76, 77]:

$$\frac{dp_i}{dt} = r(i+1)\, p_{i+1} + g(i-1)\, p_{i-1} - (r(i) + g(i))\, p_i \,. \tag{2.3}$$

The two positive terms represent the tendency of bonds to enter the state i by dissociation of a bond in state $i+1$ and formation of a new bond in state $i-1$ respectively. The negative term is a loss term representing movement out of state i by dissociation to state $i-1$ and formation of a bond to state $i+1$. The rates corresponding to the Bell model in equation 2.1 are

$$r(i) = ie^{\frac{f}{i}}\,, \quad g(i) = \gamma(N_t - i)\,. \tag{2.4}$$

The Bell equation 2.1 can be recovered from equation 2.3 if one calculates the average number of formed bonds $N = \langle i \rangle$ in the limit of large system size [74, 69] (i.e. a Kramers-

Moyal expansion). Contrary to the deterministic equation 2.1, which predicts infinitely long cluster lifetime below the stability threshold f_c, the stochastic model in equation 2.3 predicts finite lifetime of the cluster for any value of the force. The average lifetime of a cluster with N_t bonds can be calculated from the mean first passage time T for the cluster to stochastically reach the absorbing state $i = 0$ [78]:

$$T = \sum_{i=1}^{N_t} \frac{1}{r\left(i\right)} + \sum_{i=1}^{N_t-1} \sum_{j=i+1}^{N_t} \frac{\prod_{k=j-i}^{j-1} g\left(k\right)}{\prod_{k=j-i}^{j} r\left(k\right)}. \tag{2.5}$$

One of the features of the stochastic model is that it can be used to simulate single trajectories, which are similar to an experimental realisation [69], (see figure 2.4).

The failures seen on figure 2.4 are abrupt due to the cooperativity in the system:

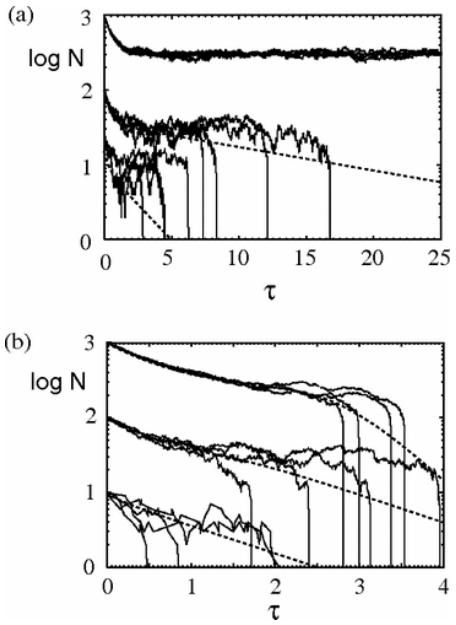

Figure 2.4: Selected trajectories simulated with the stochastic master equation model. (a): Force below threshold $\frac{f}{N_t} = 0.25$. Small clusters are unstable due to fluctuations, whereas larger clusters are stable under force. (b): Force above threshold $\frac{f}{N_t} = 0.3$. All clusters are now unstable. Dotted lines represent fitted $N\left(\tau\right) \approx N_{eq} e^{-a\tau}$. From Safran and Schwarz [69].

once sufficiently many bonds are broken due to random fluctuations, the remaining load on the system sends the cluster in a cascading failure until total detachment occurs. Figure 2.4 (a) shows that small clusters are liable to fail even under the stability threshold due to random fluctuations taking the system into a cascading failure mode. Under the stability threshold, larger clusters are therefore more stable and may remain attached during the whole simulation. Once the system is above the stability threshold, as in figure 2.4 (b), all sizes of clusters are unstable.

The conceptual framework introduced by Bell shows how adhesion clusters can present highly dynamic attachment and detachment and yet be stable up to a maximum force. The model also features high cooperativity which occurs due to the fast redistribution of force in the system when bond dissociation occurs. This cooperative mechanism also takes place in other biological systems such as during force generation in muscles [79, 80] or molecular cargo transport by molecular motors [81, 82]. The elasticity of the system can also be depicted in an explicit continuum mechanics fashion [83, 84, 85, 86], such as illustrated on figure 2.5. These models show that the stress distribution becomes localized at the edges of the adhesion site. This localization of cracks leads to cascading failure from the rim of the adhesion site inward toward the centre. As a result, both very large and very small adhesion clusters are unstable, leading to the existence of an optimum size of adhesion cluster.

2.2 Adhesion of Sliding Surfaces

Physical adhesion occurs not only to static surfaces, but also on surfaces in motion relative to one another. This type of adhesion is especially relevant for fibre networks or under the cellular lamellipodium, where the actin retrograde flow can move binding molecules relative to the corresponding binding site on the extracellular matrix. Figure 2.6

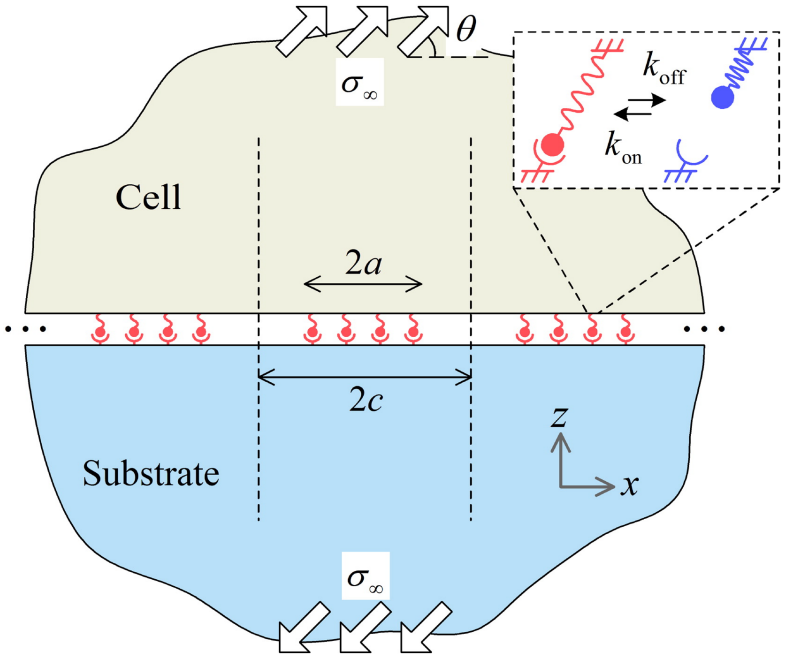

Figure 2.5: Illustration of a periodic array of adhesion clusters between two different elastic media under inclined tensile stress. From Qian et al. [86].

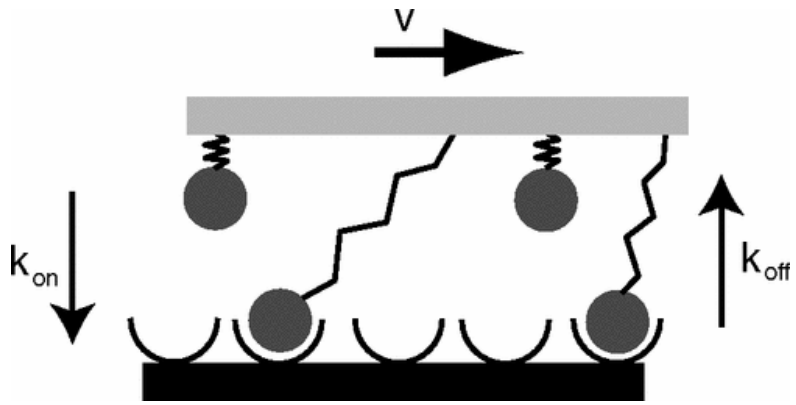

Figure 2.6: Model for an adhesive cluster that bridges two surfaces in motion relative to each other. From Safran and Schwarz [69].

illustrates a minimal model for binding between two moving surfaces [69].

Experimental data shows that a biphasic relation exists between the traction force on the substrate and the flow velocity in the cell [87, 88]. For mature adhesions, force is linearly proportional to flow velocity, while for new adhesion sites an inverse relation between force and flow is observed. Experimentally, the threshold flow value at which the change occurs has been found to be around 10 nm/s and is insensitive to various perturbations in the cell.

As in figure 2.6, the upper surface moves at a velocity v and each bond is modelled as a spring with stiffness κ. Contrary to the stationary cluster, the governing parameter of the model is now the velocity of the moving surface v and not the applied force F. Moreover, each bond is now characterised by its dynamic elongation x, in addition to being able to attach and detach stochastically. The elongation x increases with time for every attached bond due to the moving surface. The probability that a bond is attached $p_b\,(x,t)$ is therefore a function of both time and elongation of the bond. The overall probability of a bond to be attached is

$$P_b\,(t) = \int_{-\infty}^{+\infty} p_b\,(x,t)\,dx\,. \tag{2.6}$$

From normalisation we also get that the unbinding probability p_u is

$$p_u\,(x,t) = 1 - P_b\,(t)\ . \tag{2.7}$$

For harmonic springs, the average traction on the surface is given by the first moment of $p_b\,(x,t)$:

$$F_T = N_t \kappa \int_{-\infty}^{+\infty} p_b x dx\,. \tag{2.8}$$

Regarding the evolution equation, an additional convective derivative term is present to account for the change in extension due to the moving surface. The evolution equation thus reads [89, 69]:

$$\frac{\partial p_b}{\partial t} + v\frac{\partial p_b}{\partial x} = p_u k_{on} - p_b k_{off}\,. \tag{2.9}$$

The master equation can then be solved at steady-state either analytically [90, 91] or by numerical integration at steady-state [89]. Using the solution of the master equation 2.9 to calculate the force applied on the system through equation 2.8, the force velocity diagram of the system can be plotted, which gives the response of the system as a function of the input velocity v. Models adopting this framework [89, 91, 69, 90] reproduce the biphasic force-velocity curve obtained from experiments [88]. Figure 2.7 shows such a biphasic

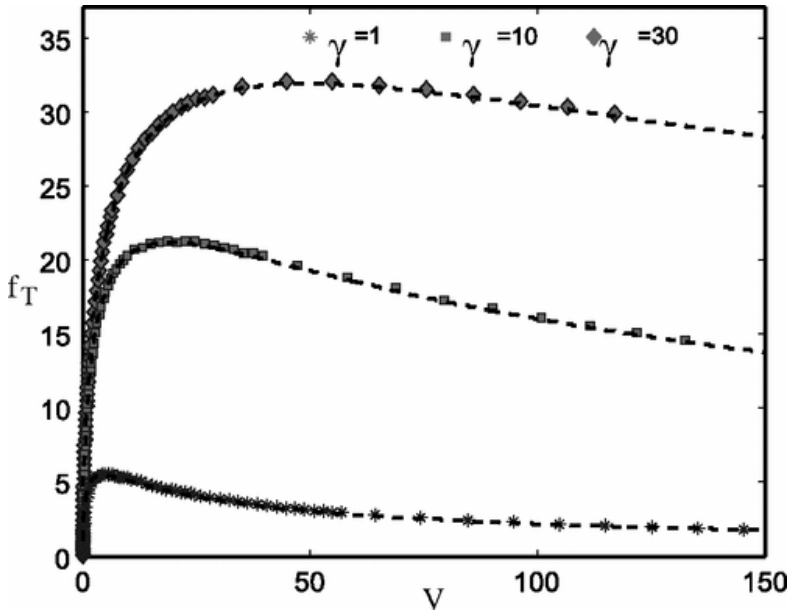

Figure 2.7: Force-velocity relation between the dimensionless traction force f_T and dimensionless flow V predicted by the minimal model for $N_t = 25$. Dashed line is the analytic steady-state solution and symbols represent the result of the stochastic simulations. From Safran and Schwarz [69].

force-velocity relation. One can see the first phase at low velocity where the system load f_T increases linearly with the velocity up to a maximum value after which the second phase begins, where f_T decays with applied V.

A similar concept of molecular friction, as modelled by transient stochastic linkers, has been explored before in a non-biological context [92, 93]. More recently, this stochastic

model has been implemented to describe biological adhesion [94, 95, 96]. Specifically, these models describe the adhesion of actin filaments to the underlying substrate. The presence of actin retrograde flow inside the lamellipodium and lamella of the cell is the mechanism which introduces the sliding velocity between the substrate and the actin filament. Besides the biphasic force-velocity relationship, these model introduce two regimes for the dynamics of the system. The first regime which occurs at low-velocity is called *frictional slippage* where the actin filament slides with dynamic friction. During frictional slippage, there exists a quasi-linear relation between sliding velocity and force exerted on the substrate. The second regime which occurs at higher velocity is the *stick-slip* regime. In this regime, the force increases cyclically, with periods of stable loading, then failure leading to an abrupt decrease of the force, then loading again, and so on. The occurrence of these two regimes has been verified experimentally in the cell lamellipodium [95].

The view of adhesion clusters can be extended to include the role of elasticity of the anchoring bodies. This element finds its importance because cells are responsive to changes of both cellular and environmental stiffness, mainly by changing the stability of its adhesion sites. In particular, Sens [96] showed that by incorporating the elasticity of the substrate into the adhesion system, cells can sense the rigidity of the adhesion substrate. This is due to the fact that in a certain regime of actin flow, traction force on the substrate becomes maximal for a finite value of the substrate modulus E^*. Once the substrate becomes stiffer than E^*, although the force exerted per linker increases, the bound fraction of cross-bridges goes down, causing an effective decrease in traction force. The models described thus far all exhibit a control in velocity of the system, also called a hard device. That is to say, the system reacts in response to a fibre sliding at a fixed velocity. However, the system may also be driven in load, as a soft device. The soft device exhibits a fixed total load and will slide to accommodate changes in the

attachment/detachment configuration of the system. The key difference in the soft device lies in the coupling of all the cross-bridges in the system. Indeed, whereas in the hard device cross-bridge heads can be considered independently, in the soft device, when one head detaches or attaches, it impacts all attached heads by shifting the total load in the system. The sliding of the fibre to return to the imposed total load is therefore felt by all attached heads and is the source of the coupling between all heads. This increases the cooperative effects in the system by recreating a mean-field interaction between heads. The impact of soft versus hard device is explored in muscle systems in the work of Caruel et al. [97, 98, 99].

In closing, the fundamental work modelling surfaces sliding with respect to one another has been laid, but some outstanding questions remain. In the following work, we propose a fibre model, with the following features. The model will present a one-dimensional system of two fibres sliding with respect to one another, with spring-like cross-bridges ensuring the interaction between the two fibres. The cross-bridges are able to attach and detach stochastically, with a load dependent detachment rate similar to the Bell cluster models discussed previously. On the attachment side, the model will explore an area which is not comprehensively discussed in previous models: the attachment to binding sites. Indeed, our model will include periodic binding sites, where cross-bridges will be able to attach, with an attachment rate dependent upon the distance between a cross-bridge and a binding site. Next, our model will be able to explore experiments where the driving parameter is the velocity of the fibre, as in the models described previously, but also the total load of the system, which is a configuration seldom explored in the previously mentioned models. Finally, the model will be put through a more complex loading path, such as a cyclic loading to further give insight into the mechanical behaviour of the system.

3 Stochastic Model

In this chapter we will present the analytical basis of the sliding fibre model. In particular, we start by describing the attachment and detachment scenario, first to a single binding site, then to an array of periodical binding sites. Two versions of the model have been developped: the initial one which was used for our first simulations and a corrected one which satisfies the detailed balance.

3.1 System Description

In order to capture the essential behaviour of a fibre network, we model the interaction between two rigid fibres in one dimension, sliding with respect to one another. A fibre has binding sites along its length, to which elastic spring-like bonds can attach and detach probabilistically based on the load it is supporting. The position of a single bond can be tracked by the position $\widetilde{\sigma}$ of its anchor point to the fibre and the position $\widetilde{y}$ of its head with respect to an arbitrary origin point, as shown on figure 3.1. When summed together, the dynamical attachment and detachment of single bonds, described below, give the mechanical properties at level of the fibres, such as sliding velocity $\widetilde{v}$ or total load $\widetilde{F}$.

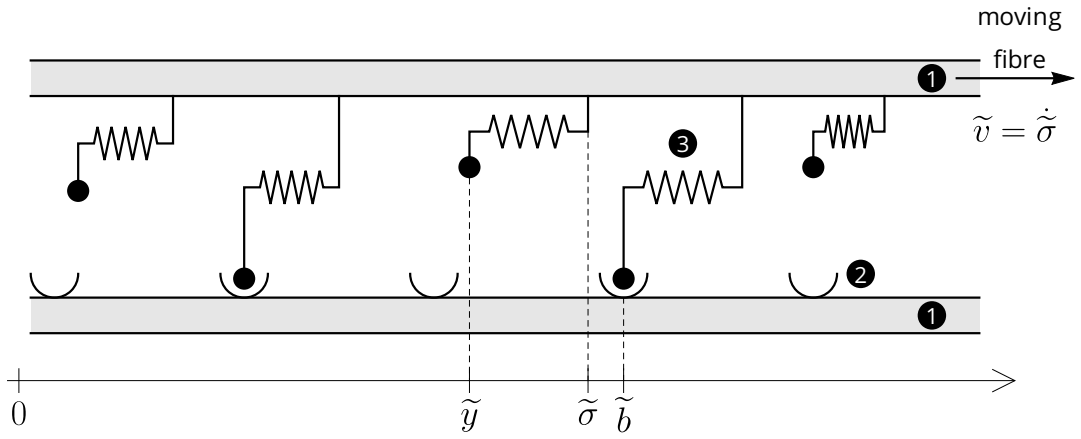

Figure 3.1: Schematics of interacting fibre system. ❶ : Rigid fibre ❷ : Binding site ❸ : Spring-like bond

3.2 Attached Bond

A bond attachment can be thought of as the interaction between the head of the bond at position $\widetilde{y}$ and the binding potential $\widetilde{V}_{bind}$ of the site. As a modelling choice, we assume that binding sites have a set spatial extension $\widetilde{\delta}$ and prescribe the shape of $\widetilde{V}_{bind}$ to be that of a harmonic potential with a stiffness parameter $\widetilde{\kappa}$. As shown on figure 3.2, this limited spatial extension of the site means that there is a zone of forced detachment outside of the binding zone. An attached head thus necessarily has a position $\widetilde{y}$ within $\frac{\widetilde{\delta}}{2}$ of a binding site, i. e. $\left|\widetilde{y} - \widetilde{b}\right| \leq \frac{\widetilde{\delta}}{2}$. The binding potential of a site in position $\widetilde{b}$ is therefore expressed as

$$\begin{cases} \widetilde{V}_{bind}\left(\widetilde{y}, \widetilde{b}\right) = \frac{1}{2}\widetilde{\kappa}\left(\widetilde{y} - \widetilde{b}\right)^2 + \widetilde{V}_0 & \text{if } \left|\widetilde{y} - \widetilde{b}\right| \leq \frac{\widetilde{\delta}}{2}\,, \\ \widetilde{V}_{bind}\left(\widetilde{y}, \widetilde{b}\right) \text{ is not defined} & \text{if } \left|\widetilde{y} - \widetilde{b}\right| > \frac{\widetilde{\delta}}{2}\,. \end{cases} \tag{3.1}$$

Next, an attached head generates loading on the fibre because it is connected to the anchor point at position $\widetilde{\sigma}$ via a spring with stiffness $\widetilde{K}$ and rest length $\widetilde{l}_0$. This spring, shown on figure 3.3, generates a load on the head which is responsible for its possible detachment within the binding zone. The spring potential $\widetilde{V}_{spring}$ is[1]

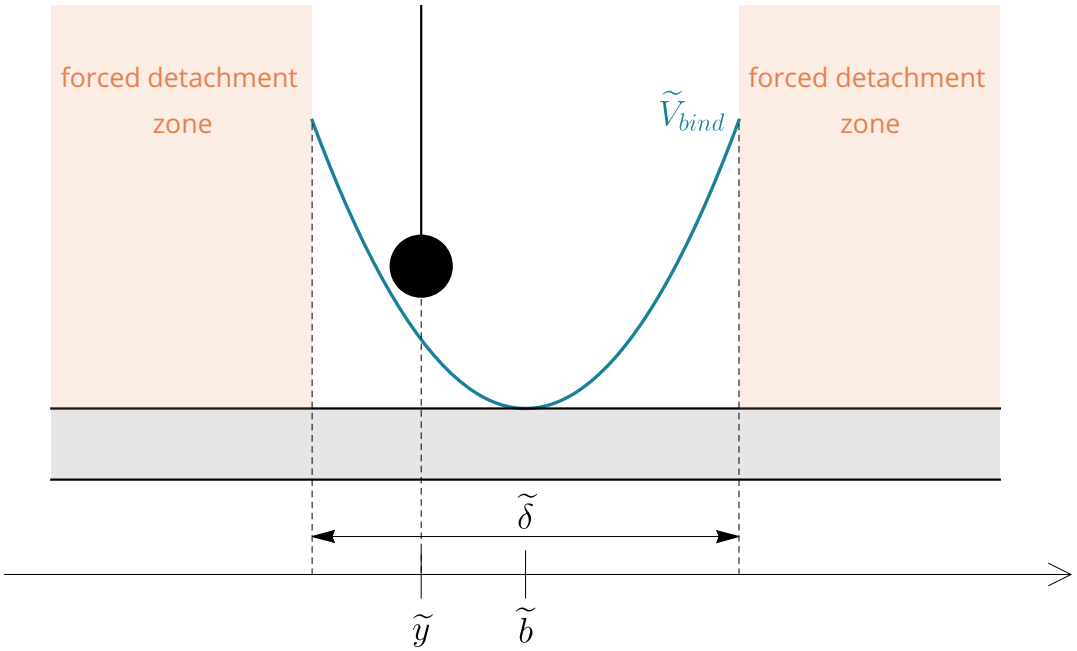

Figure 3.2: Potential of a binding site at position $\widetilde{b}$ with a spatial extension $\widetilde{\delta}$, interacting with a particle in $\widetilde{y}$

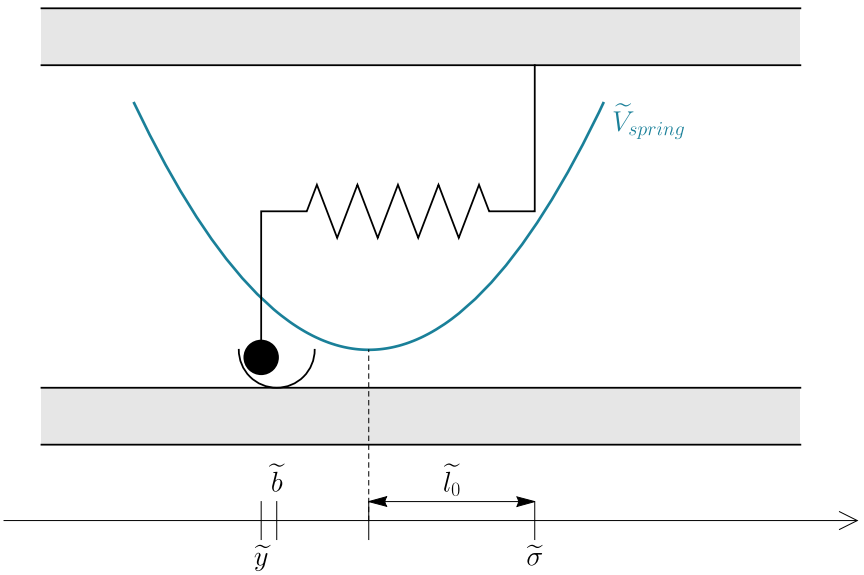

Figure 3.3: Potential of the bond spring, for a head in $\widetilde{y}$ attached in the binding site $\widetilde{b}$.

$$\widetilde{V}_{spring}\left(\widetilde{\sigma},\widetilde{y}\right)=\frac{1}{2}\widetilde{K}\left(\widetilde{\sigma}-\widetilde{y}-\widetilde{l}_0\right)^2 . \tag{3.2}$$

The total energy $\widetilde{E}$ of the attached head is therefore:

$$\begin{aligned}\widetilde{E}(\widetilde{\sigma},\widetilde{y},\widetilde{b}) &= \widetilde{V}_{spring}\left(\widetilde{\sigma},\widetilde{y}\right)+\widetilde{V}_{bind}\left(\widetilde{y},\widetilde{b}\right)\\ &= \frac{1}{2}\widetilde{K}\left(\widetilde{\sigma}-\widetilde{y}-\widetilde{l}_0\right)^2+\frac{1}{2}\widetilde{\kappa}\left(\widetilde{y}-\widetilde{b}\right)^2+\widetilde{V}_0 .\end{aligned} \tag{3.3}$$

The total energy of the system is illustrated in figure 3.4. The more stretched the bond

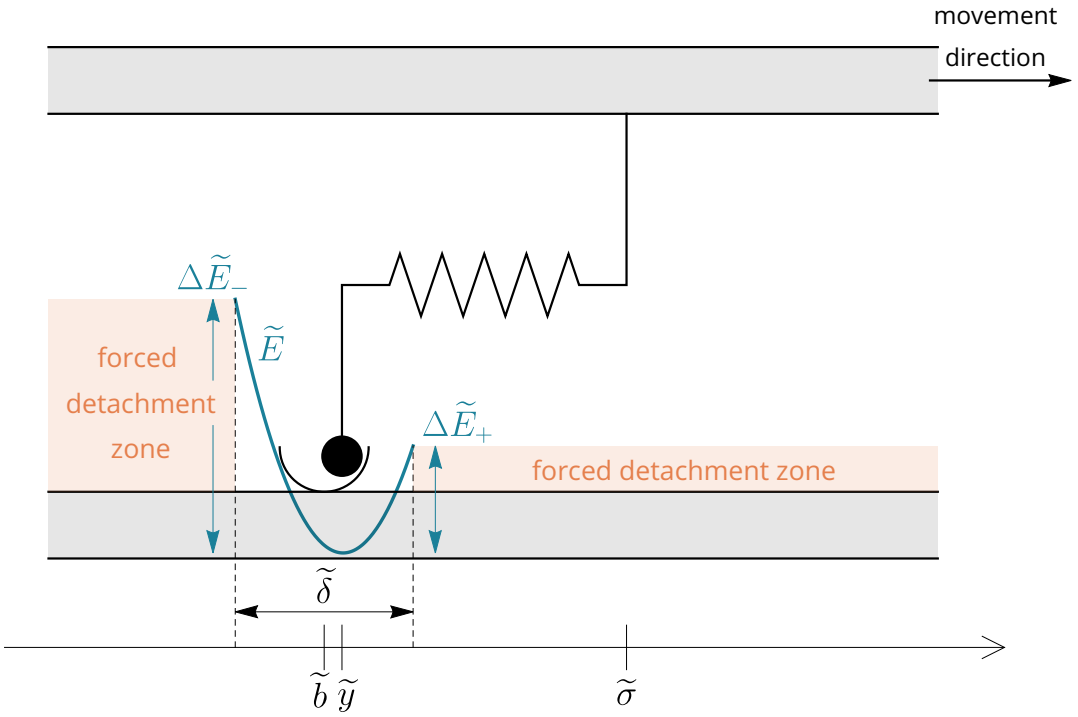

Figure 3.4: Total bound potential $\widetilde{E}$ for a particle in $\widetilde{y}$, in the binding site located in $\widetilde{b}$. The moving upper fibre lowers the exit barrier of the head in the direction of movement.

spring, the more $\widetilde{E}$ is shifted in the direction of movement and the higher the probability of detachment. In the following work, we can omit the presence of the resting length $\widetilde{l}_0$,

[1] This expression makes the assumption that $\widetilde{\sigma} > \widetilde{y}$, namely that the head is trailing the bond anchor along an axis pointed in the direction of movement.

by performing a variable change $\widetilde{s} = \widetilde{\sigma} - \widetilde{l_0}$, giving

$$\widetilde{E}(\widetilde{s}, \widetilde{y}, \widetilde{b}) = \frac{1}{2}\widetilde{K}\left(\widetilde{s} - \widetilde{y}\right)^2 + \frac{1}{2}\widetilde{\kappa}\left(\widetilde{y} - \widetilde{b}\right)^2 + \widetilde{V}_0\,, \tag{3.4}$$

which is tantamount to having the corrected anchor point $\widetilde{s}$ over the same position as the head when the spring is unstretched. Furthermore, the origin point of the position axis can be set at the binding site such that $\widetilde{b} = 0$, leading to

$$\widetilde{E}(\widetilde{s}, \widetilde{y}) = \frac{1}{2}\widetilde{K}\left(\widetilde{s} - \widetilde{y}\right)^2 + \frac{1}{2}\widetilde{\kappa}\widetilde{y}^2 + \widetilde{V}_0\,. \tag{3.5}$$

In order to determine the rate of detachment $\widetilde{k}^-\left(\widetilde{s}\right)$, we first express the energy barrier $\Delta\widetilde{E}$ to overcome for detachment:

$$\Delta\widetilde{E_\pm}\left(\widetilde{s}, \widetilde{y}\right) = E\left(\widetilde{s}, \widetilde{y} = \pm\frac{\widetilde{\delta},}{2}\right) - E(\widetilde{s}, \widetilde{y} = \widetilde{y}_{min})\,, \tag{3.6}$$

where $\widetilde{y}_{min}$ is the bond head position at the energy minimum. Both a backward and forward barrier $\Delta\widetilde{E}_-$ and $\Delta\widetilde{E}_+$ are potential escape routes for the head, with asymmetrical heights due to movement direction, as shown on figure 3.4. The minimum position $\widetilde{y}_{min}$ can be determined from the relation

$$\left.\frac{\partial\widetilde{E}}{\partial\widetilde{y}}\right|_{\widetilde{y}=\widetilde{y}_{min}}\left(\widetilde{s}\right) = 0 \quad \Rightarrow \quad \widetilde{y}_{min}\left(\widetilde{s}\right) = \frac{\widetilde{K}\widetilde{s}}{\widetilde{K} + \widetilde{\kappa}}\,. \tag{3.7}$$

Note in equation 3.7 that $\lim_{\widetilde{\kappa}\to\infty}\widetilde{y}_{min} = 0$: when the binding site potential is very stiff, the energy minimum goes to $\widetilde{b} = 0$. That is to say, the stiffer $\widetilde{V}_{bind}$ is, the more the head will be localised at the site position $\widetilde{b}$.

Let $\widetilde{U}_0 = \frac{\widetilde{\kappa}\widetilde{\delta}^2}{8}$ be the maximum height of $\widetilde{V}_{bind}$. Equation (3.6) then becomes[2]:

$$\begin{aligned}\Delta\widetilde{E}_{\pm}(\widetilde{s}) &= \frac{1}{2}\left(\widetilde{K}\left(\widetilde{s}\mp\frac{\widetilde{\delta}}{2}\right)^2+\widetilde{\kappa}\left(\pm\frac{\widetilde{\delta}}{2}\right)^2-\widetilde{K}\left(\widetilde{s}-\widetilde{y}_{min}\right)^2-\widetilde{\kappa}\widetilde{y}_{min}^2\right)\\ &= \widetilde{U}_0+\frac{1}{2}\left(\frac{\widetilde{K}\widetilde{\delta}^2}{4}\mp\widetilde{K}\widetilde{\delta}\widetilde{s}+\frac{\widetilde{K}^2\widetilde{s}^2}{\widetilde{K}+\widetilde{\kappa}}\right)\\ &= \widetilde{U}_0+\frac{\widetilde{K}\widetilde{\delta}^2}{2}\left(\frac{1}{4}\mp\frac{\widetilde{s}}{\widetilde{\delta}}+\frac{\widetilde{s}^2}{\widetilde{\delta}^2}\left(\frac{1}{1+\frac{\widetilde{\kappa}}{\widetilde{K}}}\right)\right).\end{aligned} \tag{3.9}$$

Using reaction rate theory [72, 73] (also called Kramers rate theory) for the escape of a particle from a potential well under the effect of thermal fluctuations, we can give the detachment rates $\widetilde{k}_{\pm}^{-}$ as

$$\widetilde{k}_{\pm}^{-}(\widetilde{s}) = \widetilde{k}_{off}e^{-\widetilde{\beta}\Delta\widetilde{E}_{\pm}(\widetilde{s})}, \tag{3.10}$$

where $\frac{1}{\widetilde{\beta}} = k_B\widetilde{T}$ is the energy scale of thermal fluctuations and $\widetilde{k}_{off}$ can be understood as the intrinsic detachment rate or the detachment rate for a zero-energy barrier. k_{-}^{-} is the backward rate of detachment and k_{+}^{-} is the forward rate of detachment.

The final detachment rate, plotted on figure 3.5, is counted as the sum of forward and backward detachment rates:

$$\widetilde{k}^{-}(\widetilde{s}) = \widetilde{k}_{+}^{-}(\widetilde{s})+\widetilde{k}_{-}^{-}(\widetilde{s}) = \begin{cases}2\widetilde{k}_{off}e^{-\widetilde{\beta}\left(\widetilde{U}_0+\frac{\widetilde{K}\widetilde{\delta}^2}{8}\right)}e^{-\frac{\widetilde{\beta}}{2}\frac{\widetilde{K}^2}{\widetilde{K}+\widetilde{\kappa}}\widetilde{s}^2}\cosh\left(\frac{\widetilde{\beta}}{2}\widetilde{K}\widetilde{\delta}\widetilde{s}\right) & \text{if } |\widetilde{s}| < \frac{\widetilde{\delta}(\widetilde{K}+\widetilde{\kappa})}{2\widetilde{K}},\\ +\infty & \text{otherwise}.\end{cases} \tag{3.11}$$

This rate obtained from reaction rate theory is valid as long as the time for the head inside the potential well to reach equilibrium is fast compared to the escape time from the barrier, i.e. the binding site represents a well-defined local minimum of the energy of

[2]The energy barrier for an arbitrary binding site position $\widetilde{b}$ is

$$\Delta\widetilde{E}_{\pm}\left(\widetilde{s},\widetilde{b}\right) = \widetilde{U}_0+\frac{1}{2}\left(\frac{\widetilde{K}\widetilde{\delta}^2}{4}+\widetilde{b}^2\frac{\widetilde{\kappa}^2}{\widetilde{K}+\widetilde{\kappa}}\mp\widetilde{\kappa}\widetilde{b}\widetilde{\delta}\right)+\frac{\widetilde{s}}{2}\left(2\widetilde{b}\frac{\widetilde{K}\widetilde{\kappa}}{\widetilde{K}+\widetilde{\kappa}}\mp\widetilde{K}\widetilde{\delta}\right)+\frac{\widetilde{s}^2}{2}\left(\frac{\widetilde{K}}{\widetilde{K}+\widetilde{\kappa}}\right). \tag{3.8}$$

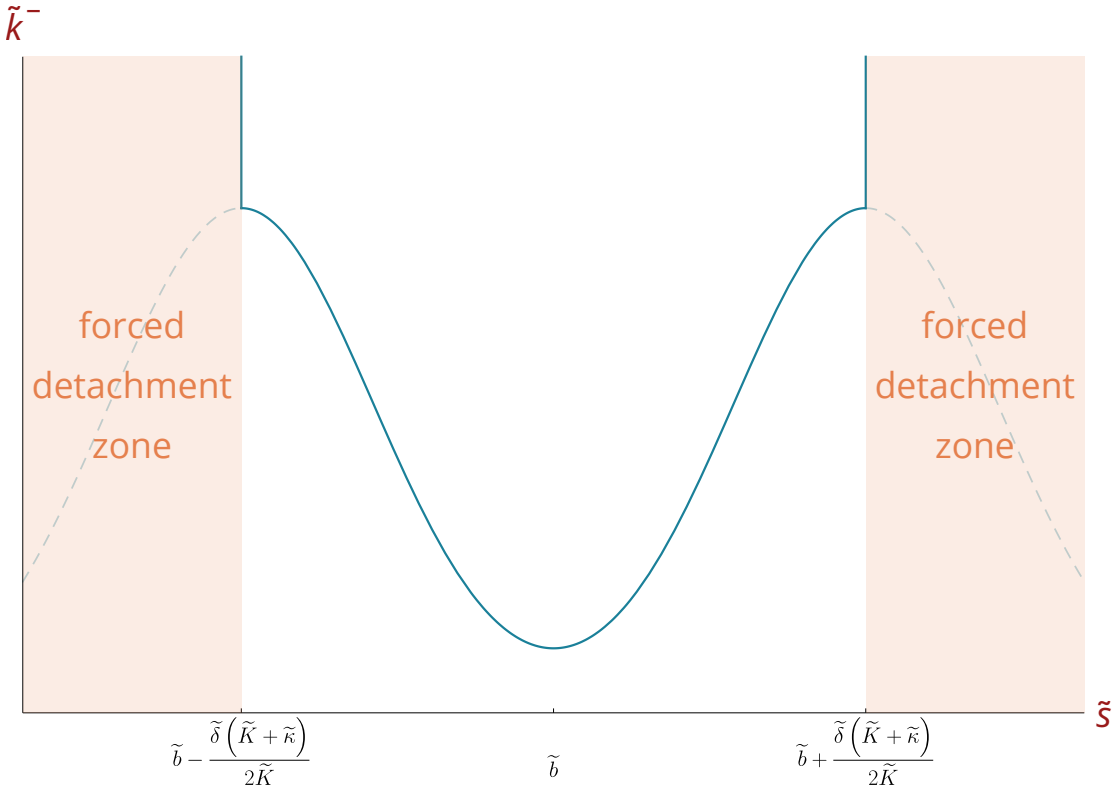

Figure 3.5: $\widetilde{k}^-$ plotted against $\widetilde{s}$. The behaviour of the function given in equation 3.11 outside of the validity of reaction rate theory is outlined with a dashed line. Plotting parameters: $\widetilde{k}_{off} = 1\,, \quad \widetilde{\beta} = 1\,, \quad \widetilde{U}_0 = 1\,, \quad \widetilde{K} = 1\,, \quad \widetilde{\kappa} = 10\,, \quad \widetilde{\delta} = 1\,.$

the bond. This translates to the following criterion:

$$|\widetilde{y}_{min}| < \frac{\widetilde{\delta}}{2} \quad \Leftrightarrow \quad |\widetilde{s}| < \frac{\widetilde{\delta}\left(\widetilde{K}+\widetilde{\kappa}\right)}{2\widetilde{K}}\,. \tag{3.12}$$

Beyond this validity limit there exists no local minimum of the bond energy within the binding site anymore, so $\widetilde{s} = \pm\frac{\widetilde{\delta}\left(\widetilde{K}+\widetilde{\kappa}\right)}{2\widetilde{K}}$ is used as a cutoff beyond which a detachment probability of 100% is enforced. This fact is also reflected in the shape of the function describing $\widetilde{k}^{-}\left(\widetilde{s}\right)$ in equation 3.11, where the detachment rate increases with $\widetilde{s}$ while $|\widetilde{s}| < \frac{\widetilde{\delta}\left(\widetilde{K}+\widetilde{\kappa}\right)}{2\widetilde{K}}$ and starts decreasing with $\widetilde{s}$ afterwards. This behaviour would be contrary to our expectation that loading, and therefore detachment rate, increases monotonously as $\widetilde{s}$ increases for a bound cross-bridge.

The Kramers rate theory is valid in the limit where the barrier to escape the binding site is large with respect to the thermal energy. Thus, it imposes that $r_{en} = \widetilde{\beta}/8\left(\widetilde{K}+\widetilde{\kappa}\right)\widetilde{\delta}^2 \gg 1$. In our initial simulations, we took a value of r_{en} around 3. Although this is sufficient to capture the qualitative features of our system, we have increased $\widetilde{\kappa}$ when we simulated the corrected model so that we had a r_{en} larger than 10. Equation 3.11 also provides length scales applicable to the system in question. One length scale is found in the factor $e^{-\frac{\widetilde{\beta}\widetilde{K}^2}{\widetilde{K}+\widetilde{\kappa}}\widetilde{s}^2}$ of equation 3.11. The length is

$$\widetilde{l}_{well} = \sqrt{\frac{k_B\widetilde{T}\left(\widetilde{K}+\widetilde{\kappa}\right)}{\widetilde{K}^2}}\,. \tag{3.13}$$

Another length found in the factor $\cosh\left(\widetilde{\beta}\widetilde{K}\widetilde{\delta}\widetilde{s}\right)$ of equation 3.11 is

$$\widetilde{l}_{Bell} = \frac{k_B\widetilde{T}}{\widetilde{K}\widetilde{\delta}}\,. \tag{3.14}$$

A third length scale is the detachment length

$$\widetilde{l}_{detach} = \frac{\widetilde{\delta}\left(\widetilde{K}+\widetilde{\kappa}\right)}{2\widetilde{K}}\,. \tag{3.15}$$

$\widetilde{l}_{detach}$ gives the length beyond which forced detachment from the binding site occurs and is therefore a measure of the size of a binding site.

3.3 Detached Bond - Initial Model

We assume that a given affinity exists between detached heads and binding sites, such that free heads attach themselves to a binding site with a constant rate $\widetilde{k}_{on}$ while they are within range of a binding site. However, since heads are thermally activated, they themselves visit a range of position in the neighbourhood of the corrected anchor point position $\widetilde{s}$. The elongation $\widetilde{x}$ of a detached bond therefore has a certain equilibrium distribution, which grows wider as temperature increases. The assumption that detached

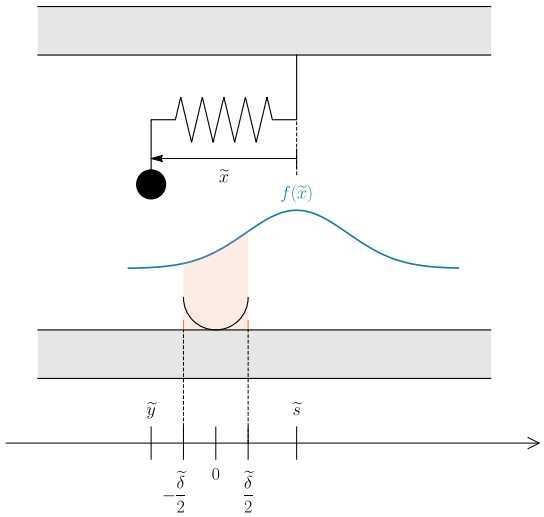

Figure 3.6: The probability of bonding to a single site can be determined by evaluating the probability of a head to be within range of the binding site of size $\widetilde{\delta}$. $f(\widetilde{x})$ represents the probability density of the head to have an elongation $\widetilde{x}$.

heads attach at a constant rate within the entire binding site thus reflects the fact that the time taken to thermally reach the equilibrium distribution of $\widetilde{x}$ is much faster than the typical time to bind to a site. This is also in keeping with the assumption made previously in reaction rate theory, that for attached heads, the escape time from the binding potential is much slower than the thermal equilibrium time within the potential well. However, an asymmetry in the model can be detected here: the attachment can

occurs everywhere in the site, while the detachment occurs only in $\pm\widetilde{\delta}/2$. This asymmetry is the cause of the breaking of the detailed balance in this initial model. A more detailed discussion on our choice to correct our model is done in the next section 3.4.

The attachment rate $\widetilde{k}_+$ to a binding site at position $\widetilde{b} = 0$ is then the intrinsic rate $\widetilde{k}_{on}$ weighted by the probability that the elongation distribution of the head overlaps with the binding site, as illustrated on figure 3.6. This translates to

$$\widetilde{k}^+(\widetilde{s}) = \widetilde{k}_{on} \int_{-\frac{\widetilde{\delta}}{2}}^{+\frac{\widetilde{\delta}}{2}} f(\widetilde{x} - \widetilde{s}) d\widetilde{x} = \widetilde{k}_{on} \int_{\widetilde{s}-\frac{\widetilde{\delta}}{2}}^{\widetilde{s}+\frac{\widetilde{\delta}}{2}} f(\widetilde{x}) d\widetilde{x}\,, \tag{3.16}$$

where f is the probability density for a head to be at a distance $\widetilde{x}$ of the resting-length-corrected anchor point, as shown on figure 3.6. We posit an expression of f, with the assumption that unbound heads reach their equilibrium position quickly relative to the fibre movement speed. This leads to a Boltzmann distribution:

$$f(\widetilde{x}) = \frac{e^{-\widetilde{\beta}\widetilde{K}\widetilde{x}^2}}{\int_{-\infty}^{+\infty} e^{-\widetilde{\beta}\widetilde{K}\widetilde{x}^2} dx} = \sqrt{\frac{\widetilde{\beta}\widetilde{K}}{\pi}} e^{-\widetilde{\beta}\widetilde{K}\widetilde{x}^2}\,. \tag{3.17}$$

A length scale associated to the detached system is therefore

$$\widetilde{\lambda} = \sqrt{\frac{k_B \widetilde{T}}{\widetilde{K}}}\,. \tag{3.18}$$

$\widetilde{\lambda}$ is the length associated with the width of the binding rate around the individual binding sites. The binding rate $\widetilde{k}^+$ can therefore be expressed as

$$\widetilde{k}^+(\widetilde{s}) = \widetilde{k}_{on} \frac{1}{\sqrt{\widetilde{\lambda}^2 \pi}} \int_{\widetilde{s}-\frac{\widetilde{\delta}}{2}}^{\widetilde{s}+\frac{\widetilde{\delta}}{2}} e^{-\left(\frac{\widetilde{x}}{\widetilde{\lambda}}\right)^2} d\widetilde{x} = \frac{\widetilde{k}_{on}}{\sqrt{\pi}} \int_{\left(\widetilde{s}-\frac{\widetilde{\delta}}{2}\right)/\widetilde{\lambda}}^{\left(\widetilde{s}+\frac{\widetilde{\delta}}{2}\right)/\widetilde{\lambda}} e^{-\widetilde{x}^2} d\widetilde{x}\,, \tag{3.19}$$

as shown on figure 3.7.

Equation 3.19 can also be expressed in terms of the error function $\mathrm{erf}\,(x) = \frac{1}{\sqrt{\pi}} \int_{-x}^{x} e^{-t^2} dt$, which is convenient when a numerical evaluation of $\widetilde{k}^+$ is needed:

$$\widetilde{k}^+\,(\widetilde{s}) = \frac{\widetilde{k}_{on}}{2} \left(\mathrm{erf}\left(\frac{\widetilde{s} + \frac{\widetilde{\delta}}{2}}{\widetilde{\lambda}} \right) - \mathrm{erf}\left(\frac{\widetilde{s} - \frac{\widetilde{\delta}}{2}}{\widetilde{\lambda}} \right) \right)\,. \tag{3.20}$$

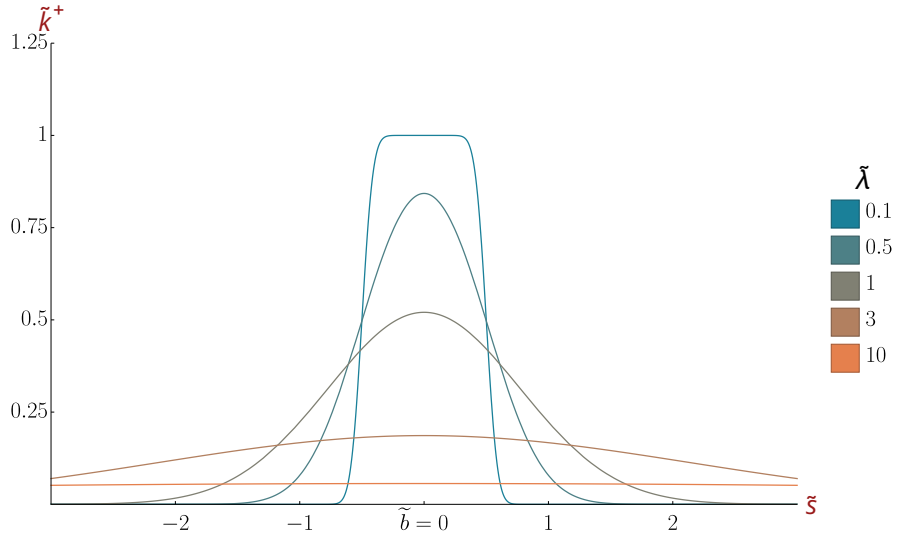

Figure 3.7: $\widetilde{k}^+$ plotted against $\widetilde{s}$ for different values of $\widetilde{\lambda}$.

Plotting parameters: $\widetilde{k}_{on} = 1\,, \quad \widetilde{\delta} = 1\,.$

Additionally, equation 3.20 gives an intuitive interpretation of the effect of the parameter $\widetilde{\delta}$, the spatial site extension. As shown on figure 3.8, $\widetilde{k}^+$ can be seen as the difference between two sigmoid-like error functions, horizontally shifted by an amount $\widetilde{\delta}$. Since $\widetilde{\delta}$ is the distance separating two shifted error functions, it can be seen as a measure of the "flatness" of the attachment rate peak. The bigger the value, the larger the maximum zone of the binding site attachment rate, which is consistent with the fact that the spatial extension of the binding site is increasing. Additionally, $\widetilde{\lambda}$ can be seen as the variation length of the error function.

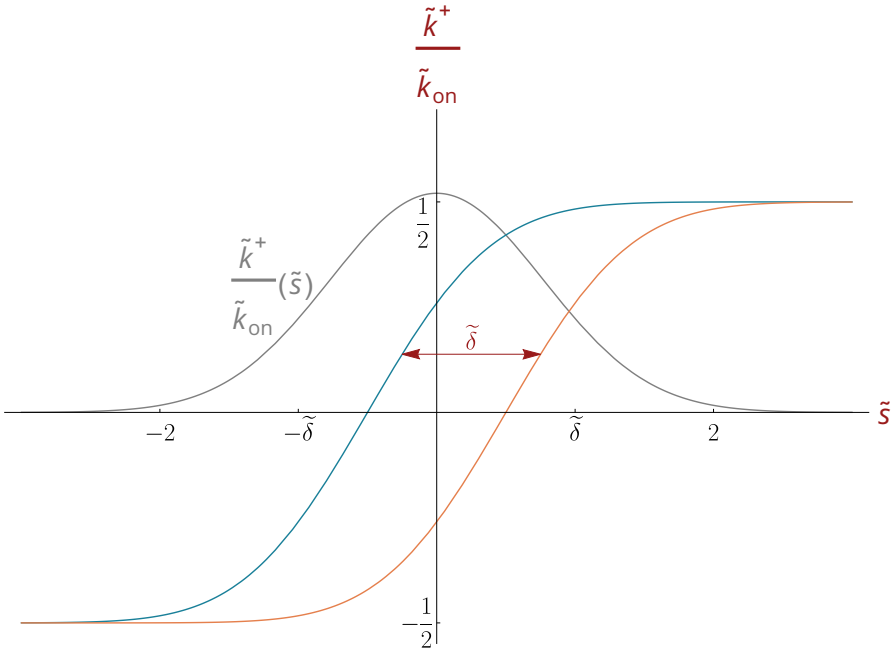

(a) $\widetilde{\delta} = 1$.

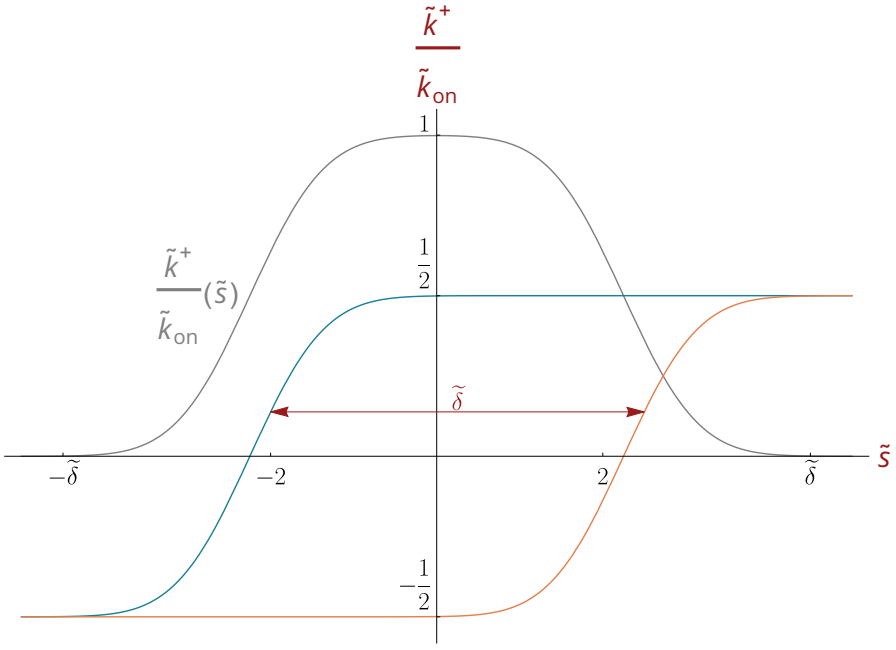

(b) $\widetilde{\delta} = 4.5$.

Figure 3.8: $\frac{\widetilde{k}^+}{\widetilde{k}_{on}}$ (plotted in grey), is the difference between two erf functions (plotted in blue and orange) each shifted by an amount $\frac{\widetilde{\delta}}{2}$ from the origin. Plots are drawn for (a) $\widetilde{\delta}$=1, (b) $\widetilde{\delta} = 4.5$. Other parameters are $\widetilde{k}_{on} = 1$, $\widetilde{\beta} = 1$, $\widetilde{K} = 1$.

3.4 Detached Bond - Corrected to Respect the Detailed Balance

3.4.1 Detailed Balance for our Initial Model

If we now assemble all the elements of the model, we have a model for the detachment rate, and a model for the attachment rate. As pointed out in the presentation of the detached bond modelling (section 3.3), the two descriptions are asymmetric microscopically. Indeed, for the detachment, one doesn't really distinguish the different localizations $\widetilde{y}$ of the head, assuming that they detach only at the border of the well. For the attachment, we explicitly track the position of the head over the binding site, so that we define a binding rate at each location of the head. Without further refinement of the model, this assumes that the reverse process of the attachment for the position y is negligible with respect to the detachment except at the positions $\pm\widetilde{\delta}/2$.

To test the detailed balance, it is easier to consider a two-state picture, without writing the detailed balanced at each y (which may also be done). We thus have 2 states: a detached and an attached one. The detached state has a mean energy of 0, which is the energy at the mean position of the spring alone (see eq. 3.2). The attached state has a mean energy of

$$\widetilde{E}_{bind} = \widetilde{E}(\widetilde{s}, \widetilde{y}_{min}) = \frac{1}{2}\frac{\widetilde{\kappa}\widetilde{K}}{\widetilde{\kappa}+\widetilde{K}}\widetilde{s}^2 + \widetilde{V}_0, \tag{3.21}$$

using the expression of 3.4 of the bound potential at its minimum 3.7. Thus the detailed balance should impose that

$$\frac{\widetilde{k}^-}{\widetilde{k}^+} \propto \exp\left(\widetilde{\beta}(\widetilde{E}_{bind})\right) \propto \exp\left(\frac{\widetilde{\beta}}{2}\frac{\widetilde{\kappa}\widetilde{K}}{\widetilde{\kappa}+\widetilde{K}}\widetilde{s}^2\right). \tag{3.22}$$

In contrast to this, our ratio of attachment / detachment rates leads to

$$\frac{\widetilde{k}^-}{\widetilde{k}^+} = \frac{2\widetilde{k}_{off}e^{-\widetilde{\beta}\left(\widetilde{U}_0+\frac{\widetilde{K}\widetilde{\delta}^2}{8}\right)}e^{-\frac{\widetilde{\beta}}{2}\frac{\widetilde{K}^2}{\widetilde{K}+\widetilde{\kappa}}\widetilde{s}^2}\cosh\left(\frac{\widetilde{\beta}}{2}\widetilde{K}\widetilde{\delta}\widetilde{s}\right)}{\frac{\widetilde{k}_{on}}{2}\left(\mathrm{erf}\left(\frac{\widetilde{s}+\frac{\widetilde{\delta}}{2}}{\sqrt{2}\widetilde{\lambda}}\right)-\mathrm{erf}\left(\frac{\widetilde{s}-\frac{\widetilde{\delta}}{2}}{\sqrt{2}\widetilde{\lambda}}\right)\right)}. \tag{3.23}$$

while the head is attached ($|\widetilde{s}| < \frac{\widetilde{\delta}(\widetilde{K}+\widetilde{\kappa})}{2\widetilde{K}}$). Obviously, these two expression of the ratio of the attachment / detachment rates are different. This means that our model does not satisfy the detailed balance. Thus, any state close to the equilibrium should be taken carefully. In the dynamical considerations that we investigated in this thesis, this is likely to have a limited impact on our results as the heads are dragged away from the binding site. Thus, for most of the heads, the detachment occurs in a different region than the attachment and an error on the attachment rate will thus have a limited impact. Typically, the heads attach on a size $\widetilde{\lambda}$. Their typical detachment rate will be in this region around k_{off}. So, the drag will dominate the detachment in the region near the binding site if $\widetilde{v} \gg \widetilde{\lambda}\widetilde{k}_{off}$. Most of the simulations done with the initial model satisfy this condition (which translate into $v > 0.7$ using the nondimensionalisation of the next section 3.5. Still, a corrected, thermodynamically exact model is also presented here.

3.4.2 Corrected Detachment Rate

To restore the detailed balance, we propose to replace the attachment rate $\widetilde{k}^{+}(\widetilde{s})$ by an expression satisfying the detailed balance. This choice leads to the fact that the detachment rate is local, while our initial attachment rate was chosen as an integral expression. Thus, modifying the detachment rate would have ask us to construct a local model, feasible and maybe more relevant in our modeling frame but outside the scope of this PhD work.

Therefore, we start from the detachment rate (Eq. 3.11 - for $\widetilde{s}$ enabling a detachment rate)

$$\widetilde{k}^{-}(\widetilde{s}) = 2\widetilde{k}_{off} e^{-\widetilde{\beta}\left(\widetilde{U}_0 + \frac{\widetilde{K}\widetilde{\delta}^2}{8}\right)} e^{-\frac{\widetilde{\beta}}{2}\frac{\widetilde{K}^2}{\widetilde{K}+\widetilde{\kappa}}\widetilde{s}^2} \cosh\left(\frac{\widetilde{\beta}}{2}\widetilde{K}\widetilde{\delta}\widetilde{s}\right) \quad \text{if } |\widetilde{s}| < \frac{\widetilde{\delta}\left(\widetilde{K}+\widetilde{\kappa}\right)}{2\widetilde{K}}.$$

We combine this expression with the detailed balance (Eq. 3.22):

$$\frac{\widetilde{k}^-}{\widetilde{k}^+} \propto \exp\left(\widetilde{\beta}(\widetilde{E}_{bind})\right) \propto \exp\left(\frac{\widetilde{\beta}}{2}\frac{\widetilde{\kappa}\widetilde{K}}{\widetilde{\kappa}+\widetilde{K}}\widetilde{s}^2)\right). \tag{3.24}$$

This imposes the expression of k^+:

$$\begin{aligned}
\widetilde{k}^+(\widetilde{s}) &\propto \widetilde{k}^-(\widetilde{s})\exp\left(-\frac{\widetilde{\beta}}{2}\frac{\widetilde{\kappa}\widetilde{K}}{\widetilde{\kappa}+\widetilde{K}}\widetilde{s}^2)\right) \\
&\propto 2\,\widetilde{k}_{off}\exp\left(-\widetilde{\beta}\widetilde{V}_0-\frac{\widetilde{\beta}}{8}\widetilde{K}\widetilde{\delta}^2\right)\cosh\left(\frac{\widetilde{\beta}}{2}\widetilde{K}\widetilde{s}\widetilde{\delta}\right)\exp\left(-\frac{\widetilde{\beta}}{2}\left(\frac{\widetilde{K}^2}{\widetilde{K}+\widetilde{\kappa}}+\frac{\widetilde{\kappa}\widetilde{K}}{\widetilde{K}+\widetilde{\kappa}}\right)\widetilde{s}^2\right) \\
&\propto 2\,\widetilde{k}_{off}\exp\left(-\widetilde{\beta}\widetilde{V}_0-\frac{\widetilde{\beta}}{8}\widetilde{K}\widetilde{\delta}^2\right)\cosh\left(\frac{\widetilde{\beta}}{2}\widetilde{K}\widetilde{s}\widetilde{\delta}\right)\exp\left(-\frac{\widetilde{\beta}}{2}\widetilde{K}\widetilde{s}^2\right)\,.
\end{aligned} \tag{3.25}$$

So, an expression of $k^+(s)$ which satisfies the detailled balance is:

$$\widetilde{k}^+(\widetilde{s}) = \widetilde{k}_{on}\cosh\left(\frac{\widetilde{\beta}}{2}\widetilde{K}\widetilde{s}\widetilde{\delta}\right)\exp\left(-\frac{\widetilde{\beta}}{2}\widetilde{K}\widetilde{s}^2\right)\,. \tag{3.26}$$

This expression of $\widetilde{k}^-$ reflects the fact that the particle starts in average from 0 and has to reach the points $\pm\widetilde{\delta}/2$ to bind to the site, climbing the spring potential.

3.5 Nondimensionalisation

We rewrite all dimensioned quantities $\widetilde{q}$ denoted with a tilde into non-dimensioned quantities q denoted without a tilde, by dividing dimensioned quantities by a reference quantity. When choosing a reference quantity for normalisation, one rationale can be the existence of a natural scaling parameter, such as a natural length scale. Another rationale is to use quantities which fade in relevancy when looking at larger scale dynamics, most often due to coarse-graining in the model response. The justification for this is simply to keep the most relevant quantities at the forefront of visible equations. The final reasoning we highlight for choosing a reference normalisation value is one of formal simplicity. Sometimes a choice of non-dimensionalisation produces simpler equations in an aesthetic sense. The latter two rationales are the ones used in this work to produce the following

non-dimensionalisation of quantities. In our case, since the fibre network is described in a generic fashion and includes no explicit empirical tie to a specific biological system, no natural length scales appear at this stage. Possible length scales in our system is listed below:

$$\widetilde{\delta}\,, \quad \widetilde{l}_{well} = \sqrt{\frac{k_B\widetilde{T}\left(\widetilde{K}+\widetilde{\kappa}\right)}{\widetilde{K}^2}}\,, \quad \widetilde{l}_{Bell} = \frac{k_B\widetilde{T}}{\widetilde{K}\widetilde{\delta}}\,, \quad \widetilde{l}_{detach} = \frac{\widetilde{\delta}\left(\widetilde{K}+\widetilde{\kappa}\right)}{2\widetilde{K}} \text{ and } \quad \widetilde{\lambda} = \sqrt{\frac{k_B\widetilde{T}}{\widetilde{K}}}\,. \tag{3.27}$$

The reference length chosen is $\widetilde{\delta}$ the binding site spatial extension. This is done with the expectation that $\widetilde{\delta}$, being likely the smallest length quantity next to $\widetilde{y}$, will play a relatively lesser role in the whole system dynamics. Lengths are therefore rewritten as

$$s = \frac{\widetilde{s}}{\widetilde{\delta}}\,. \tag{3.28}$$

Next, the stiffness is normalised by $\widetilde{K}$ the bond spring stiffness constant. This choice is made due to the prevalence of $\widetilde{K}$ in the various expressions derived previously. Furthermore, in our assumptions, we adopt a point of view where the site stiffness $\widetilde{\kappa}$ is larger compared to the cross-bridge stiffness $\widetilde{K}$. This is consistent with the view that the binding site is localised in space. These reasons make $\widetilde{K}$ a good candidate for the reference stiffness. Stiffnesses are therefore rewritten as

$$\kappa = \frac{\widetilde{\kappa}}{\widetilde{K}}\,. \tag{3.29}$$

Finally, the time normalisation can be chosen from either $\widetilde{k}_{on}$, $\widetilde{k}_{off}$ or a combination of both, such as $\widetilde{k}_{on} + \widetilde{k}_{off}$. Since no natural choice emerges, we choose a normalisation which leads to the simplest expression possible, in this case based on $\widetilde{k}_{off}$. Binding rates are therefore rewritten as

$$k_{on} = \frac{\widetilde{k}_{on}}{\widetilde{k}_{off}}\,. \tag{3.30}$$

Following the non-dimensionalisation choices made for length and stiffness, the following

dimensionless energy constant β can be defined for convenience:

$$\beta = \widetilde{\beta}\widetilde{K}\widetilde{\delta}^2 \,. \tag{3.31}$$

This procedure gives, at $b = 0$, a dimensionless detachment energy barrier

$$\Delta E_{\pm}(s) = \frac{\Delta \widetilde{E}_{\pm}}{\widetilde{K}\widetilde{\delta}^2} = U_0 + \frac{1}{2}\left(\frac{1}{4} \mp s + \frac{s^2}{1+\kappa}\right), \tag{3.32}$$

a dimensionless detachment rate

$$k^-(s) = \frac{\widetilde{k}^-}{\widetilde{k}_{off}} = \begin{cases} 2e^{-\beta\left(U_0+\frac{1}{8}\right)} e^{\frac{\beta}{1+\kappa}s^2} \cosh(\beta s) & \text{if } |s| < \frac{1+\kappa}{2}\,, \\ +\infty & \text{otherwise}\,, \end{cases} \tag{3.33}$$

and a dimensionless attachment rate

$$\begin{aligned} k^+(s) &= \frac{\widetilde{k}^+}{\widetilde{k}_{off}} \\ &= \frac{k_{on}}{\sqrt{\pi}} \int_{\sqrt{\beta}\left(s-\frac{1}{2}\right)}^{\sqrt{\beta}\left(s+\frac{1}{2}\right)} e^{-x^2} dx \\ &= \frac{k_{on}}{2}\left(\operatorname{erf}\left(\sqrt{\beta}\left(s+\frac{1}{2}\right)\right) - \operatorname{erf}\left(\sqrt{\beta}\left(s-\frac{1}{2}\right)\right)\right). \end{aligned} \tag{3.34}$$

Or for the corrected k^+ which respects the detailed balance:

$$k^+(s) = k_{on} \cosh\left(\frac{\beta}{2}s\right) \exp\left(-\frac{\beta}{2}s^2\right) \tag{3.35}$$

3.6 Multiple Bonds with Periodic Binding Sites

In the previous sections we described the system as it applies to fibres with a single cross-bridge and a single binding site. We now extend this description to fibres presenting multiple cross-bridges N facing infinitely periodic binding sites with inter-site distance d (following our non-dimensionalisation convention, $d = \frac{\widetilde{d}}{\widetilde{\delta}}$) as illustrated on figure 3.9. One of the most important feature of the periodic system is the change of reference used to describe positions. All positions are now taken relative to the closest binding site instead

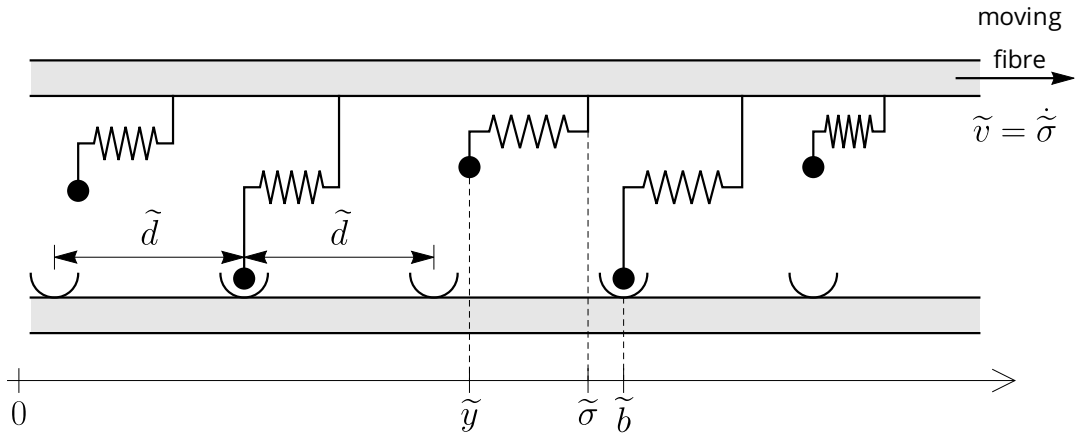

Figure 3.9: Interacting fibre system exhibiting periodic binding sites with periodicity $\widetilde{d}$.

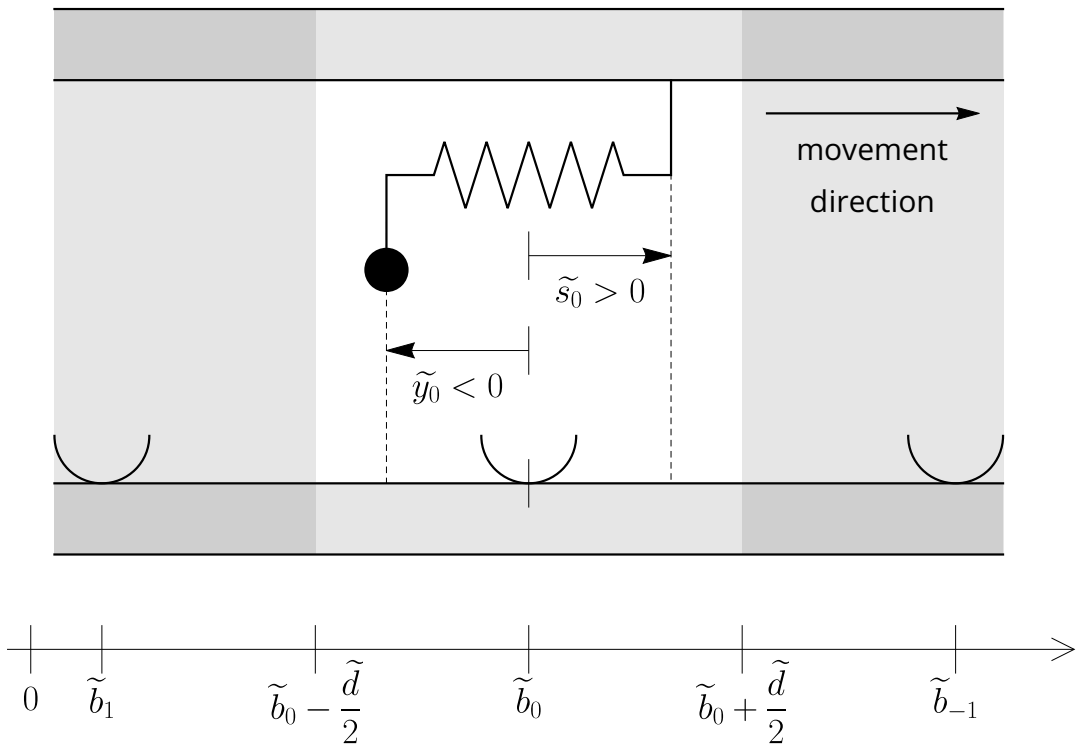

Figure 3.10: A system with periodic binding sites. Positions y_0 and s_0 are taken relative to the closest binding site $\widetilde{b}_0$.

of relative to a common origin point. We use the subscript 0 to denote positions taken relative to the closest binding site. This gives rise to the relative head position y_0, the relative unshifted anchor position σ_0 and the relative shifted anchor position $s_0 = \sigma_0 - l_0$. As shown on figure 3.10, we adopt a sign convention whereby positions located before the binding site with respect to the movement direction are taken negative, and positions located after the site with respect to movement direction are taken positive.

These conventions are used in order to reduce the description of N bonds interacting with infinitely periodic binding sites to N bonds interacting with a single binding site over a single period d. Furthermore, the use of the closest binding site as origin of position allows for the use of all previously derived expressions for attachment and detachment rates of a single bond without loss of generality, by substituting the positions b, s and y with the corresponding $b_0 = 0$, s_0 and y_0. The dynamics of the system will thus be computed, with some exceptions discussed below, for a system of N independent cross-bridges interacting with a fibre of length d possessing a single binding site and exhibiting periodic boundary conditions.

3.7 Attached Bond, Periodic Binding Sites

On a periodic system, each attached bond follows the behaviour described in section 3.2 with a detachment rate

$$k^{-}(s_0) = \begin{cases} 2e^{-\beta\left(U_0+\frac{1}{8}\right)} e^{\frac{\beta}{1+\kappa}s_0^2} \cosh(\beta s_0) & \text{if } |s_0| < \frac{1+\kappa}{2}, \\ +\infty & \text{otherwise}. \end{cases} \tag{3.36}$$

Attached bonds are considered similarly to section 3.2 with a forced detachment that is enforced once $|s_0| \geq \frac{1+\kappa}{2}$. This means that attached cross-bridges do not follow periodic boundary conditions. Indeed, if periodic boundary conditions were enforced, in the case that the distance to the periodic boundary $\frac{d}{2}$ is smaller than the distance of forced

detachment $\frac{1+\kappa}{2}$, the detachment rate would start to erroneously decrease for $\frac{d}{2} \leq |s_0| \leq \frac{1+\kappa}{2}$, as shown on figure 3.11. Intuitively, one knows that detachment rate can only

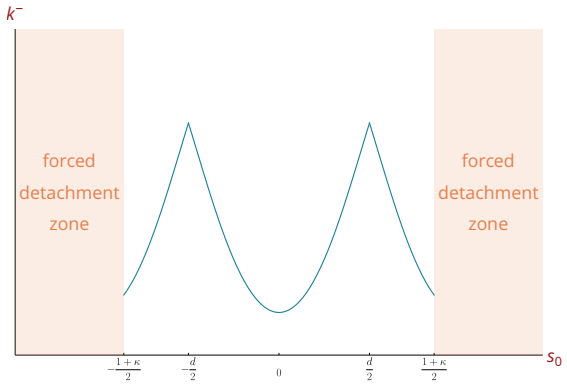

Figure 3.11: Normalised detachment rate k^- with enforced periodic boundary conditions. $k^-(s_0)$ does not grow monotonously with $|s_0|$, so this periodic boundary condition is not used in the model.
Plotting parameters: $\beta = 1\,, \quad U_0 = 1\,, \quad \kappa = 10\,.$

monotonously increase as the cross-bridge is loaded, therefore the boundary condition with forced detachment, as in figure 3.5, is used instead of the periodic one.

3.8 Detached Bond, Periodic Binding Sites

In the case of detached bonds, the previous attachment rate derived in section 3.3 is still valid when applied to a single period of the fibre, except that one must now take into account the possibility of attaching to neighbouring binding sites. Indeed, should a cross-bridge connect to a distant binding site, the starting load of the attached bond will be higher than that of a bond attached to the closest binding site due to the increased stretch of the bond spring. With regards to k^+, we add the contribution of neighbouring

sites to the expression of equation 3.34:

$$\begin{aligned} k^+(s_0) &= \frac{k_{on}}{\sqrt{\pi}} \sum_{i=-\infty}^{+\infty} k_i^+(s_0) \\ &= \frac{k_{on}}{\sqrt{\pi}} \sum_{i=-\infty}^{\infty} \int_{\sqrt{\beta}\left(s_0+id-\frac{1}{2}\right)}^{\sqrt{\beta}\left(s_0+id+\frac{1}{2}\right)} e^{-x^2} dx \\ &= \frac{k_{on}}{2} \sum_{i=-\infty}^{\infty} \left(\operatorname{erf}\left(\sqrt{\beta}\left(s_0+id+\frac{1}{2}\right)\right) - \operatorname{erf}\left(\sqrt{\beta}\left(s_0+id-\frac{1}{2}\right)\right)\right), \end{aligned} \tag{3.37}$$

where the binding sites i are numbered positively when a bound head contributes positively to the total load and negatively when a bound head contributes negatively, as illustrated on figure 3.12.

In order to perform numerical computations, we naturally want to restrict bonding to a

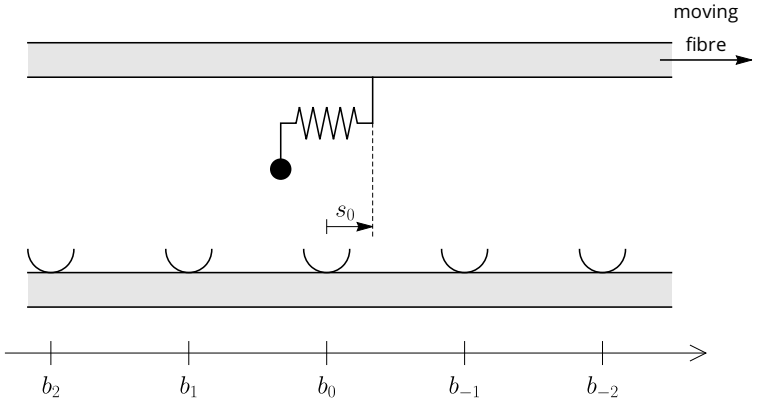

Figure 3.12: Binding sites are numbered relative to the binding site closest to the anchor point of the bond ($i = 0$) . The site number is positive opposite the direction of fibre movement and negative in this direction.

finite number $n \geq 0$ of neighbours to the closest binding site, since k^+ becomes vanishingly close to 0 for far-off binding sites. The cutoff is chosen such that the probability of attaching to a relevant neighbouring binding site, measured as a fraction of the maximum of the closest binding site, must be above a certain threshold c. Due to the symmetry of the binding rate function, for a given c, the total number of considered binding sites will

be $2n+1$, with n verifying

$$n = \min\left(i \in \mathbb{N}, \quad \frac{k^+\left(s_0 = d\left(\frac{1}{2}+i\right)\right)}{k^+\left(s_0 = 0\right)} > c\right). \tag{3.38}$$

Typically, $c = 1\%$ is chosen. The shape of k^+ and its sum components $k^+_{\pm n}$ is illustrated for different d with $c = 1\%$, inducing $n = 0, 1, 2, 3$ on figure 3.13. If $n = 0$, then only the closest site is relevant. See figure 3.14 for an illustration using $n = 0$ and $n = 1$ for $c = 10\%$. The number of relevant binding site in a simulation is therefore a function of the shape of the bonding probability function k^+ and the binding site periodicity d. Figure 3.15 illustrates this dependence on binding site periodicity for a given c.

As shown on figure 3.13, the smaller the intersite distance d, the higher the number of relevant neighbours n contributing to k^+. As d becomes small, the total attachment rate k^+ increases and becomes wider in shape, eventually becoming flat across the period window. The plot of $k^+\left(s_0\right)$ on figure 3.16 shows how this flattening occurs as the value of d decreases. Plotting the rate contributions of neighbouring binding sites, as done on figure 3.13d, clearly shows that for numerous contributing neighbours, the total rate k^+ flattens at a value equal to the sum total of the $2n+1$ maximum values of individual binding sites. This is essentially the same as prescribing a constant attachment rate k^+ and can be interpreted as the continuum limit of our discrete binding site model: when binding site spacing d goes to zero, a detached cross-bridge can attach itself everywhere and the k^+ is a flat constant. Indeed, this approach is commonly adopted in models of various adhesion problems in the literature, where detachment rate is described as load dependent but attachment rate follows a constant rate. Such examples can be found in the models of Bell [68], Odde et al. [94, 95], Schwarz et al. [74] or Sens [96].

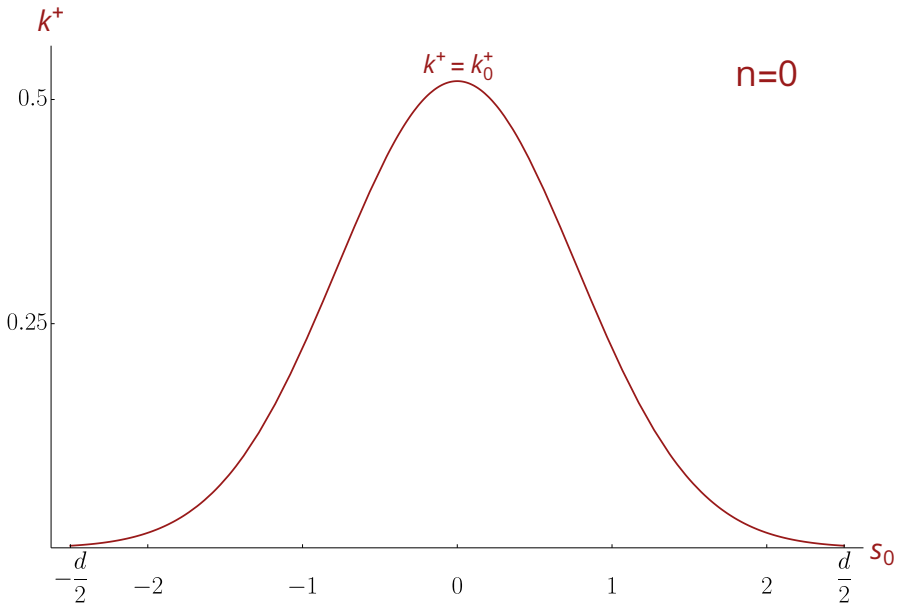

(a) Plotting parameters: $k_{on} = 1\,, \quad \beta = 1\,, \quad d = 5\,, \quad c = 1\%\,.$

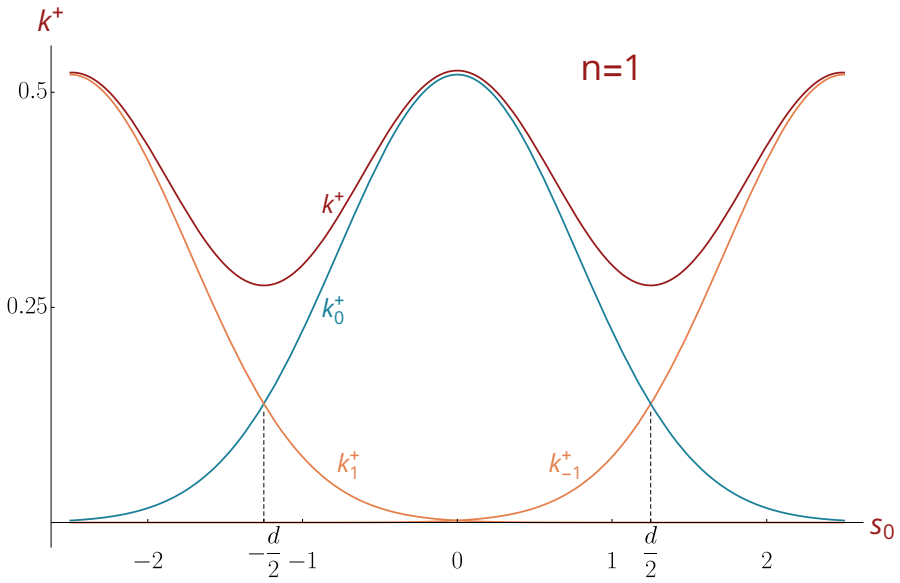

(b) Plotting parameters: $k_{on} = 1\,, \quad \beta = 1\,, \quad d = 2.5\,, \quad c = 1\%\,.$

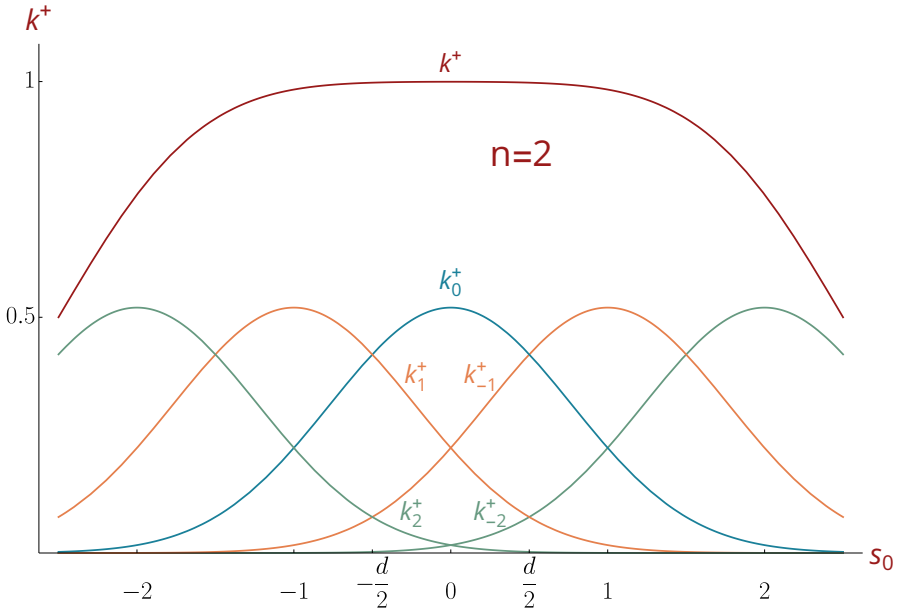

(c) Plotting parameters: $k_{on} = 1\,, \quad \beta = 1\,, \quad d = 1\,, \quad c = 1\%\,.$

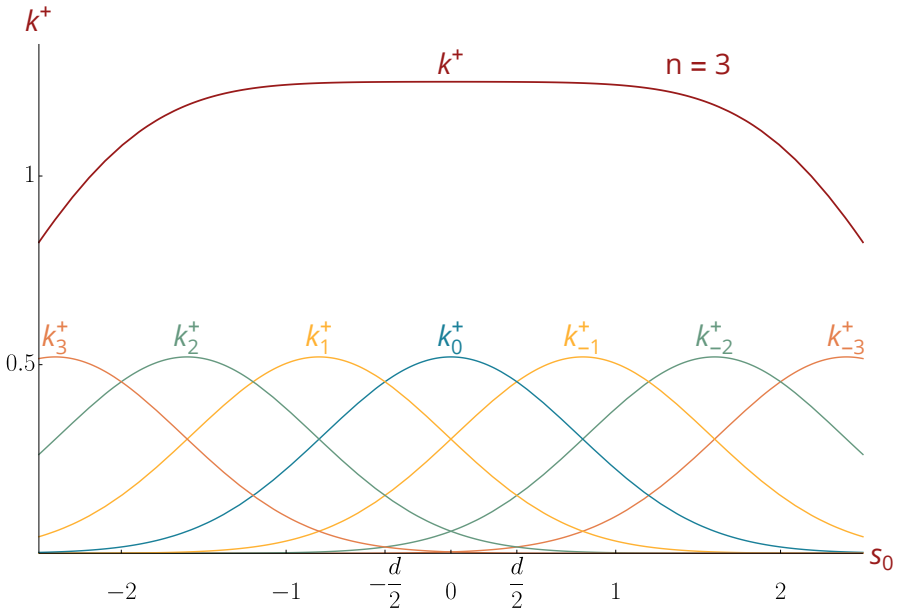

(d) Plotting parameters: $k_{on} = 1\,, \quad \beta = 1\,, \quad d = 0.8\,, \quad c = 1\%\,.$

Figure 3.13: Plot of $k^+(s_0) = \sum_{i=-n}^{n} k_i^+$ showing individual terms k_i^+ for (a): $n = 0$, (b): $n = 1$, (c): $n = 2$, (d): $n = 3$

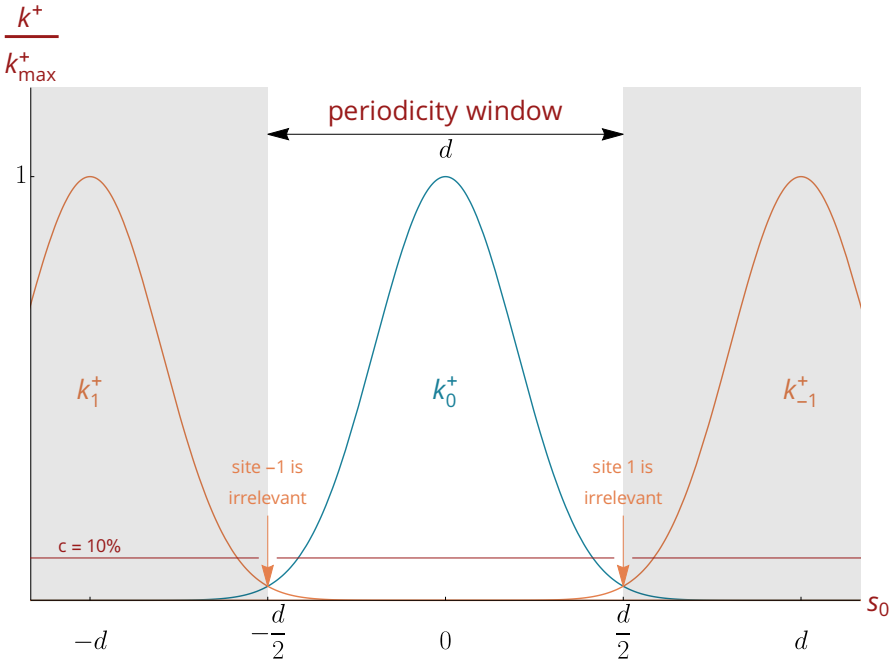

(a) Plotting parameters: $\Delta t = 10^{-4}$, $k_{on} = 10$, $\beta = 2$, $d = 3$, $c = 10\%$.

3.9 Population Equation

The evolution of the system can be described by a population equation describing the evolution of the probability of being in a particular state of the system. We use $p_i^b(s_0, t)$ to describe the probability of being bound to the site i while at a distance s_0 from the closest binding site. To obtain the evolution equation, we count the amount of heads leaving the bound state in a space interval ds during a time dt. The number of heads between s_0 and $s_0 + ds$ bound at the site i at t is equal to $p_i^b(s_0, t)\, ds$. We denote $p_i^u(s_0, t)$ the probability to unbind for a head attached at a binding site i at position s_0 and time t. We therefore have

$$\begin{aligned} p_i^b(s_0, t + dt)\, ds = & k_i^+(s_0)\, p_i^u(s_0, t)\, dtds - k_i^-(s_0)\, p_i^b(s_0, t)\, dtds \\ & + \dot{s_0} p_i^b(s_0, t)\, dt - \dot{s_0} p_i^b(s_0 + ds, t)\, dt + p_i^b(s_0, t)\, ds\,, \end{aligned} \tag{3.39}$$

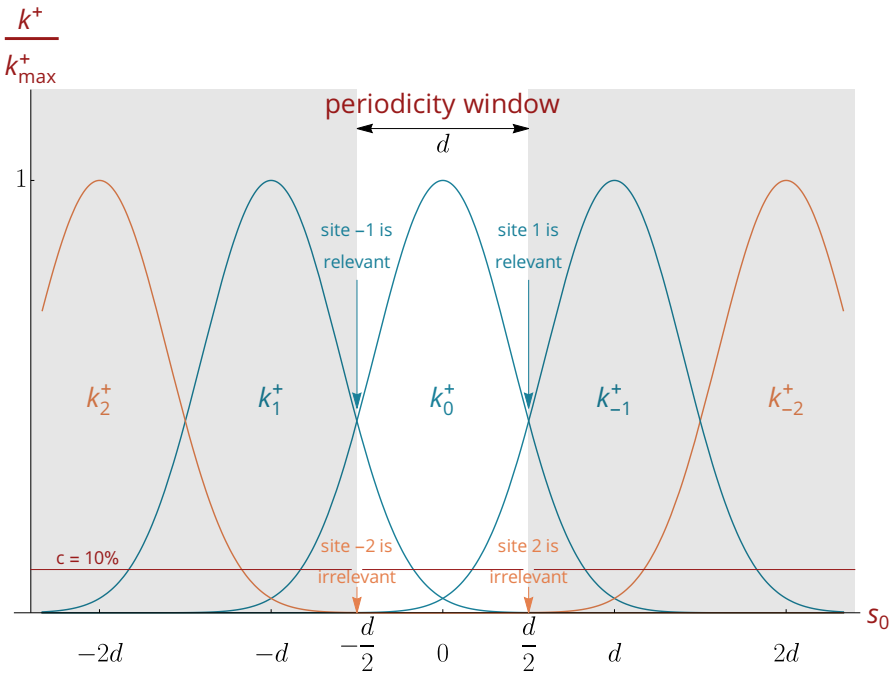

(b) Plotting parameters: $\Delta t = 10^{-4}$, $k_{on} = 10$, $\beta = 2$, $d = 1.5$, $c = 10\%$.

Figure 3.14: The number of relevant binding sites is determined by counting all neighbouring binding sites within the periodicity window which have an attachment rate higher than c relative to the maximum rate of the closest binding site. (a): When binding sites are spaced out, only the closest binding site has a significant attachment rate and is the only relevant site for a given bond. (b): When site spacing is denser, neighbours to the closest binding site do have a significant binding rate when measured at the edges of the periodicity window. Quantitatively, neighbours are considered relevant when their rate at the edges of the window exceeds a ratio c of the highest value of the closest site.

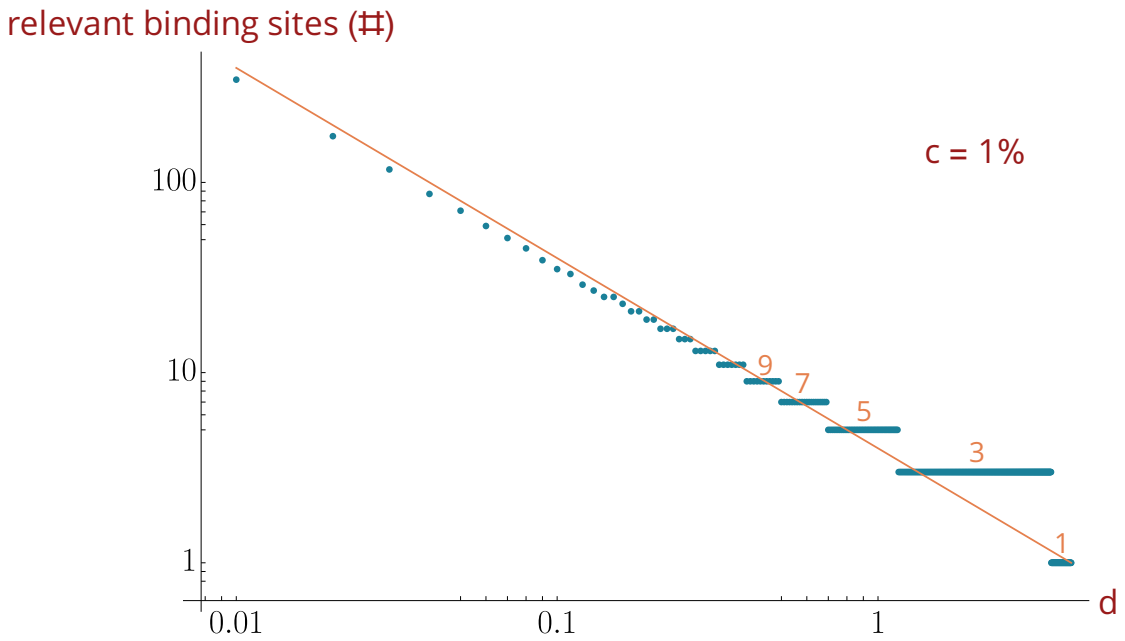

Figure 3.15: Number of relevant binding sites as a function of periodicity given on a log-log-plot, for a c value of 1%. The number of binding sites to consider increases exponentially as the distance between sites decreases. Note that the minimum number of relevant sites is 1, i.e. the closest site to the unbound head. A nonlinear fit is shown as an orange line with parameter values of $y = 4.0x^{-1}$

Plotting parameters: $k_{on} = 10\,, \quad \beta = 2\,, \quad c = 1\%\,.$

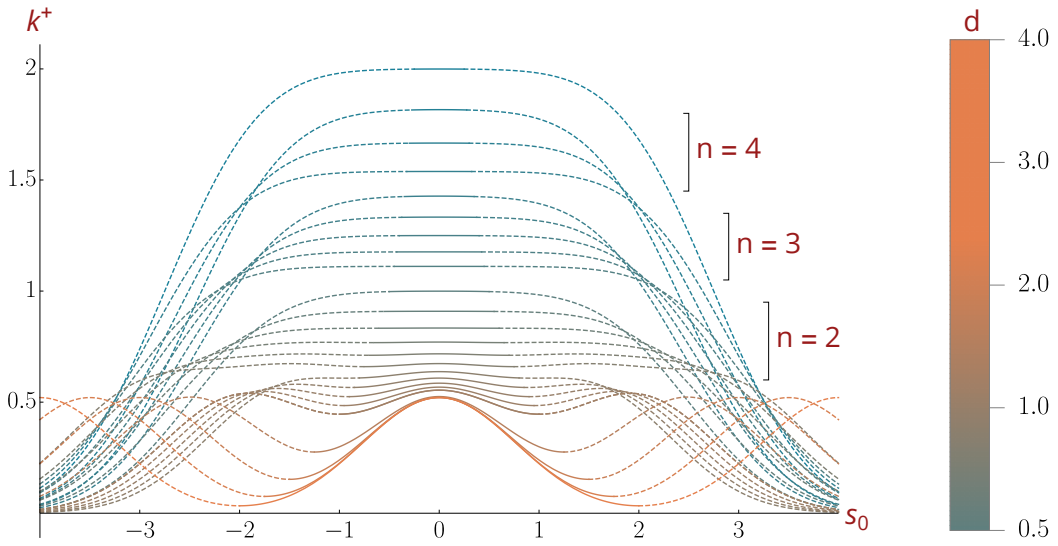

Figure 3.16: $k^+(s_0)$ plotted for decreasing values of d. Continuous line indicates values inside the periodicity window $\pm\frac{d}{2}$, whereas dashed line indicates values outside the periodicity window.

Plotting parameters: $k_{on} = 1\,, \quad \beta = 1\,.$

where the two first terms are the result of bonding and debonding transiting in and out of the bound i state. The next two terms are the convection terms going in and out of the considered space interval of size ds. Dividing both sides by $dsdt$, we obtain:

$$\frac{p_i^b\left(s_0, t+dt\right) - p_i^b\left(s_0, t\right)}{dt} + \dot{s_0}\frac{p_i^b\left(s_0+ds, t\right) - p_i^b\left(s_0, t\right)}{ds} = k_i^+\left(s_0\right) p_i^u\left(s_0, t\right) - k_i^-\left(s_0\right) p_i^b\left(s_0, t\right) . \tag{3.40}$$

In the limit of infinitesimal ds and dt, we thus have

$$\frac{\partial p_i^b\left(s_0, t\right)}{\partial t} + \dot{s_0}\frac{\partial p_i^b\left(s_0, t\right)}{\partial s} = k_i^+\left(s_0\right) p_i^u\left(s_0, t\right) - k_i^-\left(s_0\right) p_i^b\left(s_0, t\right) . \tag{3.41}$$

Due to the nonlinear dependency of the k_i^+ and k_i^- on s_0, the population equations are nonlinear differential equations of $p_i^b\left(s_0, t\right)$.

4 Simulation Procedure

4.1 Framework

The analytical model having being described in section 3, we now describe the framework used to numerically simulate the system behaviour. A Monte-Carlo-type simulation is chosen to represent the system dynamics where a discrete amount N of bonds will be tracked inside a fibre section with periodic boundary conditions, as described in section 3.6. Relevant observations can be made while the system follows two different kinds of loadings: either the relative velocity of the fibres v is imposed (sometimes called a hard device [99, 98]) or the total load F is set while the fibre is free to adjust its position (called a soft device [99]). In the first case F, is monitored while in the latter case, the total fibre displacement s_{tot} is measured. s_{tot} is measured as opposed to v due to the simulation moving in discrete time steps. An instantaneous velocity can be derived by dividing s_{tot} by the timestep.

4.2 Hard Device Case

We've shown in section 3 that the relevant non-dimensionalised space variable to track is the shifted anchor point position of the bond s.

For each detached bond, due to the periodic boundary conditions, one will keep track of s_0, its distance to the closest binding site. Meanwhile, for an attached bond, the

attachment state of each bond—which we call the p-index—describes whether a cross-bridge is attached to the nearest binding site or its closest neighbour, or its neighbour once-removed, and so on... The p-index is thus a relative integer, with 0 for a detached head, 1 for a head attached to the closest binding site, 2 for the neighbour of the closest binding site, 3 for the neighbour once-removed of the closest binding site and so on, so that the length of an attached bond is $s_0 + pd$. The sign of the p-index is used to distinguish binding site directions relative to the closest binding site, so that neighbours with a positive contribution to the total load F have a positive p-index and neighbours with a negative contribution have a negative p-index, following the convention set out in figure 3.12.

Furthermore, periodic boundary conditions are not enforced on attached bonds, since attached bonds can be stretched out of the periodicity window before hitting the forced detachment zone.

s_0, p and the simulation time t constitute the state variables which are tracked for each head in the simulation. Finally, a couple of derived variables are stored in our simulation as a convenience since they are widely used to interpret the model results. The first one is the load generated by each individual bond f. Keeping in mind that the bond's stiffness constant $\widetilde{K}$ is used as the force scaling and therefore $K = 1$, the value of f for an individual bond is:

$$\begin{cases} f &= 0 & if \quad p = 0\,, \\ f &= \frac{1}{1+\frac{1}{\kappa}}\left((p-1)\,d + s_0\right) & if \quad p > 0\,, \\ f &= \frac{1}{1+\frac{1}{\kappa}}\left(pd + s_0\right) & if \quad p < 0\,. \end{cases} \tag{4.1}$$

The second convenience variable is the total load F, which is simply the sum of individual f values at each time step. Table 4.1 gives an overview of variables stored as an output of the simulation. Note that due to the direct correspondence between s_0 and f, only the bond load is stored as a simulation output.

Variable	Symbol	Value
time elapsed	t	scalar
bond load	f	N-length vector
p-index	p	N-length vector
Total load	F	scalar

Table 4.1: Variables stored as an output of the hard device simulation. Simulation inputs are given in table 4.2.

4.3 Hard Device Simulation Procedure

The velocity driving of the hard device means that this simulation can be implemented in a straightforward fixed time step manner. Foremost, a prescribed velocity v is given to the system. A sufficiently small time step Δt is chosen in order to visualize transient phenomena in sufficient detail and a number of iterations $N_{timestep}$ is simulated, sufficiently to obtain a steady-state behaviour of the system. Here Δt (see table 4.2) is taken to be small with respect to the normalizing value of time variables $\frac{1}{\tilde{k}_{off}}$ (see equation 3.30). Next, model parameters k_{on}, κ, β and d are entered to account for the attachment/detachment interactions described in section 3. A sufficiently large number $N \gg 1$ of bonds is initialized in an initial configuration $p_{init} = (\phi_{attached}, \phi_{detached})$ of attachment fraction. The initial configuration $p_{init} = (\phi_{attached}, \phi_{detached})$ is determined by running a simulation with zero driving velocity and taking the final value of attached and detached bond fractions. Finally, a neighbour criterion c is given which determines the number of neighbouring binding sites to consider for attachment of a given bond. As shown in section 3.8, the number of neighbours to consider specified by a periodic model

is infinite with a vanishing bonding probability as distance to the bond becomes large. For a given c, the number of relevant binding sites is given by the largest number n of neighbours which verify the minimum criterion of equation 3.38, where a binding site is considered in the simulation if its maximum bonding probability exceeds a fraction c of the maximum bonding probability of the closest binding site. The general algorithm for the hard device simulation is therefore:

(**a1**) Store the current values of output parameters as summarized in table 4.1.

(**a2**) For each cross-bridge, generate a random number uniformly distributed in $[0; 1]$.

(**a3**) For each cross-bridge, update its p-index following the generated random number. The generated number is tested against the probability of detaching if attached or attaching if detached to all relevant binding sites. If the number is lower or equal to the probability being tested, then the event happens and the p-index is updated accordingly. If an attached cross-bridge moves out of the periodicity window, its p-index is automatically incremented according to the multiplicity of d found in its position s_0.

(**a4**) For each cross-bridge, update its position s_0 by an increment $v\Delta t$.

An example simulation trajectory is plotted in figure 4.1.

4.4 Soft Device

In the case of a soft device, the fibre is considered loaded at the extremity by a given force F. Attachment or detachment events will then have a destabilising effect on the fibre, increasing or decreasing respectively the load on the system. As a result, the whole fibre will then shift by an amount s_{tot} sufficient to return to the prescribed load F, causing an equally distributed shift to the anchor position s_0 of all bonds. The direction of the

Parameter	Symbol	Value
prescribed velocity	v	scalar
number of time step	$N_{timestep}$	scalar
bonding ratio	k_{on}	scalar
stiffness ratio	κ	scalar
energy constant	β	scalar
periodicity	d	scalar
time step value	Δt	scalar
neighbour criterion	c	scalar
bond number	N	scalar
initial p-vector	p_{init}	2-length vector

Table 4.2: Parameters given as input of the hard device simulation. Simulation output of the hard device is given in table 4.1.

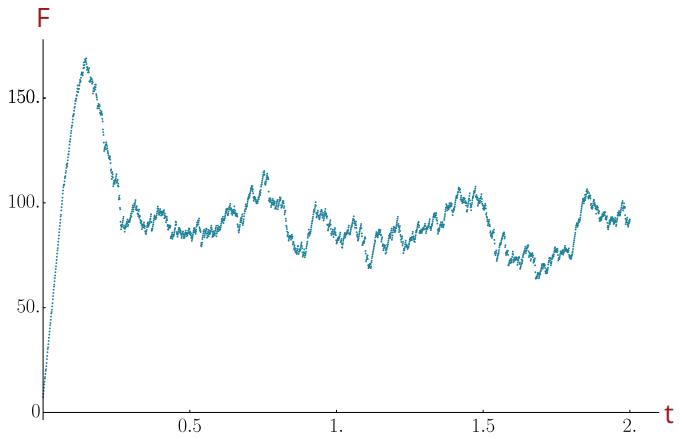

Figure 4.1: Load versus time shown for an example trajectory of the hard device simulation.

Simulation parameters: $N_{timestep} = 2.10^4$, $k_{on} = 10$, $\kappa = 10$, $\beta = 2$, $d = 1.5$, $\Delta t = 10^{-4}$, $c = 1\%$, $N = 200$, $p_{init} = (0.28, 0.72)$, $v = 10$.

fibre shift is chosen such that a detachment event causes a positive shift in position s_0. The main output of the soft device simulation is therefore the positions s_0 of the anchor point of individual cross-bridges and the correction displacement Δs required to return to the prescribed load after a transition event.

The same procedure as in the hard device is adopted, where detached bond heads follow periodic boundary conditions with respect to the closest binding site and attached heads can be stretched indefinitely with regard to the closest binding site. Time elapsed t and head p-indexes are also stored, as summarized in table 4.3

Variable	Symbol	Value
time elapsed	t	scalar
bond positions	s_0	N-length vector
p-index	p	N-length vector
Correction displacement	Δs	scalar

Table 4.3: Variables stored as an output of the soft device simulation. Simulation inputs are given in table 4.4.

4.5 Soft Device Simulation Procedure

4.5.1 Time Step Incrementation

A soft device simulation cannot be run using a straightforward fixed time step approach. Indeed, consider the following problem: one increments the simulation time by a fixed time step Δt. During this time frame, two detachment events occur. The first problem is due to the feedback loop structure of the soft device: when an attachment or detachment event occurs, the position of the whole system is shifted, which may, in turn, cause another event and so on. Thus skipping in time to the end of a fixed time step breaks the chain of causality that accurately portrays the simulation trajectory. Similarly, when multiple events occur during a fixed time step, one has no way of distinguishing the order of these events which, once again, is needed to maintain the causality of the simulation.

The solution to this causality problem is to increment the simulation time step by a variable amount, exactly equal to the waiting time between each individual event. The problem as described above finds a general solution in the Stochastic Simulation Algorithm (SSA), also called Gillespie algorithm [100, 101]. The SSA appropriately models

the soft device because unlike the hard device, no movement of the fibres occurs between cross-bridge transition events. Since the system state does not change in-between transition events, it is appropriate to use an algorithm which skips in time between events, provided that the event distribution is modelled properly.

4.5.2 Distribution of Waiting Times

The SSA calls for determining the distribution of the next time step within the algorithm. Indeed, if one knows the distribution of the next time step, one can generate a sample from this distribution, solving the problem "When does the next transition event occur?". To do this we model transition events as competing Poisson processes in time. Two general hypotheses relative to stochastic processes are made:

1. Transition events occurring within separate time intervals are independent from one another (Markov property).

2. Processes depend on the considered time interval and not on the absolute time position. This property is the invariance with respect to time-translation.

Two further hypotheses relative to Poisson processes specifically are made [102]:

1. The probability that at least one transition event happens within an interval Δt is

$$p\left(\Delta t\right) = k.\Delta t + o\left(\Delta t\right) , \tag{4.2}$$

   where $k > 0$ and $\lim_{\Delta t \to 0} \frac{o(\Delta t)}{\Delta t} = 0$.

2. The probability of two or more events happening at once is $o\left(\Delta t\right)$. This hypothesis can be satisfied in practice if transition events are rare or equivalently, according to the previous hypothesis, by observing the process on a small enough window Δt.

Using these hypotheses, we model the N transition processes by so many Poisson processes, each with a transition rate per unit time k_i. k_i can be either a k^+ or a k^- depending

on whether the cross-bridge number i is attached or detached. Each process describes the evolution of random variable $X_i(t)$ which is a waiting time between cross-bridge transition events. As a starting point, we are looking to determine the expression of the minimum of the N random variables $X_i(t)$, which corresponds to the waiting time until the soonest transition event. The following properties of Poisson processes are used [102]:

1. The waiting time of a Poisson process is exponentially distributed. The corresponding probability density is

$$f_i(t) = k_i e^{-k_i t}, \tag{4.3}$$

with the probability:

$$P(t_1 \leq X_i \leq t_2) = \int_{t_1}^{t_2} f_i(t)\, dt. \tag{4.4}$$

2. The cumulative distribution function of a process is

$$F_i(t) = 1 - e^{-k_i t}, \tag{4.5}$$

with the probability:

$$P(X_i \leq t) = F_i(t). \tag{4.6}$$

We start by expressing the complementary of $F_{\text{Min}\{X_1,X_2,...,X_N\}}$, the cumulative distribution function of the minima of the processes X_i. We have the equality:

$$1 - F_{\text{Min}\{X_1,X_2,...,X_N\}}(t) = 1 - P(\text{Min}(\{X_1, X_2, ..., X_N\}) \leq t). \tag{4.7}$$

Furthermore,

$$
\begin{aligned}
1 - P\left(\mathrm{Min}\left(\{X_1, X_2, ..., X_N\}\right) \leq t\right) &= P\left(\mathrm{Min}\left(\{X_1, X_2, ..., X_N\}\right) > t\right) \\
&= P\left(X_1 > t, X_2 > t, ..., X_N > t\right) \\
&= \prod_{i=1}^{N} P\left(X_i > t\right) \quad (X_i \text{ are independent}) \\
&= \prod_{i=1}^{N} \left(1 - F_i\left(t\right)\right) \\
&= \prod_{i=1}^{N} \left(1 - \left(1 - e^{-k_i t}\right)\right) \\
&= e^{-t\sum_i k_i}
\end{aligned}
\tag{4.8}
$$

Finally,

$$
F_{\mathrm{Min}\{X_1, X_2, ..., X_N\}}\left(t\right) = 1 - e^{-t\sum_i k_i}\,. \tag{4.9}
$$

We have thus shown that this cumulative distribution function has the correct form for a corresponding exponential probability density function with a parameter $\sum_i k_i$. The waiting time until the next transition event can therefore be obtained by generating a random variate of a single Poisson process with a parameter that is the sum of all the parameters of the competing processes.

4.5.3 Random Variate Generation

In order to generate a random variate from the exponential distribution of the waiting time minima, we use the inverse method [103], where we compute the inverse function of the cumulated distribution function of the exponential distribution. The cumulated distribution function of the waiting time minima is

$$
F_{\mathrm{Min}\{X_1, X_2, ..., X_N\}}\left(t\right) = 1 - e^{-t\sum_i k_i}\,. \tag{4.10}
$$

This function can be easily inverted to

$$
F^{-1}_{\mathrm{Min}\{X_1, X_2, ..., X_N\}}\left(u\right) = -\frac{\ln\left(1 - u\right)}{\sum_i k_i}\,. \tag{4.11}
$$

Furthermore, since for $u \in [0;1]$, we also have $\hat{u} = 1 - u \in [0;1]$, the expression we use to generate random variates is

$$F^{-1}_{\text{Min}\{X_1,X_2,...,X_N\}}(\hat{u}) = -\frac{\ln(\hat{u})}{\sum_i k_i}, \tag{4.12}$$

where $\hat{u} \in [0;1]$. The simplicity of this expression renders it naturally suitable to be used inside the SSA, as opposed to other methods such as the rejection method or the table method [103].

4.5.4 Choice of the Transition Event

Before moving on with the Stochastic Simulation Algorithm, one final question must be adressed. Once the waiting time until the next reaction has been determined, which of the N cross-bridges is chosen to experience a transition event? Let $N_i(t)$ be the random variable counting the number of events happening to the i-th cross-bridge between 0 and t. Similarly, $N(t)$ will be the random variable counting the total number of events. The probability for a specific cross-bridge i to have the minimal waiting time is

$$P(X_i = \text{Min}(\{X_1, X_2, ..., X_N\})) = P(N_i(t+dt) - N_i(t) > 0 | N(t+dt) - N(t) > 0). \tag{4.13}$$

The SSA algorithm ensures that during one time interval dt, only a single event takes place. This translates to

$$\begin{aligned} P(X_i = \text{Min}(\{X_1, X_2, ..., X_N\})) &= P(N_i(t+dt) - N_i(t) = 1 | N(t+dt) - N(t) = 1) \\ &= \frac{P(N_i(t+dt) - N_i(t) = 1 \cap N(t+dt) - N(t) = 1)}{P(N(t+dt) - N(t) = 1)} \\ &= \frac{P(N_i(t+dt) - N_i(t) = 1)}{P(N(t+dt) - N(t) = 1)} \end{aligned} \tag{4.14}$$

Using the property of a Poisson process, the probability of the random variable $N_i(t)$ being equal to m is given by $P(N_i(t) = m) = \frac{(k_i t)^m}{m!} e^{-k_i t}$. Therefore,

$$P(X_i = \text{Min}(\{X_1, X_2, ..., X_N\})) = \frac{e^{-k_i dt} k_i dt}{e^{-\sum_i k_i dt} \sum_i k_i dt}, \tag{4.15}$$

which, when $dt \to 0$:

$$P(X_i = \text{Min}(\{X_1, X_2, ..., X_N\})) = \frac{k_i}{\sum_i k_i}. \tag{4.16}$$

We thus have the intuitive result that the probability of choosing a given cross-bridge i as the next transition event is given by the weight of its transition rate relative to the sum total of transition rates of all cross-bridges.

4.5.5 Soft Device Algorithm

The parameters given in input of the soft device simulation are summarized in table 4.4. The general algorithm for the soft device simulation is as follows:

(**b1**) Store the current values of output parameters as summarized in table 4.3.

(**b2**) Check whether some cross-bridges have moved out of the Kramers validity zone given by $s_0 = \frac{1+\kappa}{2}$. If so, a detachment event happens right away (no waiting time) to the cross-bridge with the highest s_0, and go to (**b6**).

(**b3**) Generate a random number u uniformly distributed in $[0; 1]$.

(**b4**) Generate a waiting time until the next reaction given by $-\frac{\ln(u)}{\sum_i k_i}$.

(**b5**) Choose the cross-bridge to undergo a transition event by performing a weighted random choice among all cross-bridges with the weight $\frac{k_i}{\sum_i k_i}$ for the i-th cross-bridge.

(**b6**) Adjust the p-index of the cross-bridge undergoing the transition.

Parameter	Symbol	Value
prescribed load	f	scalar
number of time step	$N_{timestep}$	scalar
bonding ratio	k_{on}	scalar
stiffness ratio	κ	scalar
energy constant	β	scalar
periodicity	d	scalar
neighbour criterion	c	scalar
bond number	N	scalar
initial p-vector	p_{init}	2-length vector

Table 4.4: Parameters given as input of the soft device simulation. Simulation output of the soft device is given in table 4.3.

(**b7**) Calculate the change in system load Δf that the transition would cause.

(**b8**) For each cross bridge, adjust s_0 evenly by the correct amount to offset the loading change Δf and return to the prescribed load f.

(**b9**) Increment the simulation time by the generated waiting time and go back to (**b1**).

An example of simulated trajectory is plotted in figure 4.2.

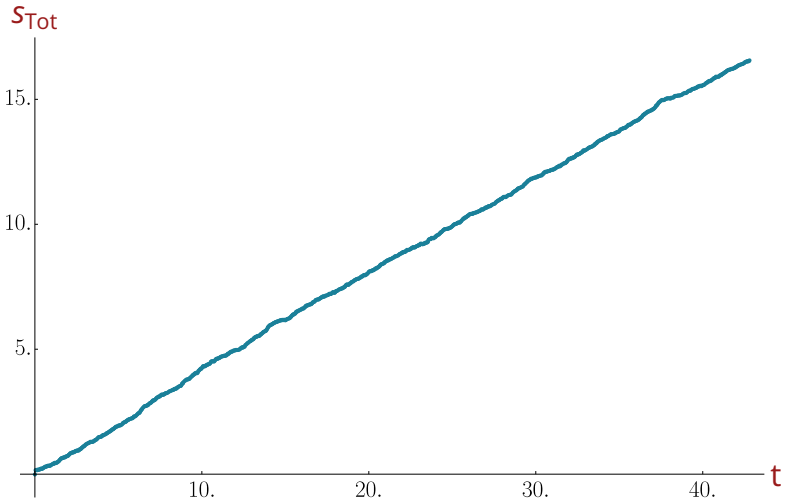

Figure 4.2: Displacement s_{tot} versus time shown for an example trajectory of the soft device simulation.
Simulation parameters: $N_{timestep} = 2.10^4$, $k_{on} = 10$, $\kappa = 10$, $\beta = 2$, $d = 1.5$, $c = 1\%$, $N = 200$, $p_{init} = (0.24, 0.76)$, $f = 20$.

5 Simulation Results - Initial Model

In this section we present the main results of the simulation of the sliding fibre system. The steady-state regime and the transient regime of the hard device are examined, and following that the results of the soft device are analysed. Finally, the influence of binding site spacing as well as cyclic loading are investigated.

5.1 Hard Device

In order to get a sense of the behaviour of the system, we first perform a speed-driven simulation, at a prescribed velocity v. The system will then exhibit a variable load $F(t)$ as a result of the various bonds attached to sites at a given moment and resisting the movement. Figure 5.1 represents multiple trajectories of the simulation for the same prescribed v. The load on the fibre initially increases linearly with time and then drops from a peak value to a steady-state plateau. In this final regime, the load exhibits fluctuations around a final value, which we denote by F_∞.

5.1.1 Steady-State Regime

We first describe the steady-state regime, where the load fluctuates around a plateau value F_∞ and then we move on to describe the transient initial regime, where the load peaks in a linear fashion.

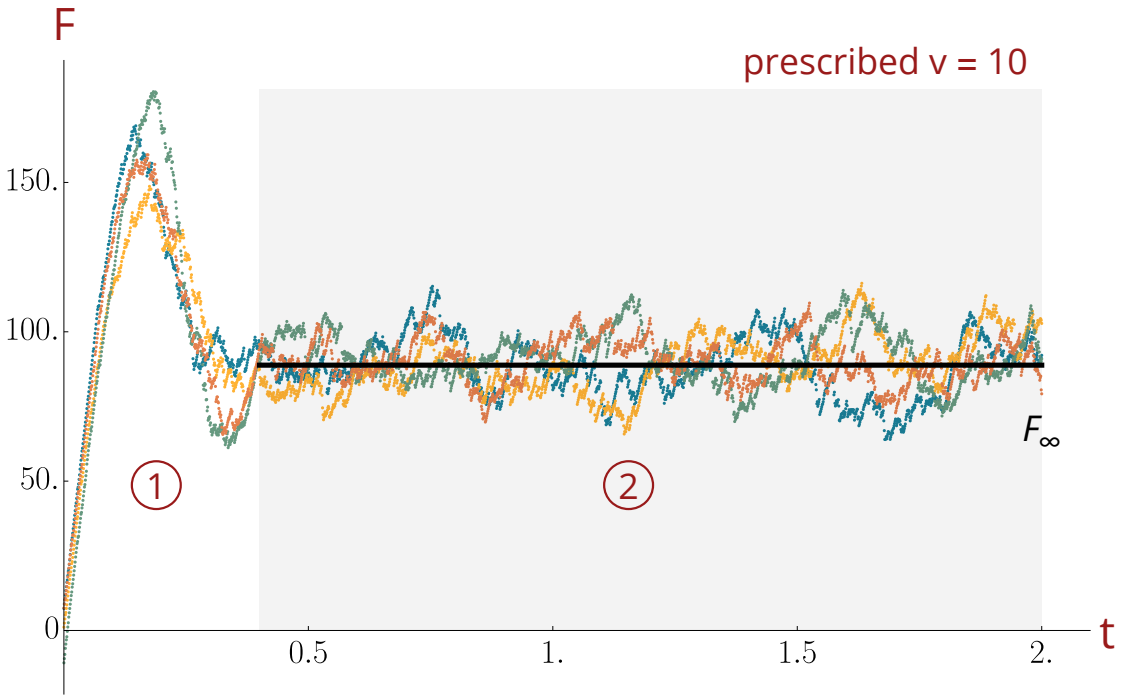

Figure 5.1: Total load in the system F versus time t shown for multiple trajectories and for prescribed velocity $v = 10$. F_∞ visualizes the average value taken by F once the permanent regime has been reached.

① Transient regime. ② Steady-state regime.

Simulation parameters: $N_{timestep} = 2.10^4$, $k_{on} = 10$, $\kappa = 10$, $\beta = 2$, $d = 1.5$, $\Delta t = 10^{-4}$, $c = 1\%$, $N = 200$, $p_{init} = (0.28, 0.72)$, $v = 10$.

Drawing, for various v, the average trajectories of at least $n = 20$ realisations, as done in figure 5.2, confirms the generality of this behaviour and furthermore hints that the prescribed sliding velocity v has a non-linear effect on the value of F_∞. A wider overview

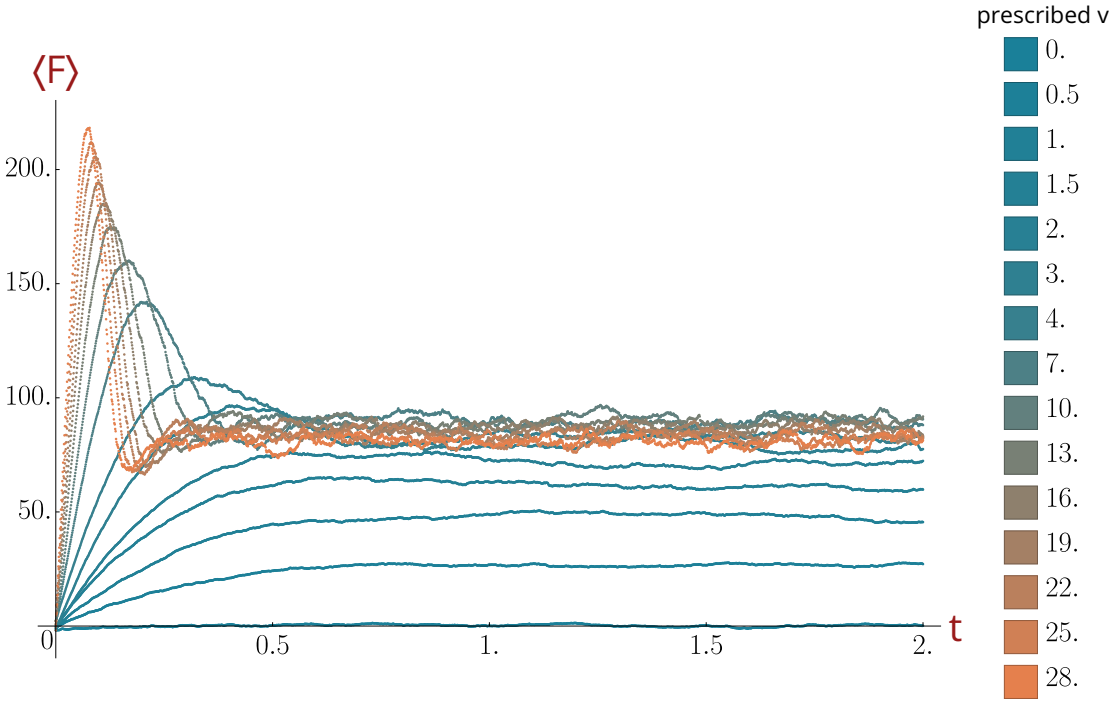

Figure 5.2: Average value $\langle F \rangle (t)$ as a function of time t for increasing sliding velocity v.

Each curve is the average of $n = 20$ simulations.

Simulation parameters: $N_{timestep} = 2.10^4$, $k_{on} = 10$, $\kappa = 10$, $\beta = 2$, $d = 1.5$, $\Delta t = 10^{-4}$, $c = 1\%$, $N = 200$, $p_{init} = (0.24, 0.76)$.

of the system behaviour can be obtained by looking at $F_\infty (v)$, drawn in figure 5.3, which describes how much resistance at steady-state the system opposes to a given speed v of solicitation. The force-velocity curve of the system is indeed non-monotonous: initially, as the sliding velocity increases, the steady-state force of the system increases almost linearly. After a given velocity however, F_∞ stops increasing and begins a slower decrease, as reported in the literature [96, 90].

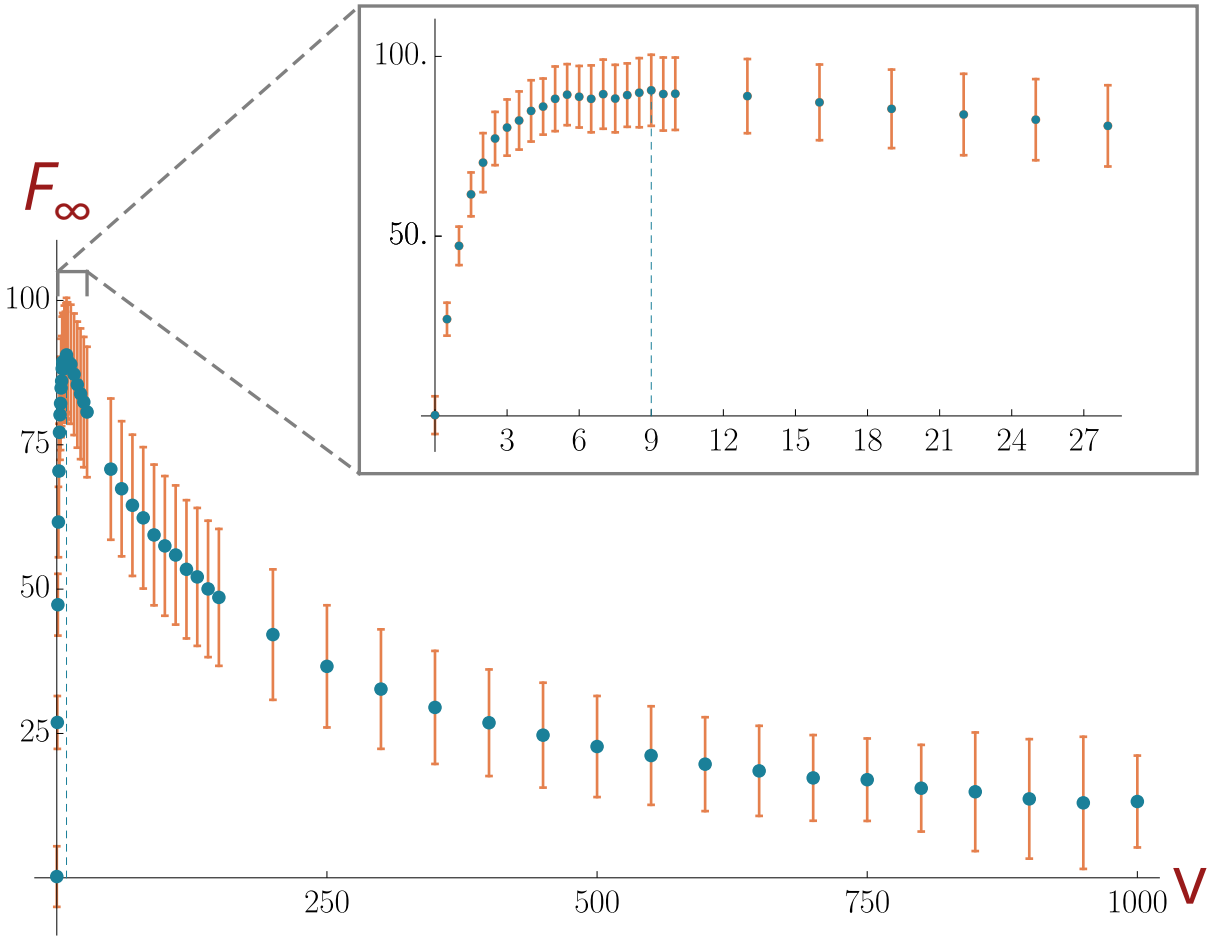

Figure 5.3: Steady-state load F_∞ versus prescribed sliding velocity v. Bars indicate the size of fluctuations at steady-state around the average F_∞ value. These bars are calculated as the standard deviation of F once steady-state has been reached, averaged over all $n = 20$ trajectories of the simulation. Inset shows a zoom around the peak of load-velocity curve. Simulation parameters as in figure 5.2.

A comparison of figure 5.2 and the corresponding fraction of attached bonds $\phi_{attached}$, shown in figure 5.4, seems appropriate to understand the underlying behaviour of the system. Indeed, one should expect $\phi_{attached}$ to behave similarly to F, as

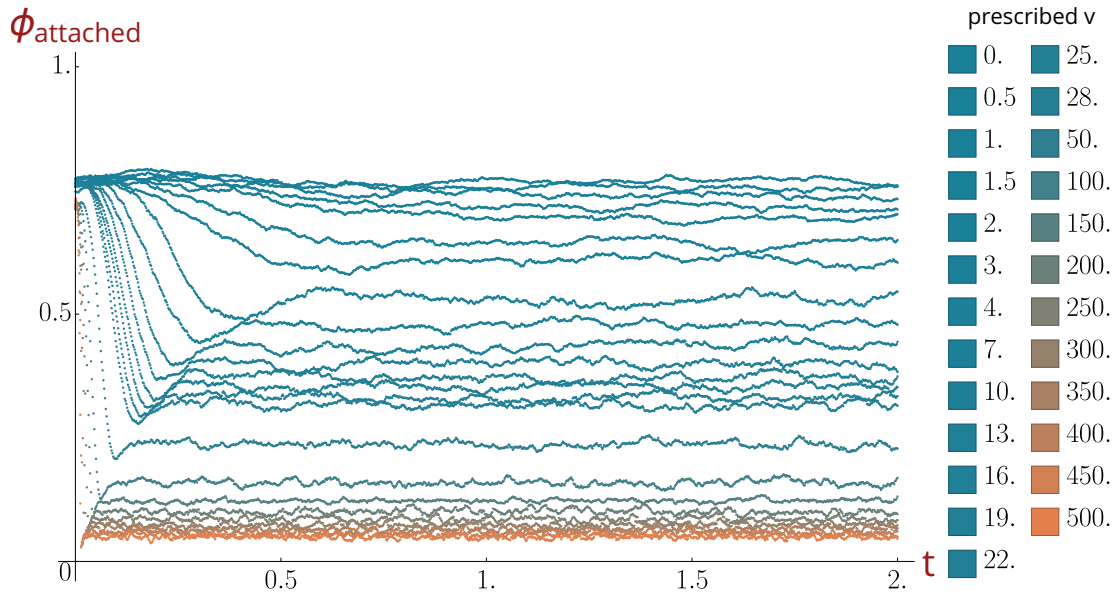

Figure 5.4: Average fraction of attached bonds $\phi_{attached}$ as a function of time, plotted for different values of prescribed v. The initial state has 76% of the bonds attached. Simulation parameters as in figure 5.2

$$F = \sum_{i}^{N} \alpha_p K s_0 \,, \quad \begin{cases} \alpha_p = 0 & \text{if} \quad p = 0 \\ \alpha_p = 1 & \text{if} \quad p \neq 0 \end{cases} \tag{5.1}$$

with $K = 1$ according to the non-dimensionalisation convention. Therefore, the higher $\phi_{attached}$, the more bonds with $\alpha_p \neq 0$ and the higher the load generated. However, figure 5.4 clearly shows a monotonous behaviour for the same range of prescribed v: the faster the prescribed sliding, the smaller the amount of attached heads. This monotonous behaviour continues uninterrupted at high speeds as shown in figure 5.4. A more detailed look at the attachment state of bonds during the experiment reveals the source of this

discrepancy. As discussed previously, we simulate only bonds in the range $-\frac{d}{2}$ to $\frac{d}{2}$, but bonds can be outside of this range. Bonds attached further along the fibre, naturally produce a higher load on the system due to the increased stretch. Recalling equation 4.1:

$$\begin{cases} f &= 0 & if \quad p = 0\,, \\ f &= \frac{1}{1+\frac{1}{\kappa}}\left(\left(p-1\right)d + s_0\right) & if \quad p > 0\,, \\ f &= \frac{1}{1+\frac{1}{\kappa}}\left(pd + s_0\right) & if \quad p < 0\,, \end{cases}$$

a head which is attached farther from the closest binding site contributes a higher load—in positive or negative—by an amount $(p-1)\,d$ if positive and pd if negative. Figure 5.5 shows the evolution of the p-index in the system for increasing velocity. A visual survey of the figure shows two clear trends. First, from a steady-state where nearly three quarters of bonds are attached, as v increases, the equilibrium clearly shifts to favouring a steady-state where three-quarters of bonds are detached. This effect generates decreased load as v increases. Second, among attached bonds, when v increases, higher p-indexes are favoured, as evidenced by the gradual population of higher states. Since higher p means higher stretch on a given bond, this effect results in increased load as v increases. Therefore, the non-monotonicity of figure 5.3 seems to be the result of these two competing effects, with the decrease of attached bonds being the most prominent at high velocities.

Additionally, we put forward an intuitive explanation: introducing $\langle s \rangle$, the average elongation of cross-bridges in the system, we have approximately

$$F \propto K \langle s \rangle N \phi_{attached}\,. \tag{5.2}$$

When v increases, bound heads are more stretched, so $\langle s \rangle$ increases, which increases F, according to relation 5.2. Simultaneously, when the fibre velocity v increases, cross-bridges spend less time being attached due to increased detachment rate with stretching. This decreases $\phi_{attached}$ and therefore, according to relation 5.2, decreases F as well.

The increase of bonds with higher p-indexes is the result of the larger rate of convection of binding sites within the range of a given head. These results are consistent with those found in Sens [96]. Taken as a whole, this phenomenon generates a testable prediction of the model: were a real system to behave following this model, it would not only follow the rheological force-velocity curve, but it would also exhibit increased load per bond or per binding site, irrespective of the total load of the system. An experimental validation of these results can be suggested: if one can generate a fiber network with stretch sensors as linkers, such as Fluorescence Resonance Transfer (FRET) systems [104], the stretch distribution and the average stretch value of the system can be accessed. One can then experimentally verify the increase of $\langle s \rangle$ when prescribed v increases.

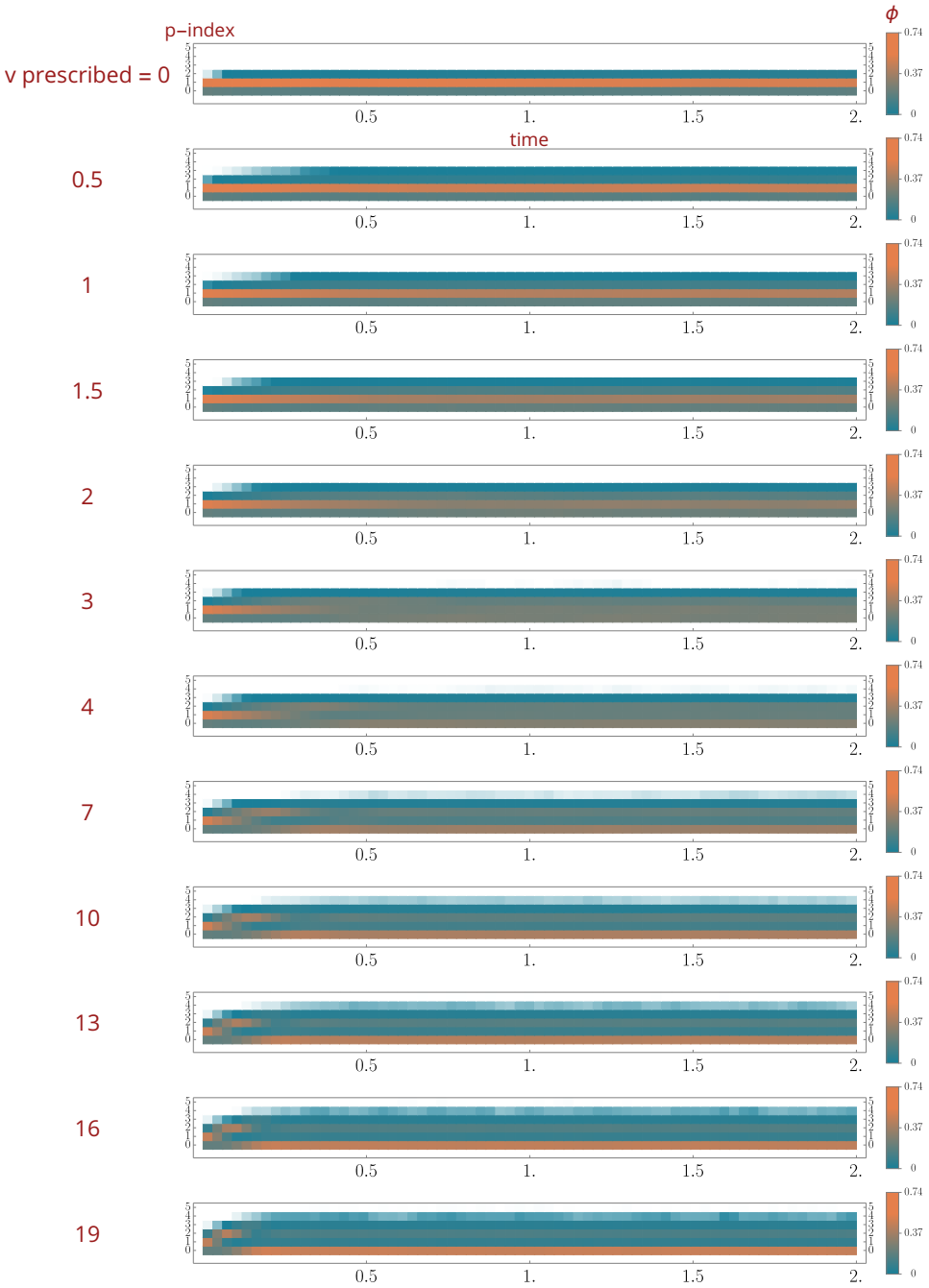
p–index
v prescribed = 0
time
0.5
1
1.5
2
3
4
7
10
13
16
19
ϕ
0.74
0.37
0
0.5
1.
1.5
2.

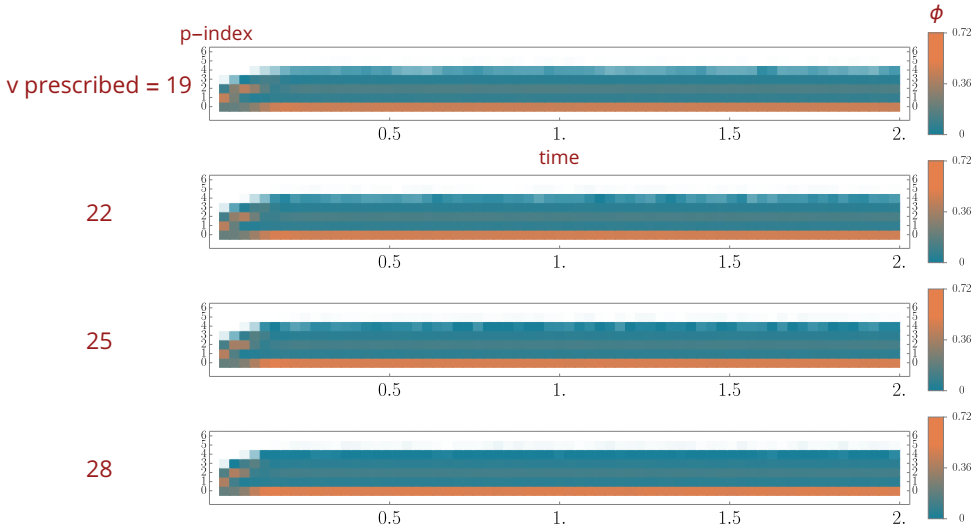

Figure 5.5: Evolution of attachment and detachment fraction ϕ with respect to time for various prescribed velocity. The p-index value indicates attachment state of bonds: 0 for a detached head, 1 for a head attached to the closest binding site, 2 for a head attached to the neighbour of the closest binding site and so on... For visualisation purposes, the data has been down sampled by a factor of 300, such that every square shown represents the average fraction over 300 time steps. Squares with an intermediate colour between transparent and blue have a value $\phi < 1\%$. Simulation parameters as in figure 5.2.

5.1.2 Transient Regime

We now describe the transient regime observed in figure 5.1 (phase 1). The transient regime is characterized by a quasi-linear increase in load F, then a rapid drop and a small overshoot towards the value of F_∞. Assuming a linear response for the transient $F(t)$, its slope increases near-linearly when v increases, as shown on figure 5.6. This phenomenon can be more precisely visualized by charting the distribution of positions

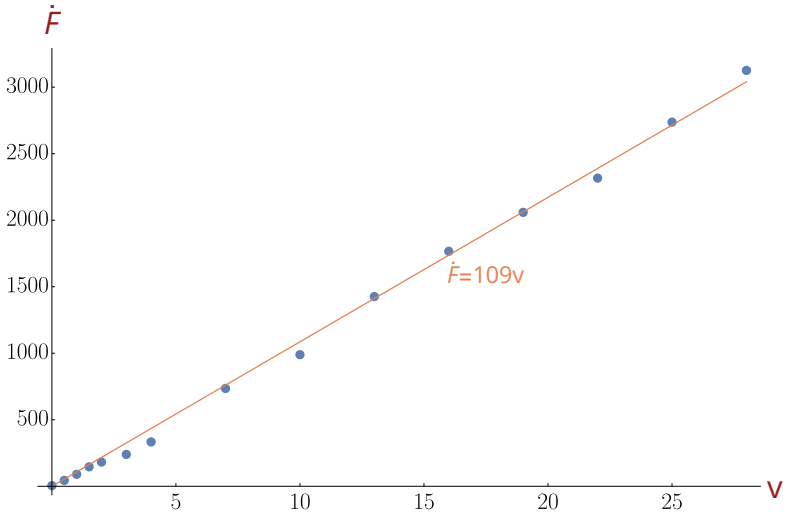

Figure 5.6: Slope $\dot{F}$ of the transient $F(t)$, assuming a linear increase, slope plotted against prescribed sliding velocity v. A linear fit of the data is shown in orange. Simulation parameters as in figure 5.2.

s_0 of attached heads for a given time, as done in figure 5.7. At $t = 0$, the attached heads are spread out evenly around their binding site at $s_0 = 0$, consistent with a uniform initial condition (see figure 5.7a). When the fibre starts moving, as in figure 5.7b, the whole distribution is convected to higher s_0: most of the cross-bridges are being stretched with only a few detaching and reattaching close to the binding site. This stretching of a group of cross-bridges with little detachment is responsible for the quasi-linear increase in load, which occurs until the block-stretching of cross-bridges is sufficient to induce a mass detachment and subsequent reattachment. Mass detachment takes place because attached cross-bridges can only be stretched for a finite amount before reaching the forced detachment zone, as shown on figure 3.5. This means that the translation in space of the initial condition can only go so far before triggering the forced detachment of individual heads. Once mass detachment has occurred, cross-bridges are redistributed in a wider bell-shaped curve, shown on figure 5.7c, typical of the steady-state regime. Another way

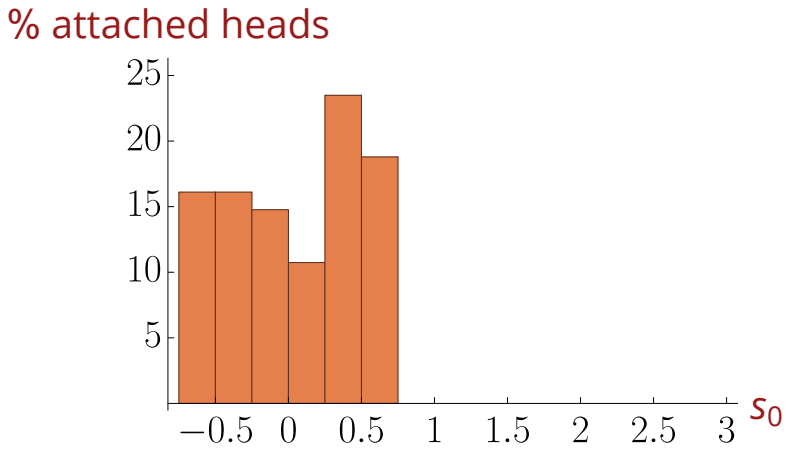

(a) $t = 0$

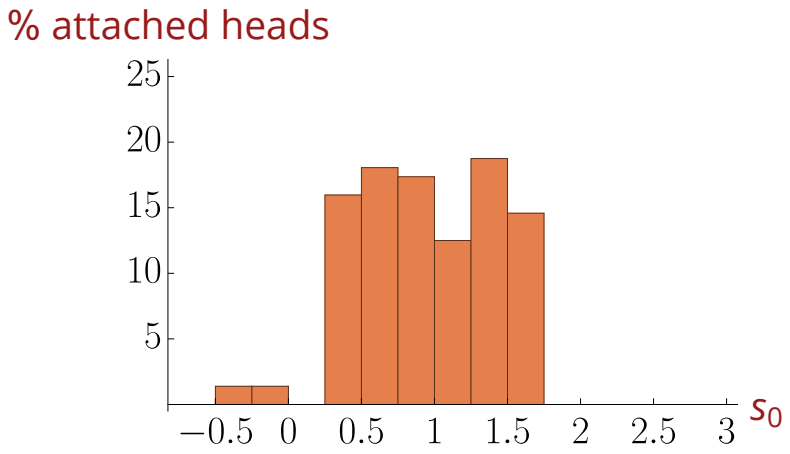

(b) $t = 0.05\, t_{max}$

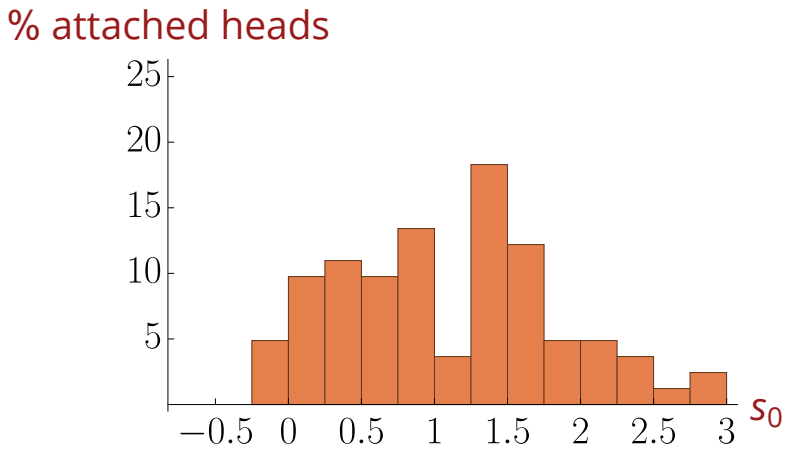

(c) $t = 0.95\, t_{max}$

Figure 5.7: Histogram of the s_0 distribution at 3 times of the simulation. (a): $t = 0$. (b): $t = 0.05 t_{max} = 0.1$. (c): $t = 0.95 t_{max} = 1.9$.

Simulation parameters: $N_{timestep} = 2.10^4$, $k_{on} = 10$, $\kappa = 10$, $\beta = 2$, $d = 1.5$, $\Delta t = 10^{-4}$, $c = 1\%$, $N = 200$, $p_{init} = (0.28, 0.72)$, $v = 10$.

to represent this effect is to plot the density of s_0 as a function of time, as in figure 5.8.

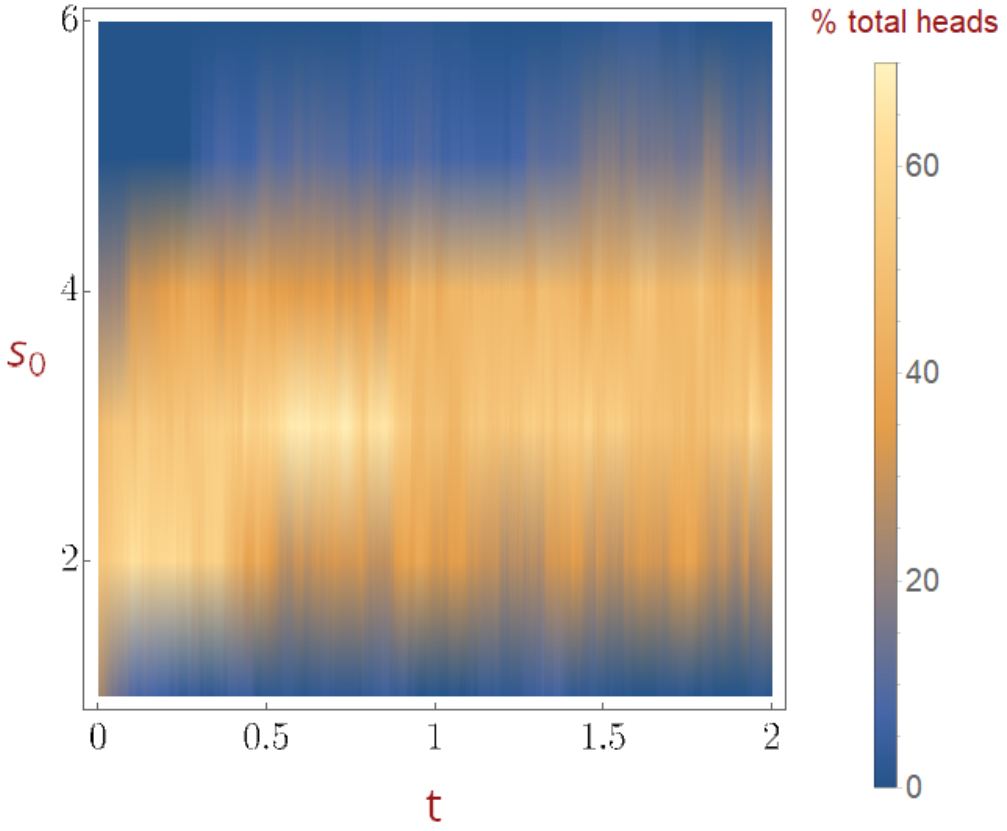
% total heads
60
40
20
0
6
4
2
s_0
0
0.5
1
1.5
2
t

(a) $v = 1$

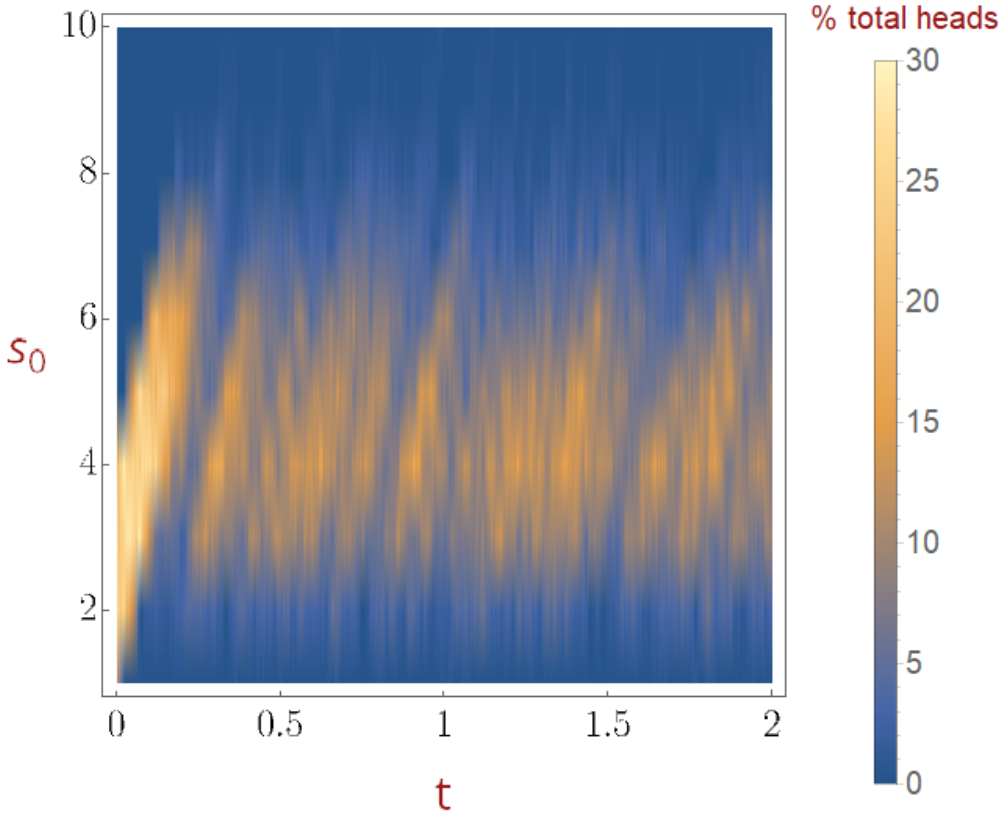
% total heads
30
25
20
15
10
5
0
10
8
6
4
2
s_0
0
0.5
1
1.5
2
t

(b) $v = 10$

In figure 5.8a, no transient regime can be observed as the advection is slower than attachment / detachment of the heads. Meanwhile, In figures 5.8b and 5.8c, transient and steady state regimes can be clearly delineated. The transient regime is characterized by a convection of a high proportion of attached heads with little detachment, whereas in the steady-state the s_0 distribution is wider and fluctuates within a large stable band. Furthermore, we see that the prescribed sliding velocity v affects this behaviour. At low v, the convection effect is weak and the system exhibits almost no transient regime and shifts immediately to the stable, wide distribution of s_0. At high v, the convection effect is strong as shown by the fact that attached heads stay attached during the entire transient regime. The transient regime is shorter, as the cross-bridges are stretched faster and the load values reached are also higher. This behaviour indicates that the transient regime is the signature of the interaction between the loading and a given initial condition. In this case we also observe that the state where $\langle F \rangle = 0$ does not necessarily imply that no cross-bridges are bound, rather bound cross-bridges can be attached but compensate each other in applied loading.

Finally, one can also observe during the steady-state regime at high velocities, that the system exhibits many small convection events with a sharp alternating of attached convection and mass detachment. We suggest that these smaller convection episodes are generated by random attachment events, where the stochastic nature of attachment / detachment causes cross-bridges to be attached in group. These groups are then dragged by the system, causing the convection signature mentioned previously.

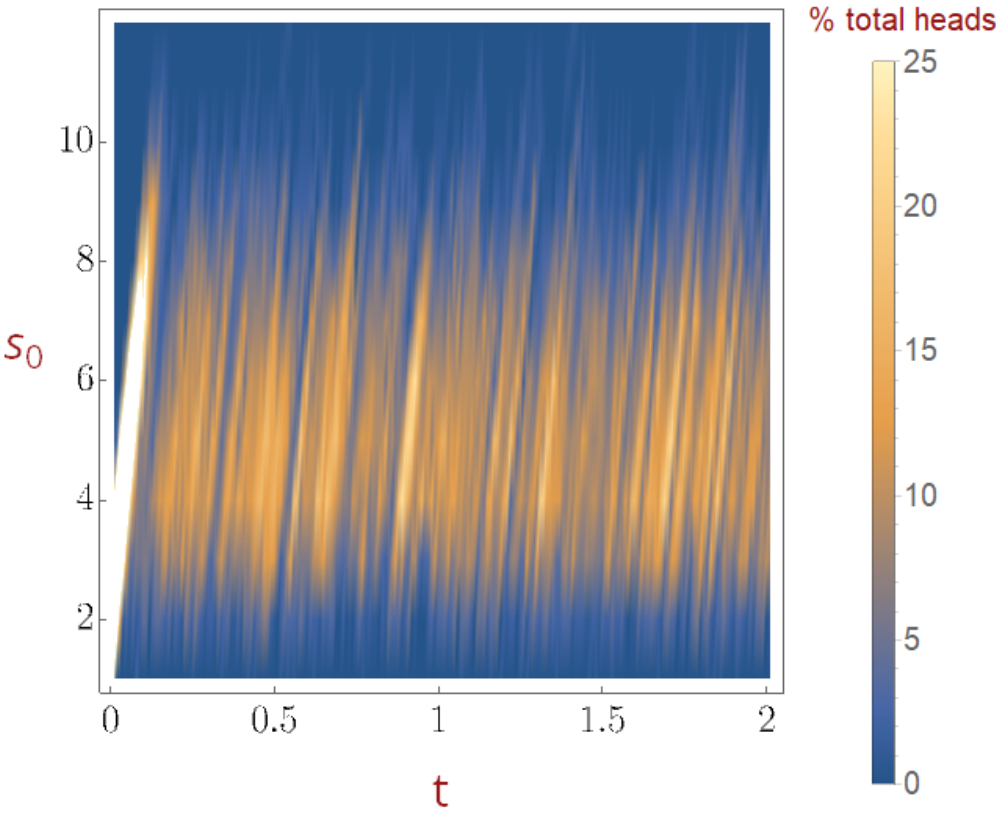

(c) $v = 28$

Figure 5.8: Density plots of the s_0 distribution versus time for different sliding velocities.

(a): $v = 1$. (b): $v = 10$. (c): $v = 28$.

Simulation parameters: as in figure 5.7.

5.2 Soft Device

5.2.1 Steady-state Regime

A load-driven experiment is performed, where one end of the system is given a prescribed load and the fibre is free to slide in either direction. The loaded end of the fibre is taken to be positive while the opposite direction is denoted negatively. When a single cross-bridge attaches or detaches, it causes a change in total load F (an increase for an attachment and a decrease for a detachment). The system will then adjust itself to return to the prescribed load. This adjustment comes in the form of fibre sliding of a length Δs. The system is then at rest until the next attachment or detachment event occurs. We denote Δs the fibre displacement caused by a single attachment / detachment event and s_{tot} the aggregate displacement of the fibre.

Figure 5.9 represents multiple trajectories of the load-driven experiment for a single prescribed f. For a constant loading, multiple trajectories of the same set of parameter show a generally similar linear ramp response $s_{tot}\,(t)$.

In order to visualise the ensemble behaviour of the load-driven system, we seek to represent the average over all trajectories of the displacement s_{tot} versus time of the fibre. However, as described in section 4.5, each simulation trajectory is drawn over a variable time step distributed according to a Poisson process. This means that the time discretization of each trajectory is different, preventing a straightforward averaging as with a fixed time step. We therefore produce an interpolated curve of each trajectory through a first order Hermite interpolation. The interpolated trajectories are then averaged over a fixed time step to produce the averaged curve $\langle s_{tot} \rangle\,(t)$. The result, seen in figure 5.10, shows linear sliding of the fibre with increasing speed as the prescribed loading f increases. Some dispersion of the slope of the response is observed, as shown in figure 5.11a for $f = 20$ and figure 5.11b for $f = 80$.

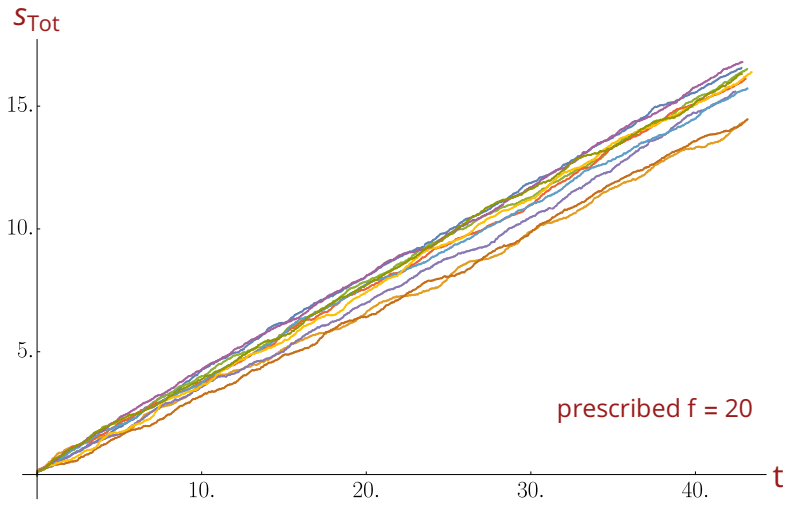

Figure 5.9: Aggregate fibre displacement s_{tot} versus time t shown for multiple trajectories and prescribed load $f = 20$.
Simulation parameters: $N_{timestep} = 2.10^4$, $k_{on} = 10$, $\kappa = 10$, $\beta = 2$, $d = 1.5$, $c = 1\%$, $N = 200$, $p_{init} = (0.24, 0.76)$, $f = 20$.

Higher prescribed f, such as shown on figure 5.12, are excluded from figure 5.10 because they present total detachment of the fibre during the simulation. Total detachment is characterized by the rapid increase of s_{tot}, leading to a divergence in displacement. This is due to cross-bridge detachment causing an increased load on the other attached heads, leading to cascading detachment until all cross-bridges are detached. Figure 5.12 shows that these trajectories present much shorter simulation time and higher variance due to the onset of total detachment, making the averaging of such trajectories meaningless.
Using the average displacement $\langle s_{tot} \rangle$ from figure 5.10, one can obtain the average velocity $\langle v \rangle$ of the fibre as the slope of the curve $\langle s_{tot} \rangle (t)$. Using a linear fit of $\langle s_{tot} \rangle (t)$ we extract the velocity v of the system which is used to plot the velocity-load curve as shown on figure 5.13. Figure 5.13 intuitively shows that the higher the loading on one end of the fibre the faster the sliding velocity of the fibre in the loading direction. The velocity-

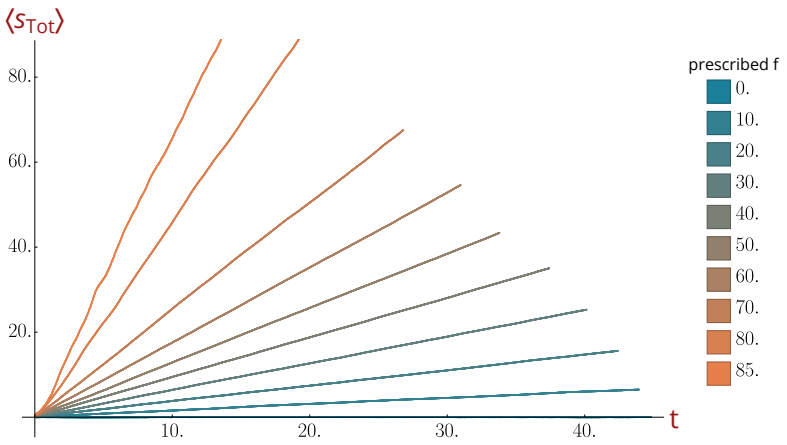

Figure 5.10: Aggregate fibre displacement $\langle s_{tot} \rangle$ averaged over 20 trajectories versus time for different prescribed load f. All displacement are drawn for the same number of iterations.

Simulation parameters: $N_{timestep} = 2.10^4$, $k_{on} = 10$, $\kappa = 10$, $\beta = 2$, $d = 1.5$, $c = 1\%$, $N = 200$, $p_{init} = (0.24, 0.76)$, interpolation step: 10^{-2}.

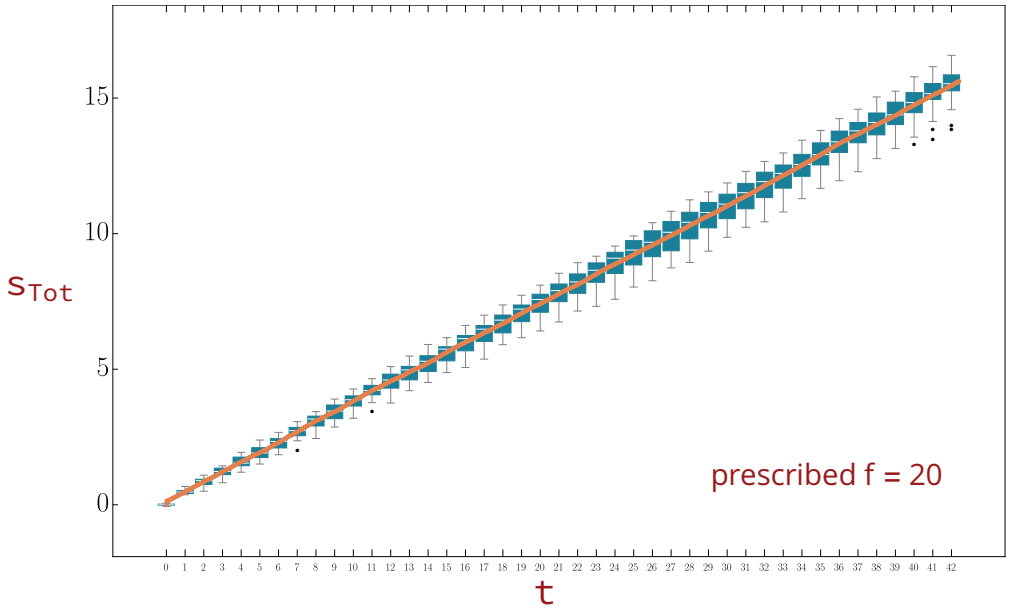

(a) $f = 20$.

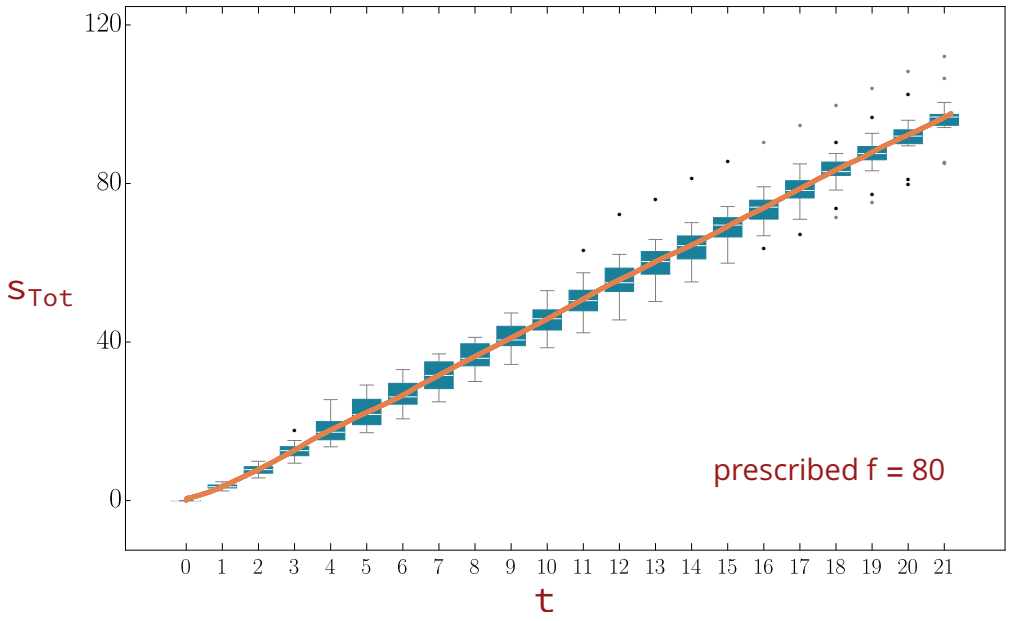

(b) $f = 80$.

Figure 5.11: Boxplot showing the dispersion of trajectories for two prescribed loads (a): f=20 and (b): f=80. Boxes span the first to third quartile and the median is indicated by a white line. Whiskers show max and min values and outliers are shown as a dot. The orange line indicates the average aggregate displacement $\langle s_{tot} \rangle$.

Simulation parameters: $N_{timestep} = 2.10^4$, $k_{on} = 10$, $\kappa = 10$, $\beta = 2$, $d = 1.5$, $c = 1\%$, $N = 200$, $p_{init} = (0.24, 0.76)$.

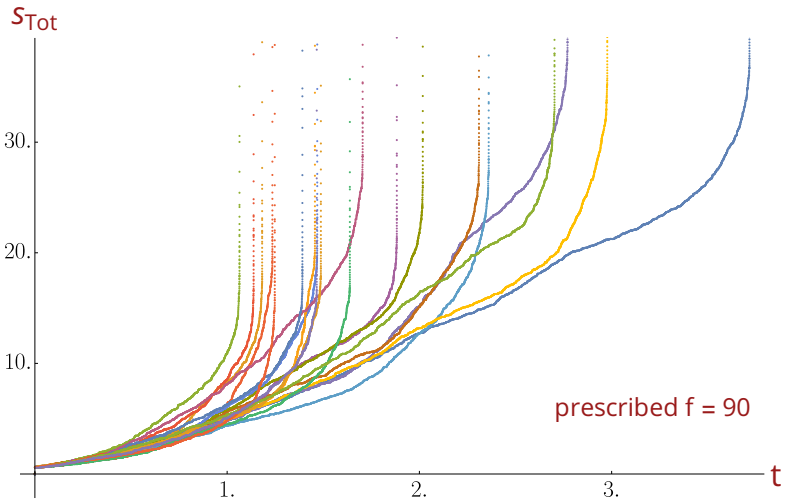

Figure 5.12: Aggregate fibre displacement trajectories s_{tot} for a prescribed load $f = 90$. The upward hook observed on the curves indicates total detachment of one fibre from the other, i.e. 0 attached cross-bridge.

Simulation parameters: $N_{timestep} = 2.10^4$, $k_{on} = 10$, $\kappa = 10$, $\beta = 2$, $d = 1.5$, $c = 1\%$, $N = 200$, $p_{init} = (0.24, 0.76)$, $f = 90$.

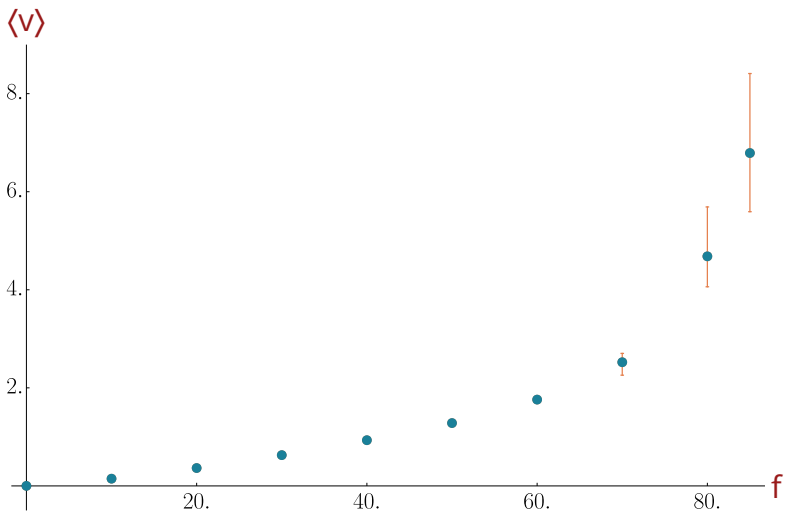

Figure 5.13: Velocity of the system v plotted versus prescribed load f. Bars indicate dispersion of velocity defined as the minimum and the maximum value of the set of $n = 20$ trajectories.

Simulation parameters: $N_{timestep} = 2.10^4 \quad k_{on} = 10 \quad \kappa = 10 \quad \beta = 2 \quad d = 1.5 \quad c = 1\% \quad N = 200 \quad p_{init} = (0.24, 0.76)$

force curve is plotted up to the point where the system experiences total detachment. In this case, the curve is plotted up to $f = 85$ because some of the trajectories at that prescribed loading are complete, whereas at $f = 90$, all of the trajectories exhibit total detachment after a short number of iteration (around 10% of the prescribed $N_{timestep}$). Since the velocity-load curve is the inverse of the load-velocity curve plotted in figure 5.3, one can compare the two by inverting the axes of the velocity-load curve in figure 5.13. Figure 5.14 shows the juxtaposition of the load-velocity curves of both the hard and soft device. One notes the general agreement between the two curves, up to the dispersion

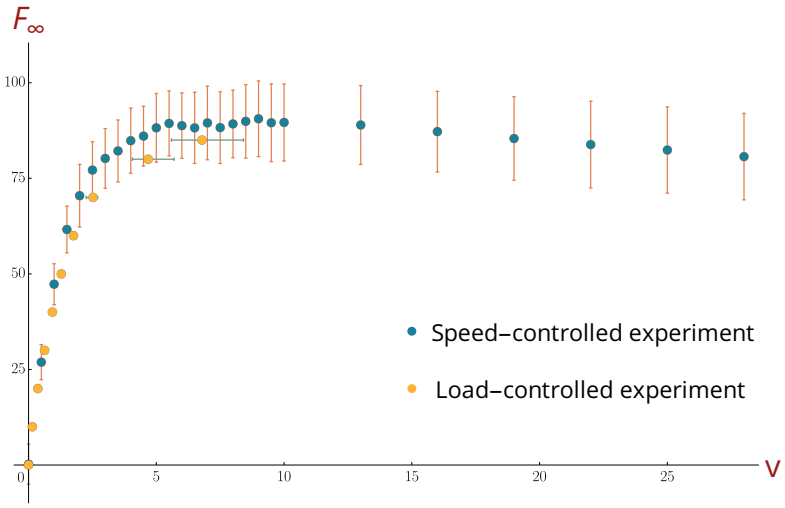

Figure 5.14: Juxtaposition of the load-velocity curve of the system in speed-controlled experiments (in blue, see figure 5.3) and load-controlled experiments (in yellow, see figure 5.13).

caused by the stochastic trajectories. Furthermore, the range of prescribed f that can be plotted without total detachment stops around the maximal load region of the hard device experiment. That is to say, starting from zero-load on the soft device, one can only explore the low velocity branch of the load-velocity curve. As a perspective on future work, one can suggest an experiment where a switch from hard device to soft device

occurs for prescribed $v > 10$, to see whether the branch of higher velocity can be explored by the soft device.

5.2.2 Transient Regime

Regarding the evolution of the soft device, we note that no transient regime is observed, as can be seen in the distribution of s_0 versus time in figure 5.15.

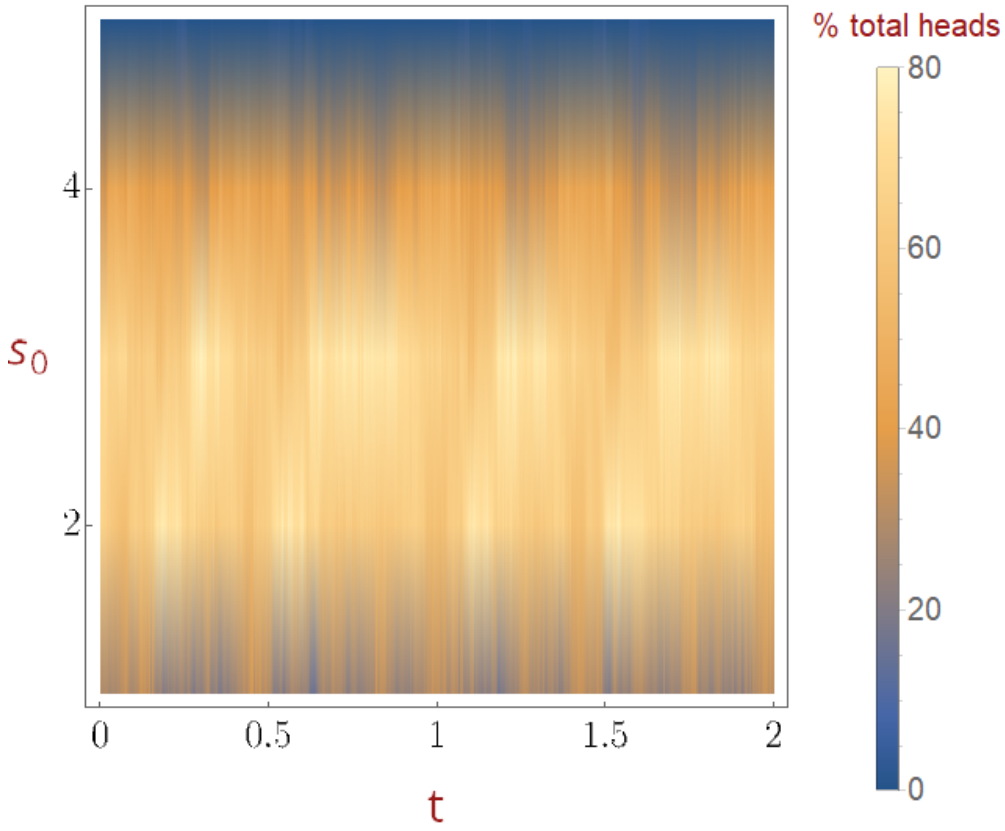
% total heads
80
60
40
20
0
4
2
s_0
0
0.5
1
1.5
2
t

(a) $f = 10$

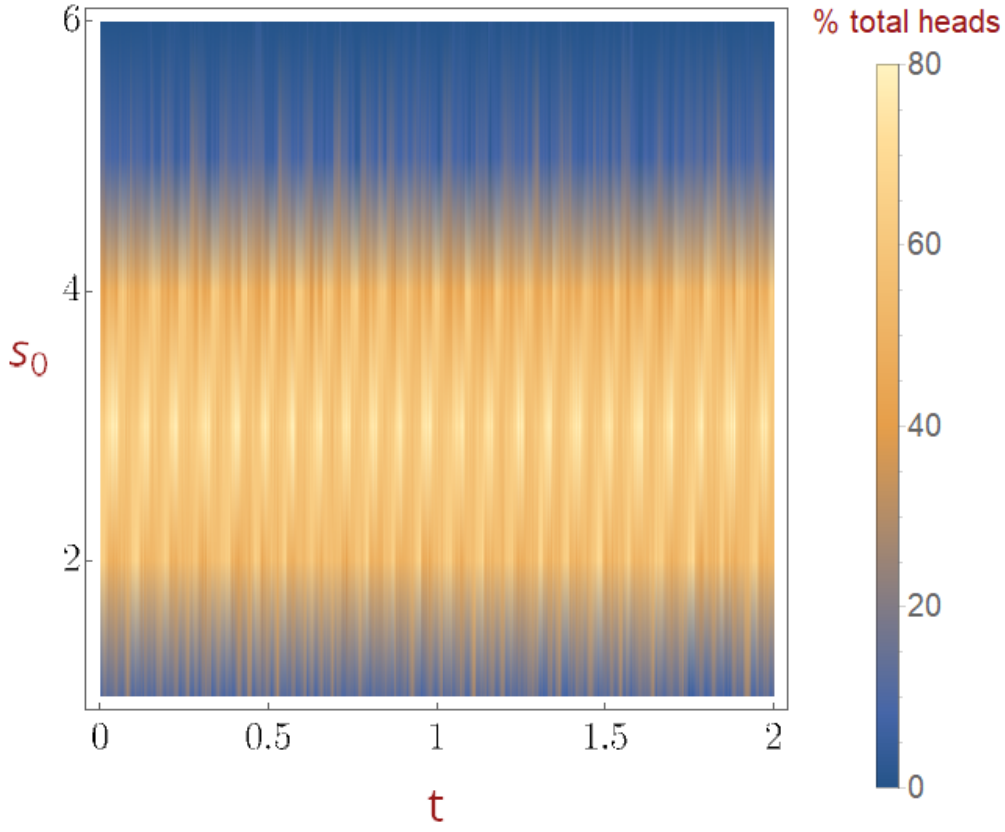
% total heads
80
60
40
20
0
6
4
2
s_0
0
0.5
1
1.5
2
t

(b) $f = 40$

Figure 5.15 shows that for various value of the prescribed load f, the system settles in a steady-state pattern immediately. The steady-state is characterized by a wide spread of s_0 around a stretched value. Strips of convected heads can be seen corresponding to the stretching of a bunch of heads followed by mass detachment to return to the steady-state s_0 distribution. The effect of increased loading f can be seen as increasing the magnitude of the dragging events, so that the distribution of s_0 around the steady-state value widens.

5.3 Effect of Binding Site Spacing

One of the defining feature of our fibre interaction model is the presence of explicit, discrete binding sites. This allows us to investigate the effect of binding site spacing on the mechanics of the system. To this end, we plot the force-velocity curve—F_∞ as a function of v—on the speed driven hard device, for varying values of the intersite spacing d, as shown on figure 5.16.

First we observe that all curves follow the same trend, with a quasi-linear increase in F_∞ at low velocity, a maximum and then a slower decay at high velocities. Next, we observe that the decay of F_∞ at high velocities generally follows a lower curve for higher binding site spacing d. The first effect which explains this trend is what we call a steric effect. Since the experiments are run at a constant amount of cross-bridges N, when the spacing between binding sites d decreases, more binding sites become available for the given amount of cross-bridge heads, as shown on figure 5.17, increasing the binding probability. This results in a linear increase of F_∞ as d decreases which is part of the observed trend on figure 5.16.

The steric effect can be negated by plotting the normalized load multiplied by the periodicity, as done on figure 5.18. Plotting $F_\infty \times d\,(v)$ at low velocities reveals that at the higher end of d, all curves collapse into a single curve, whereas for lower values of d,

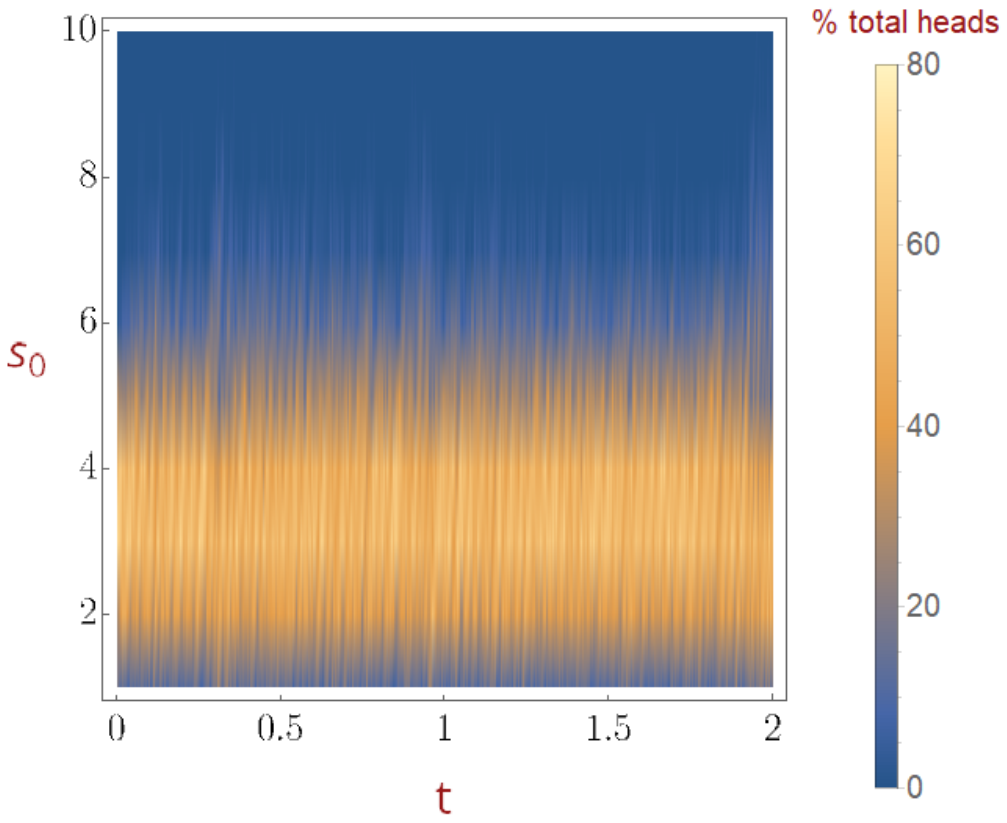

(c) $f = 80$

Figure 5.15: Density plots of the s_0 distribution versus time for different imposed loads f (a): $f = 10$, (b): $f = 40$, (c): $f = 80$.

Simulation parameters: $N_{timestep} = 2.10^4 \quad k_{on} = 10 \quad \kappa = 10 \quad \beta = 2 \quad d = 1.5 \quad c = 1\% \quad N = 200 \quad p_{init} = (0.24, 0.76)$

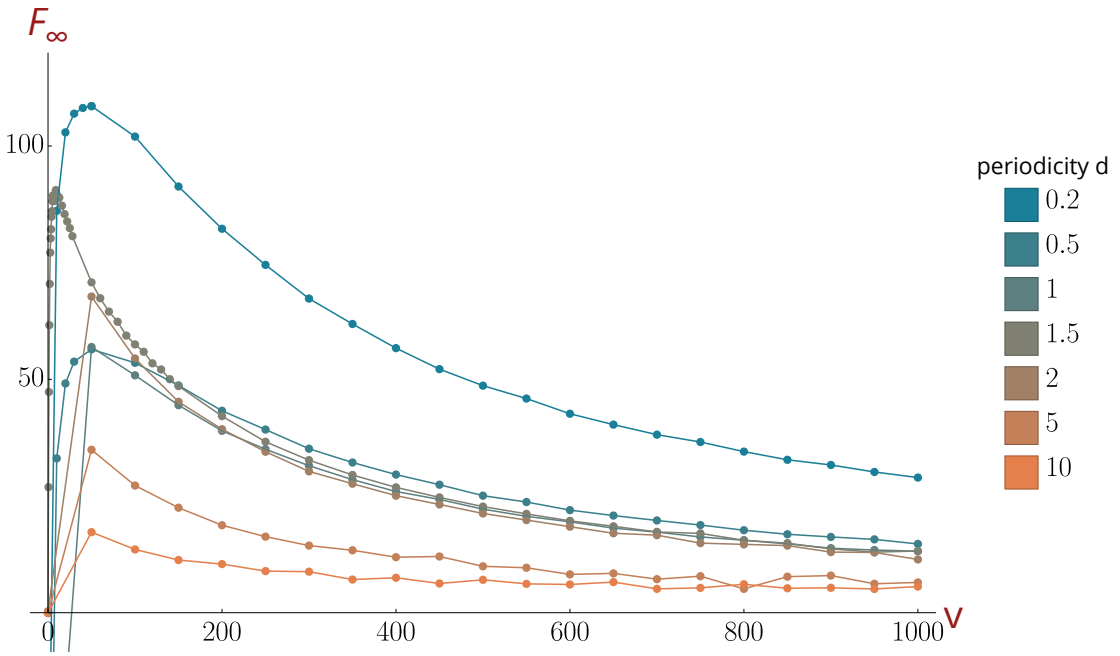

Figure 5.16: F_∞ versus v plotted for varying values of periodicity d.

Simulation parameters: $N_{timestep} = 2.10^4$, $k_{on} = 10$, $\kappa = 10$, $\beta = 2$, $\Delta t = 10^{-4}$, $c = 1\%$, $N = 200$, $p_{init} = (0.24, 0.76)$.

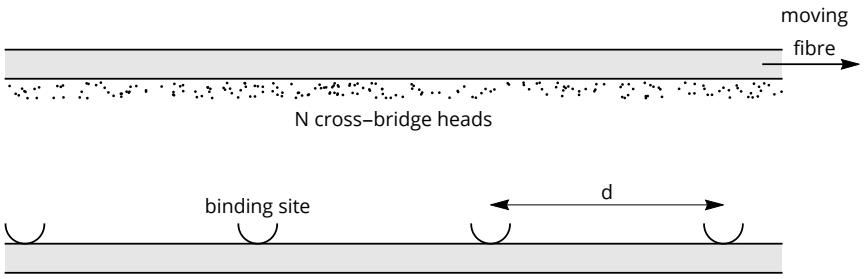

(a) Large d

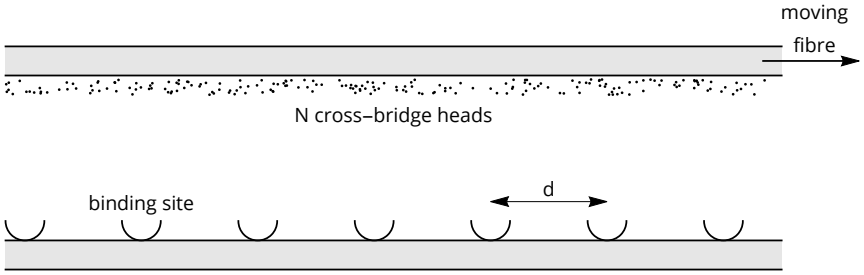

(b) Small d

Figure 5.17: Schematic representation of the periodic fibre system for (a): large and (b): small distance d between binding sites. When the periodicity d decreases, more binding sites per unit length become available, increasing the likelihood of binding and, in turn, the total load F of the system.

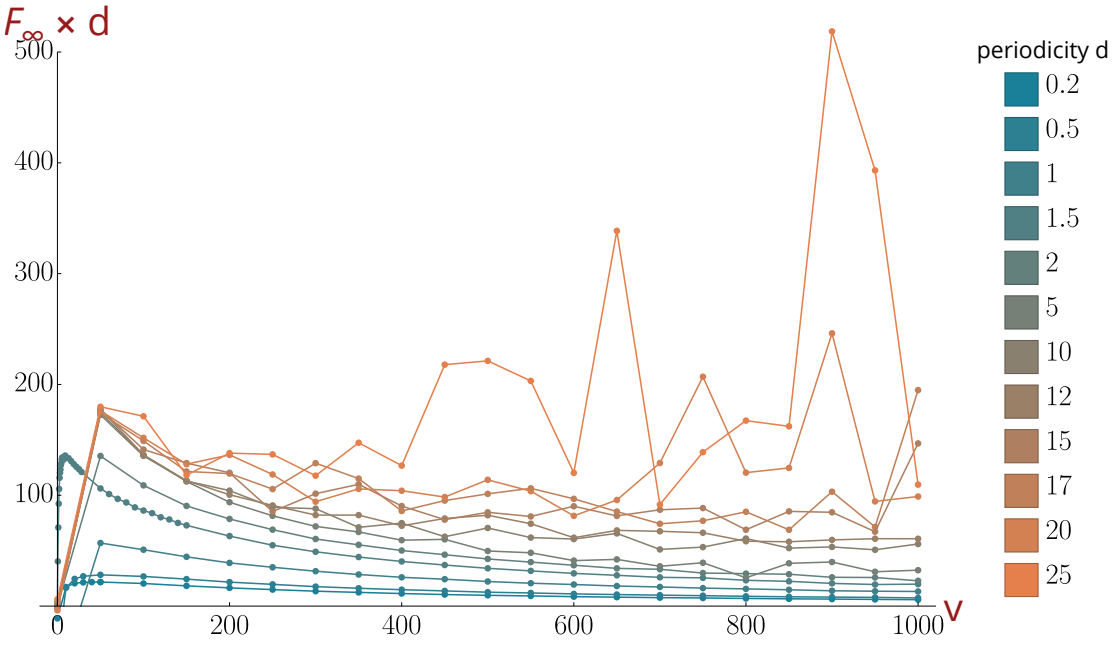

Figure 5.18: Load velocity curves multiplied by the periodicity d. Curves beyond $d = 2$ show a collapse at low velocities.

Simulation parameters: $N_{timestep} = 2.10^4$, $k_{on} = 10$, $\kappa = 10$, $\beta = 2$, $\Delta t = 10^{-4}$, $c = 1\%$, $N = 200$, $p_{init} = (0.24, 0.76)$.

$F_\infty \times d$ increases with d. This is confirmed by plotting $F_\infty \times d$ as a function of d (see figure 5.19). More specifically, for $d \geq 5$ the low-velocity curves collapse irrespective of d,

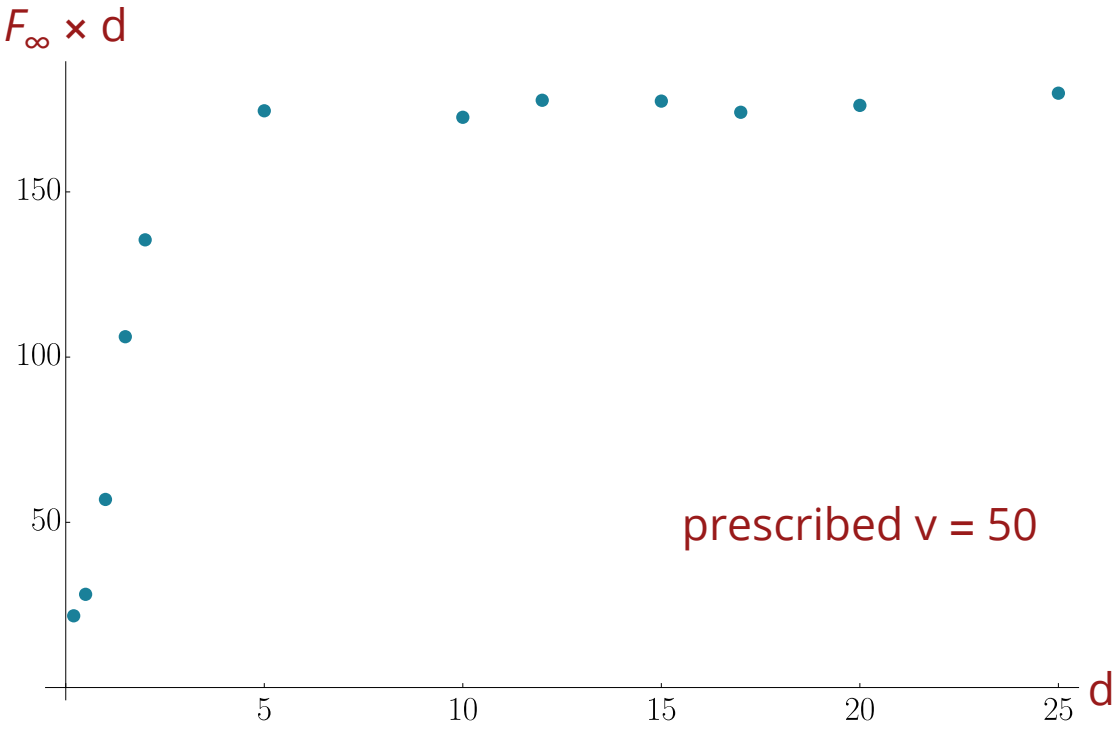

Figure 5.19: $F_\infty \times d$ plotted versus the periodicity d.

Simulation parameters: as in figure 5.18

whereas for $d \leq 2$, $F_\infty \times d$ grows as d increases. Our proposed explanation supposes that for $d \gg 1$, binding sites are sparse, therefore adding a binding site increases the number of attachable heads. We thus have the total load F equal to

$$F = N_b f_{\text{per site}}\,, \tag{5.3}$$

where N_b is the number of binding sites and $f_{\text{per site}}$ is the load per binding site. $f_{\text{per site}}$ doesn't depend on d, meaning that binding sites do not interfere with one another. Next, we also have

$$N_b = \frac{L}{d} \implies L f_{\text{per site}} = dF = constant\,, \tag{5.4}$$

where L is the total length of the fibre. In contrast, when $d \ll 1$, the probability of binding for a head is linked to the number of binding site in its neighbourhood. Therefore d becomes a factor in the curve $F_\infty \times d$.

We suggest that the reason the curve collapse is only observed low velocities is that at high velocities and high d, the fraction of attached heads becomes much lower and when faced with less binding sites this makes the system more susceptible to the noise due to discrete events making the average F_∞ less meaningful.

5.4 Cyclic Solicitation

In this section we describe the behaviour of the fibre system in response to a cyclic solicitation in hard device. Cyclic solicitation is induced by alternating the direction of the traction speed. The number of iterations during which the fibre is moved in a single direction is called the cycling interval and denoted i_{cyc}. From this we can derive the cycling time t_{cyc}, which is the duration spent moving in one direction of the cycle. The t_{cyc} verifies $t_{cyc} = \Delta t \times i_{cyc}$, where Δt is the time step of the simulation. Figure 5.20 showcases a sample trajectory of the system under cyclic movement for a cycling time of $t_{cyc} = 0.1$. Figure 5.21 represents the mean total load $\langle F \rangle$ in the system versus time, averaged over $n = 20$ trajectories, plotted for three values of t_{cyc} ($t_{cyc} = 0.1$, $t_{cyc} = 0.35$ and $t_{cyc} = 0.5$). For $t_{cyc} = 0.1$, the system never leaves the quasi-linear regime and cycles up and down linearly as time progresses. This is as expected, since the cycle duration is shorter than the duration of the transitory regime (see figure 5.2). For $t_{cyc} = 0.5$, the system has time to reach steady-state, and a brief stable period can be observed at the end of each cycle. The intermediate $t_{cyc} = 0.35$ falls between the two previous simulations: the reverse cycles occurs at the cusp between quasi-linear transient state and steady-state. In each case, one observes a higher overshoot that occurs in the first cycle,

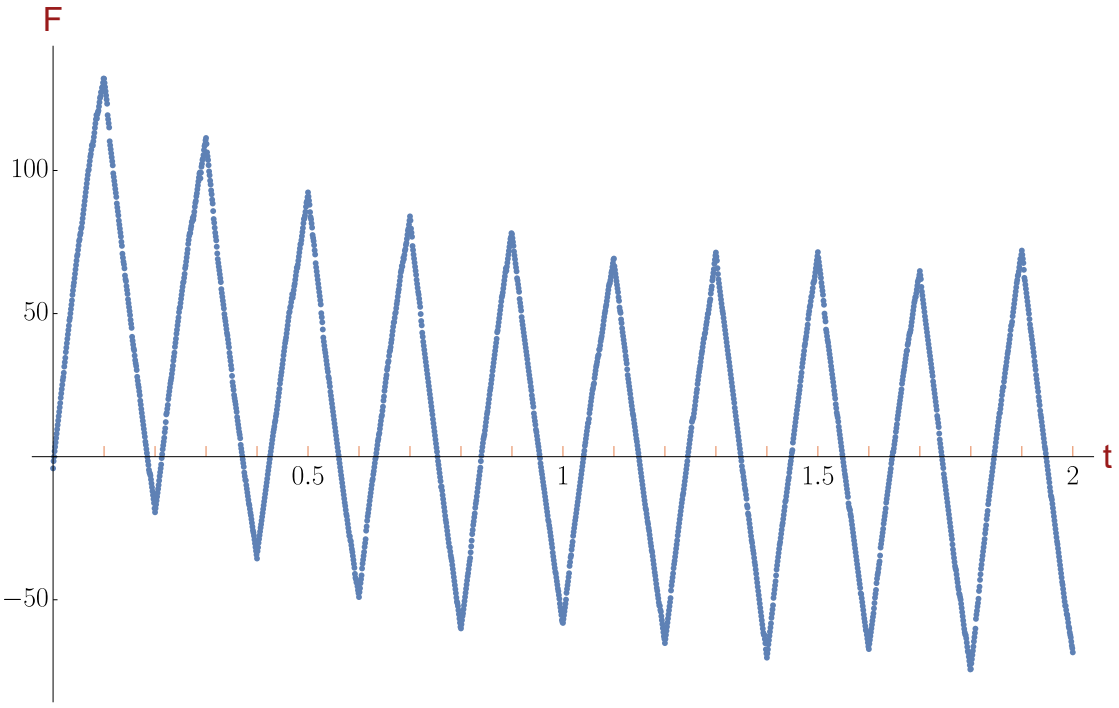

Figure 5.20: Sample trajectory of a cyclic solicitation. Orange ticks indicate the position in time where a reversal of the traction velocity occurs.

Simulation parameters: $N_{timestep} = 2.10^4$, $k_{on} = 10$, $\kappa = 10$, $\beta = 2$, $d = 1.5$, $\Delta t = 10^{-4}$, $c = 1\%$, $N = 200$, $p_{init} = (0.24, 0.76)$, $v = 10$, $i_{cyc} = 1000$ iterations, $t_{cyc} = 0.1$.

which is absent from the subsequent cycles. Furthermore, the cycles eventually move to an average load $\langle F \rangle$ which is symmetrical with respect to the zero-load horizontal axis as shown clearly on figure 5.21a.

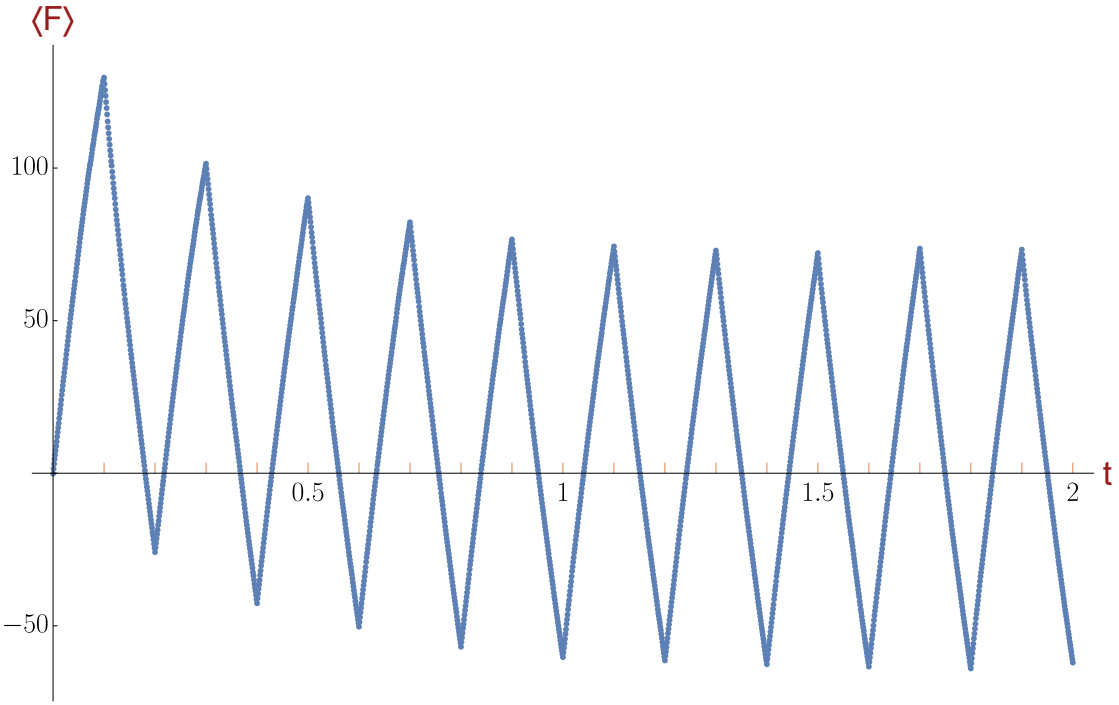

(a) $t_{cyc} = 0.1\,, \quad N_{timestep} = 2.10^4$

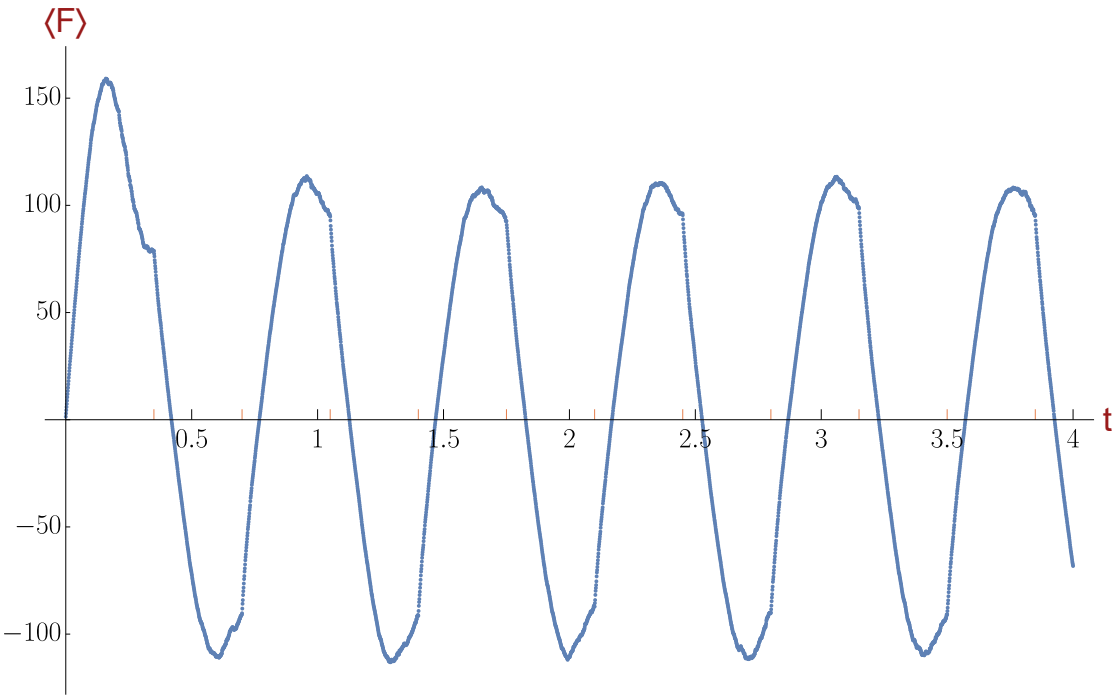

(b) $t_{cyc} = 0.35\,, \quad N_{timestep} = 4.10^4$

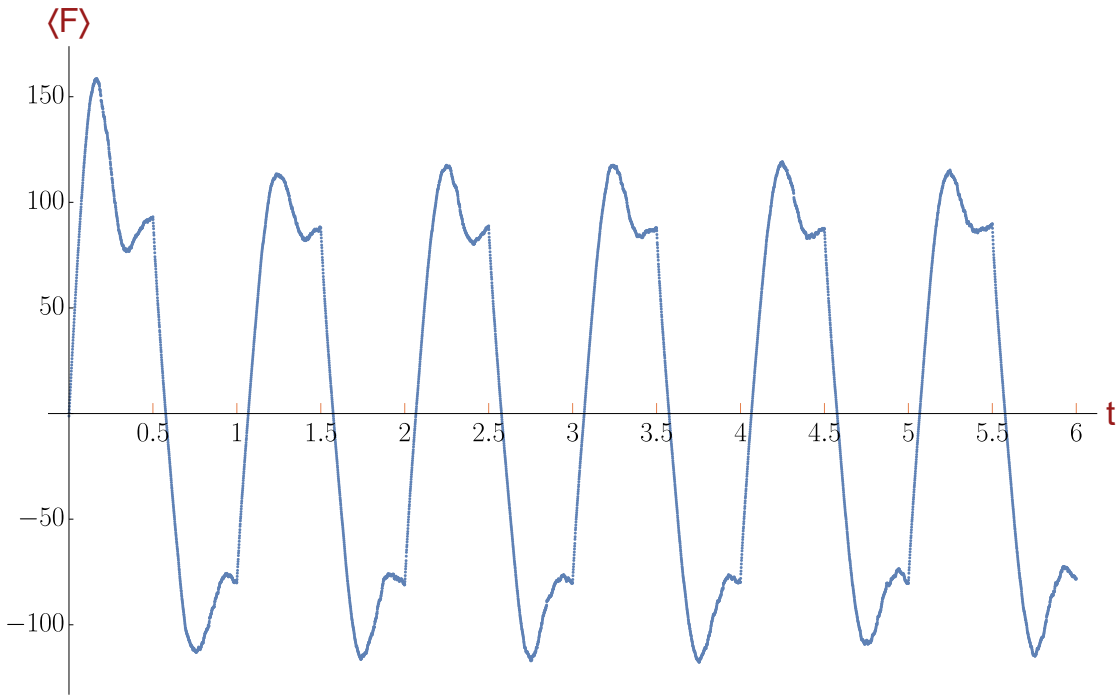

(c) $t_{cyc} = 0.5\,, \quad N_{timestep} = 6.10^4$

Figure 5.21: Averaged total load versus time for a cyclic solicitation of varying cycling time t_{cyc} (a): $t_{cyc} = 0.1$, (b): $t_{cyc} = 0.35$, (c): $t_{cyc} = 0.5$. Orange ticks indicate the position in time where a reversal of the traction velocity occurs. Simulation parameters as in figure 5.20.

This phenomenon can be more clearly observed when plotting the averaged load $\langle F \rangle$ versus the traveled distance l. This manifests itself on figure 5.22 as a convergence towards a limit cycle as the cycling progresses, with an overshoot still visible on the first iteration of the cycle. This progression to a limit cycle reproduces experimental loading assays in collagen-rich tissues such as tendon [17] and skin [105].

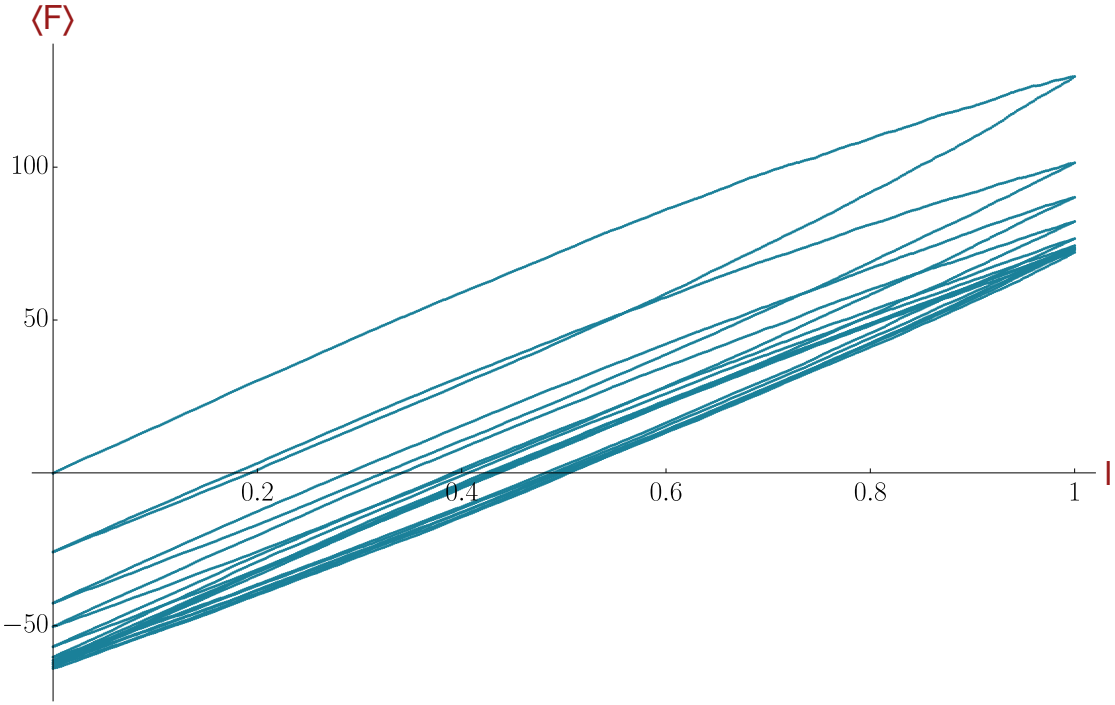

(a) $t_{cyc} = 0.1\,, \quad N_{timestep} = 2.10^4$

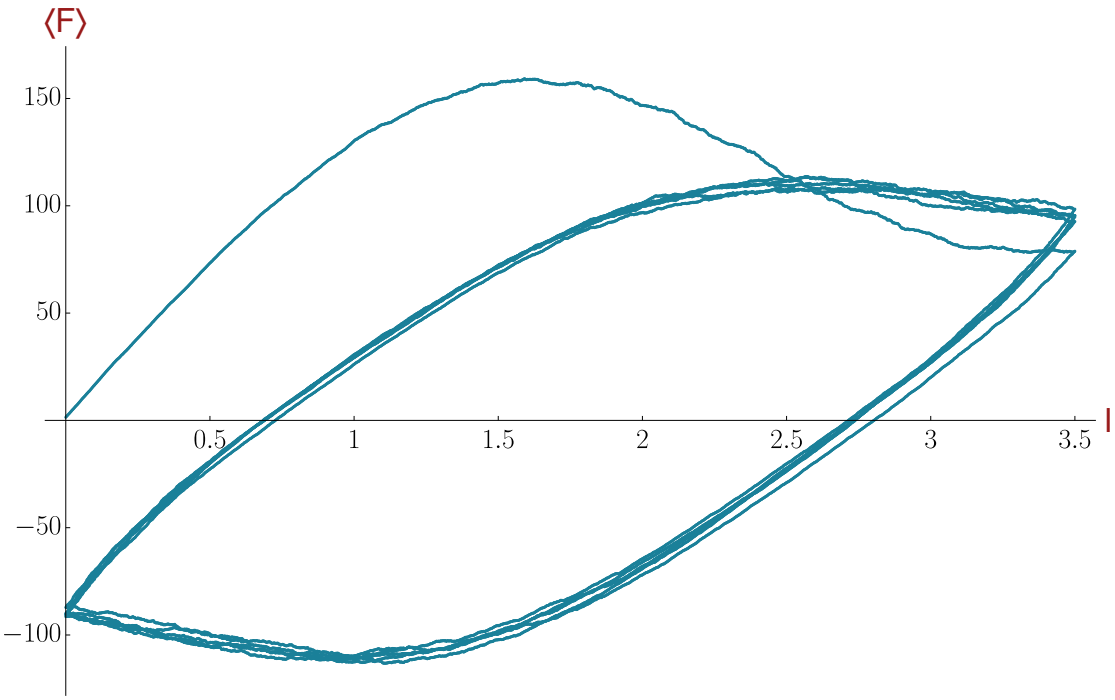

(b) $t_{cyc} = 0.35\,, \quad N_{timestep} = 4.10^4$

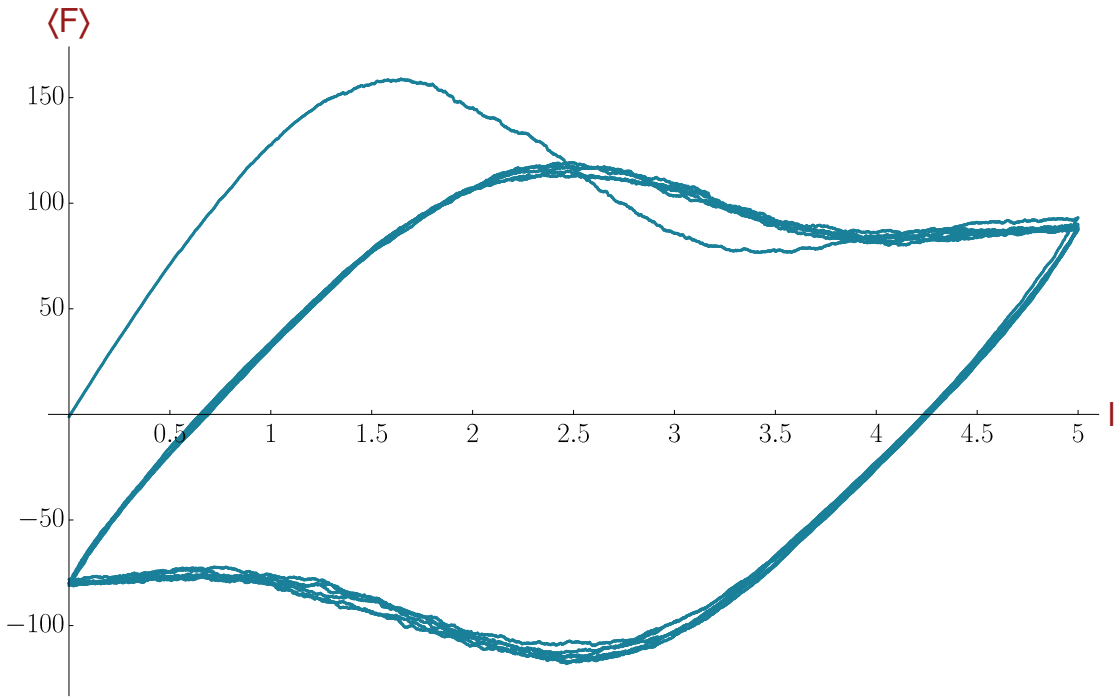

(c) $t_{cyc} = 0.5\,, \quad N_{timestep} = 6.10^4$

Figure 5.22: Averaged load over multiple trajectories $\langle F \rangle$ plotted versus travelled distance l, for different values of t_{cyc}.

Simulation parameters: as in figure 5.20.

6 Results of the Corrected Model

In the previous result and discussion chapter, we used our initial model which doesn't satisfy the detailed balance. As pointed in the presentation of the model, we expected this to be consequenceless as we consider only out-of-equilibrium situations in which the heads are not in front of the attachment site. However, to really make sure that this assumption was true, we redid the key simulations of the manuscript with our corrected model. At the same time, we also increased the stiffness κ to really make sure that the Kramer's detachment rate is a valid assumption.

6.1 Hard Device

First, we redid the simulations in the hard device. The figure 6.1 reproduces the example of a single trajectory (previously figure 4.1), while figure 6.2 gives a collection of different trajectories for our new parameters (previously figure 5.1). Figure 6.3 (previously figure 5.2) gives the behaviour of the total load F averaged over $n = 10$ trajectories. Figure 6.4 (previously figure 5.3) gives the load-velocity curve of the hard device system. Figure 5.4 (previously figure 5.4) gives the evolution of the averaged attached fraction of bonds for increasing values of the prescribed velocity v. Figure 6.6(previously figure 5.6) gives the evolution of the initial slope of the load $\dot{F}$ as a function of the prescribed velocity v.

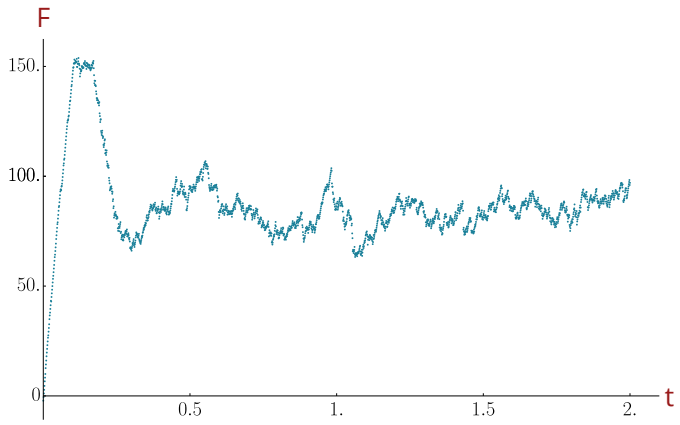

Figure 6.1: Load versus time shown for an example trajectory of the hard device simulation.

Corrected version of figure 4.1.

Simulation parameters: $N_{timestep} = 2.10^4$, $k_{on} = 10$, $\kappa = 100$, $\beta = 2$, $d = 1.5$, $\Delta t = 10^{-4}$, $c = 1\%$, $N = 200$, $p_{init} = (0.18, 0.82)$, $v = 10$.

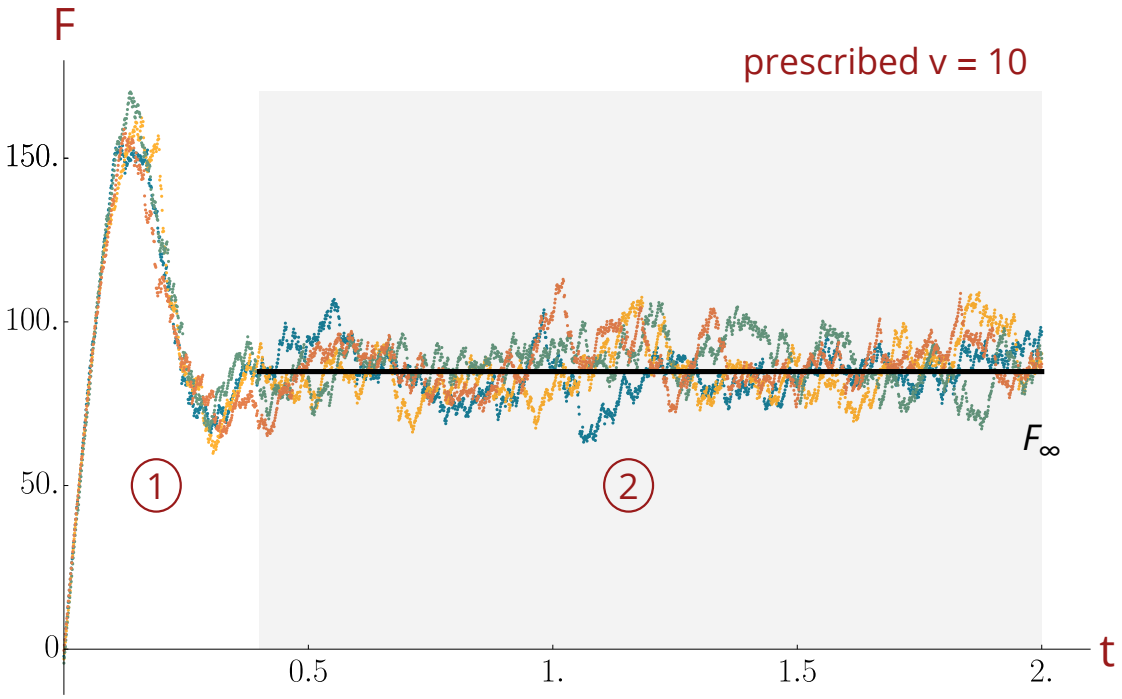

Figure 6.2: Total load in the system F versus time t shown for multiple trajectories and for prescribed velocity $v = 10$. F_∞ visualizes the average value taken by F once the permanent regime has been reached.

① Transient regime. ② Steady-state regime.

Corrected version of figure 5.1.

Simulation parameters: $N_{timestep} = 2.10^4$, $k_{on} = 10$, $\kappa = 100$, $\beta = 2$, $d = 1.5$, $\Delta t = 10^{-4}$, $c = 1\%$, $N = 200$, $p_{init} = (0.18, 0.82)$, $v = 10$.

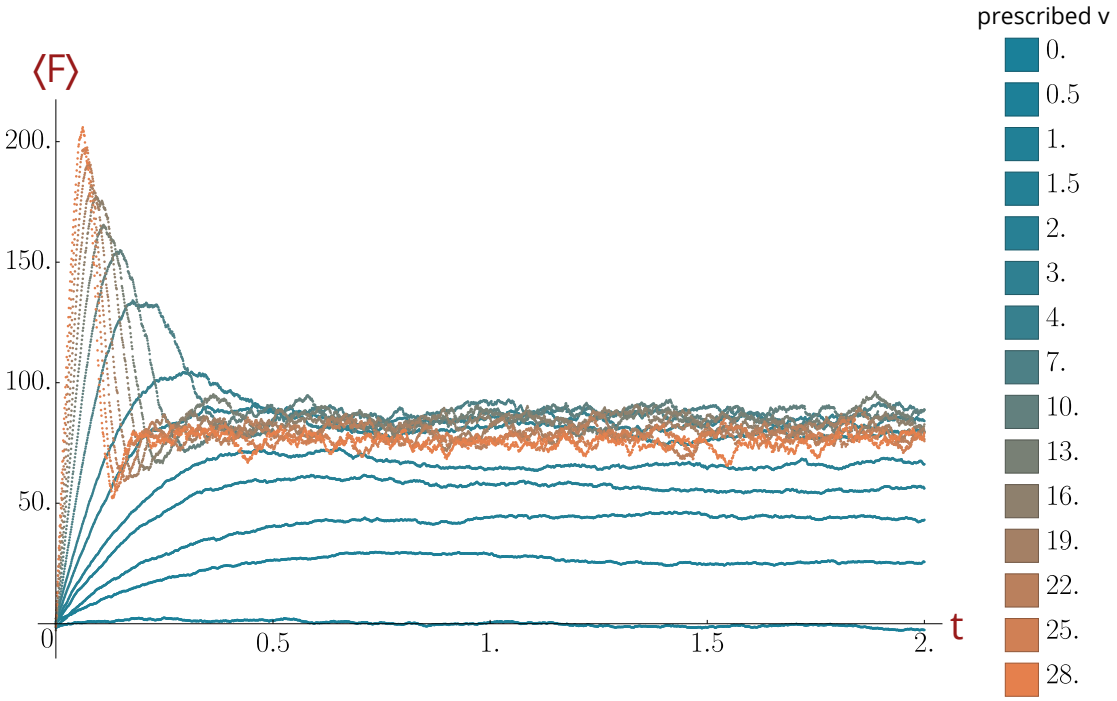

Figure 6.3: Average value $\langle F \rangle (t)$ as a function of time t for increasing sliding velocity v.

Each curve is the average of $n = 10$ simulations.

Corrected version of figure 5.2.

Simulation parameters: $N_{timestep} = 2.10^4$, $k_{on} = 10$, $\kappa = 100$, $\beta = 2$, $d = 1.5$, $\Delta t = 10^{-4}$, $c = 1\%$, $N = 200$, $p_{init} = (0.18, 0.82)$.

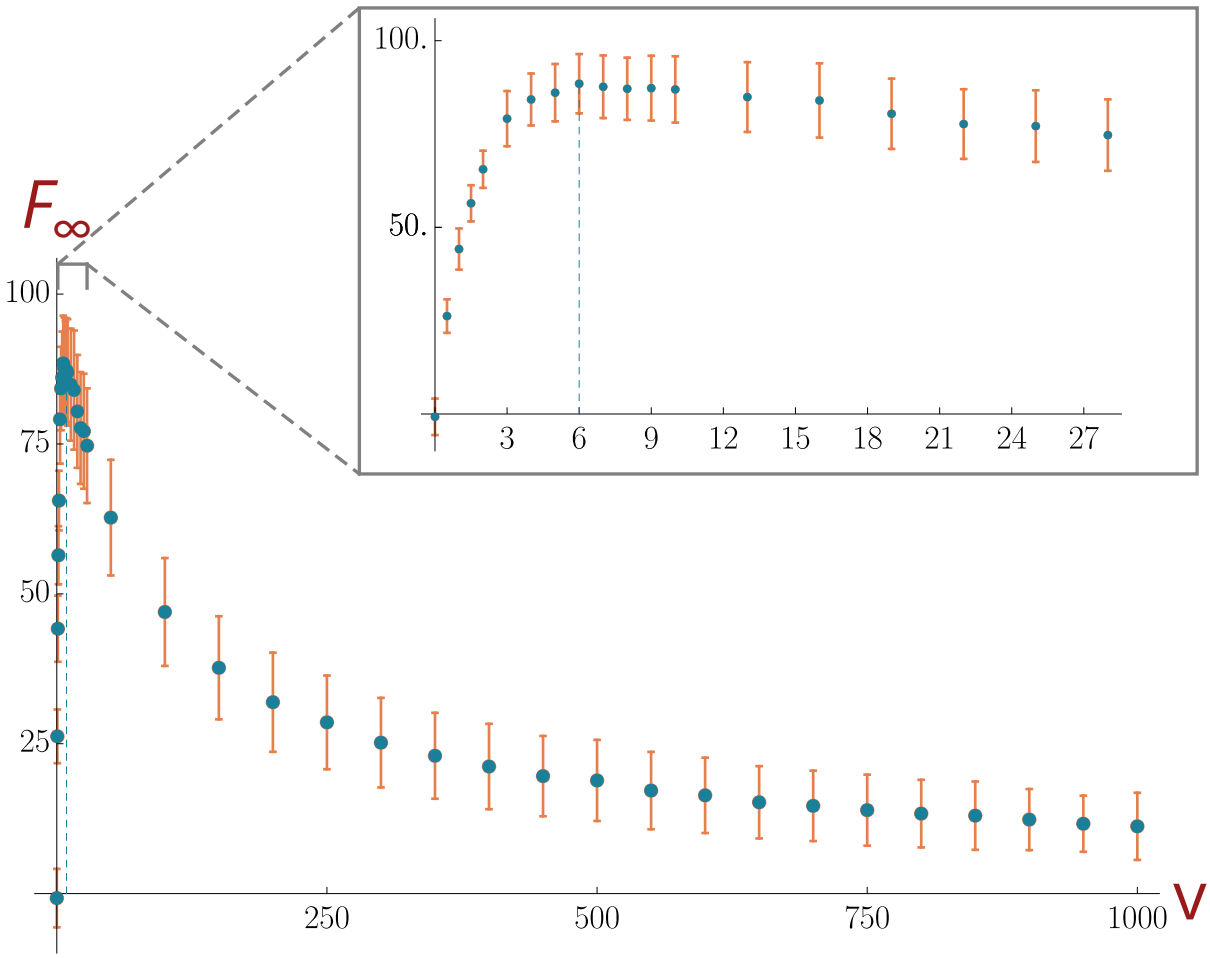

Figure 6.4: Steady-state load F_∞ versus prescribed sliding velocity v. Bars indicate the size of fluctuations at steady-state around the average F_∞ value. These bars are calculated as the standard deviation of F once steady-state has been reached, averaged over all $n = 10$ trajectories of the simulation. Inset shows a zoom around the peak of load-velocity curve. Simulation parameters as in figure 5.2.

Corrected version of figure 5.3.

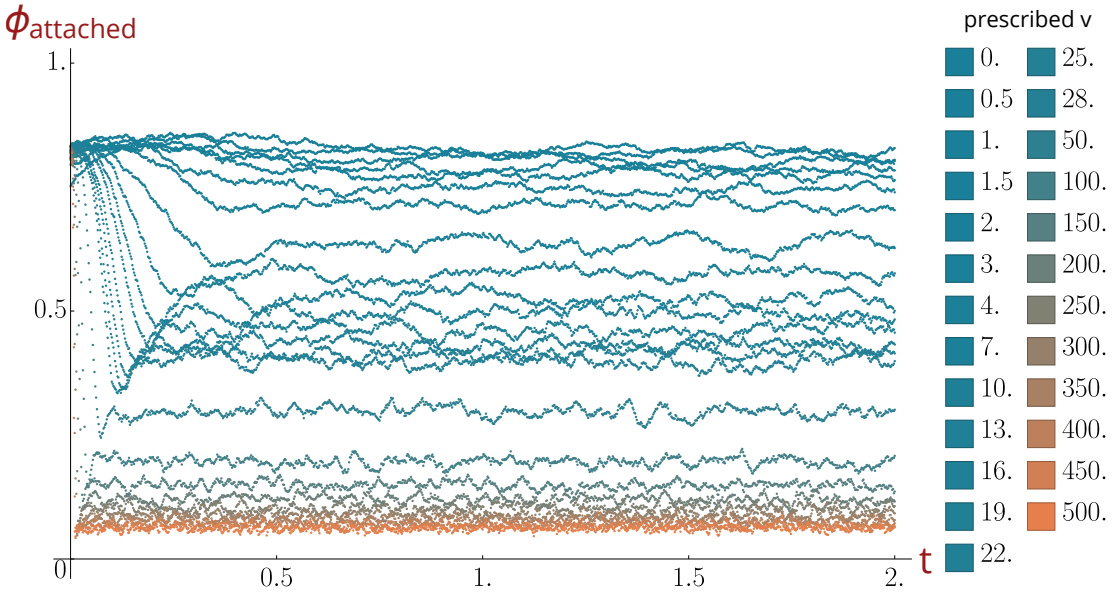

Figure 6.5: Average fraction of attached bonds $\phi_{attached}$ as a function of time, plotted for different values of prescribed v. The initial state has 82% of the bonds attached. Simulation parameters as in figure 6.3

Corrected version of figure 5.4.

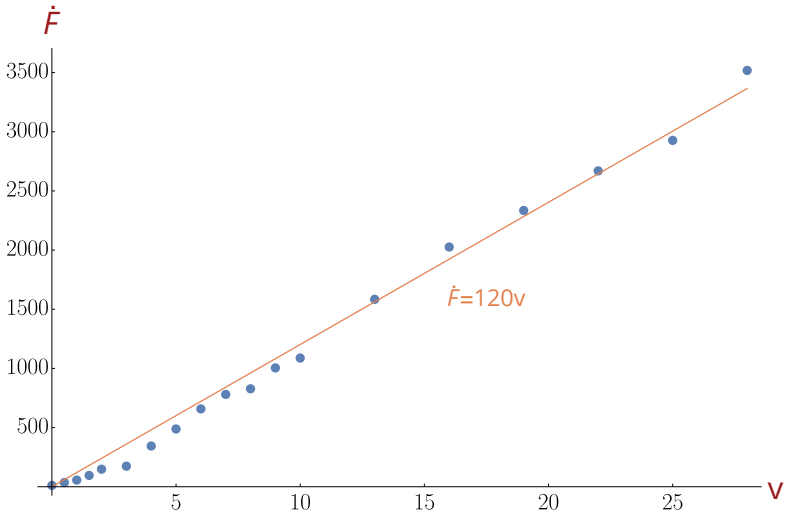

Figure 6.6: Slope $\dot{F}$ of the transient $F(t)$, assuming a linear increase, slope plotted against prescribed sliding velocity v. A linear fit of the data is shown in orange. Simulation parameters as in figure 6.3.

Corrected version of figure 5.6.

6.2 Soft Device

Next we present the results of the corrected model for the soft device. Figure 6.7 (previously figure 4.2) presents a single trajectory of the soft device experiment, while figure 6.8 (previously figure 5.9) presents a collection of multiple trajectories for a prescribed $f = 20$.

Figure 6.9 (previously figure 5.10) presents the aggregate fibre displacement versus time, averaged over $n = 10$ trajectories. Figure 6.10 (previously figure 5.13) gives the velocity-load curve of the soft device system. Figure 6.11 (previously figure 5.14) gives the juxtaposition of the force-velocity curve of both hard and soft device on the same plot.

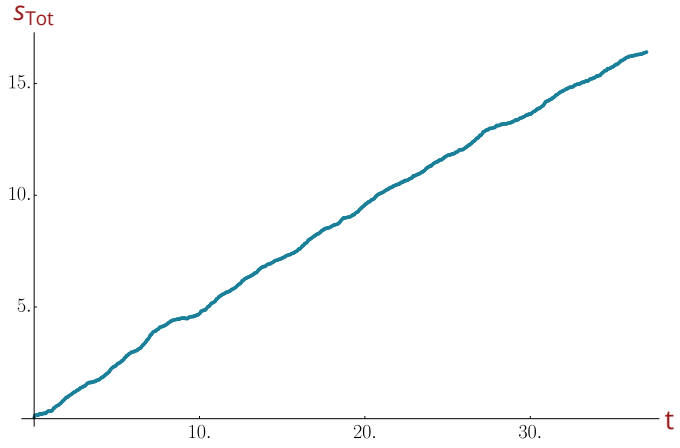

Figure 6.7: Displacement s_{tot} versus time shown for an example trajectory of the hard device simulation.

Corrected version of figure 4.2.

Simulation parameters: $N_{timestep} = 2.10^4$, $k_{on} = 10$, $\kappa = 100$, $\beta = 2$, $d = 1.5$, $c = 1\%$, $N = 200$, $p_{init} = (0.18, 0.82)$, $f = 20$.

6.3 Discussion

As demonstrated by the figures corrected for the detailed balance, the results obtained are very similar to those of the initial model. Qualitative features of the plots are identical and lead to the same conclusions. This outcome confirms our hypothesis that the simulated system operates far from equilibrium such that the breaking of detailed balance does not affect the behaviour of the model significantly. The corrected model has the advantage of being thermodynamically exact. However, unlike the initial model the corrected model may only offers the possibility of attachment at the borders of the binding site. A more advanced model could satisfy both the detailed balance and the possibility for a bond to attach at each point of the binding site. This would require a modification of both k^+ and k^-.

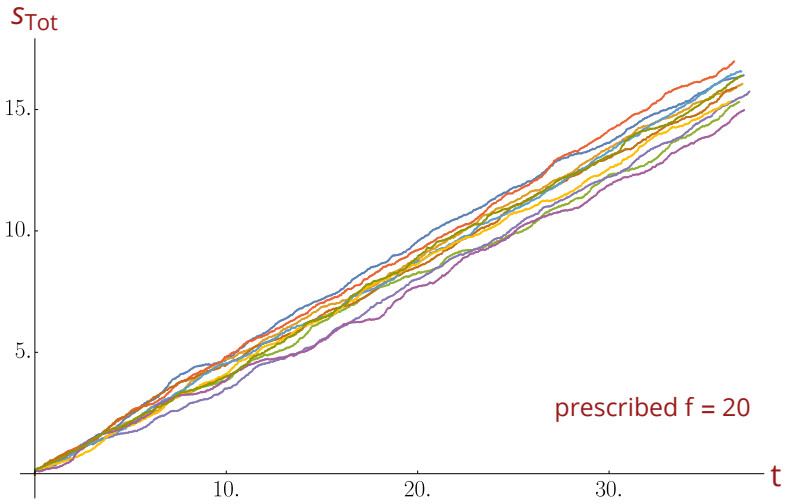

Figure 6.8: Aggregate fibre displacement s_{tot} versus time t shown for multiple trajectories and prescribed load $f = 20$.

Corrected version of figure 5.9.

Simulation parameters: $N_{timestep} = 2.10^4$, $k_{on} = 10$, $\kappa = 100$, $\beta = 2$, $d = 1.5$, $c = 1\%$, $N = 200$, $p_{init} = (0.18, 0.82)$, $f = 20$.

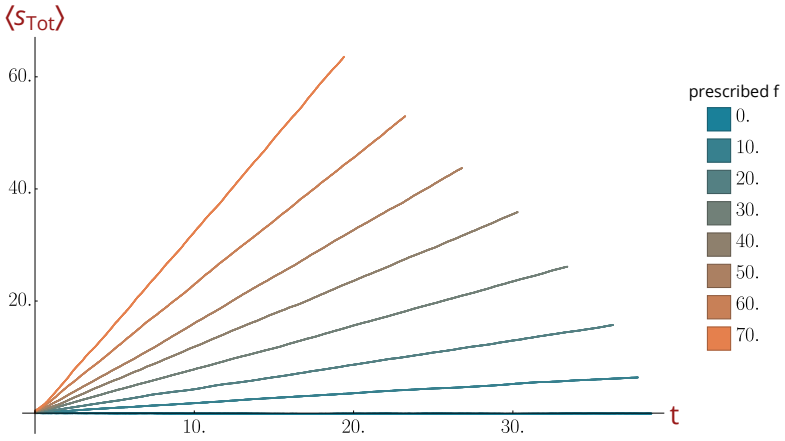

Figure 6.9: Aggregate fibre displacement $\langle s_{tot} \rangle$ averaged over 10 trajectories versus time for different prescribed load f. All displacement are drawn for the same number of iterations.

Corrected version of figure 5.10.

Simulation parameters: $N_{timestep} = 2.10^4$, $k_{on} = 10$, $\kappa = 100$, $\beta = 2$, $d = 1.5$, $c = 1\%$, $N = 200$, $p_{init} = (0.18, 0.82)$, interpolation step: 10^{-2}.

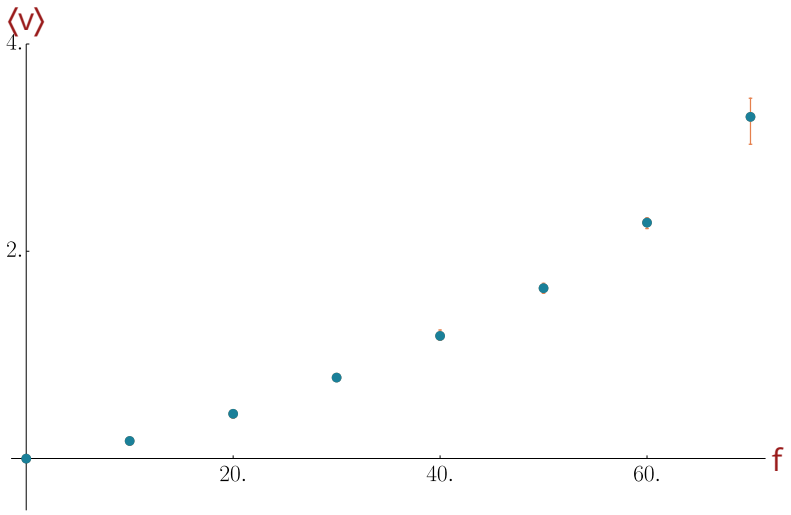

Figure 6.10: Velocity of the system v plotted versus prescribed load f. Bars indicate dispersion of velocity defined as the minimum and the maximum value of the set of $n = 10$ trajectories.

Corrected version of figure 5.13.

Simulation parameters: $N_{timestep} = 2.10^4$ $k_{on} = 10$ $\kappa = 100$ $\beta = 2$ $d = 1.5$ $c = 1\%$ $N = 200$ $p_{init} = (0.18, 0.82)$

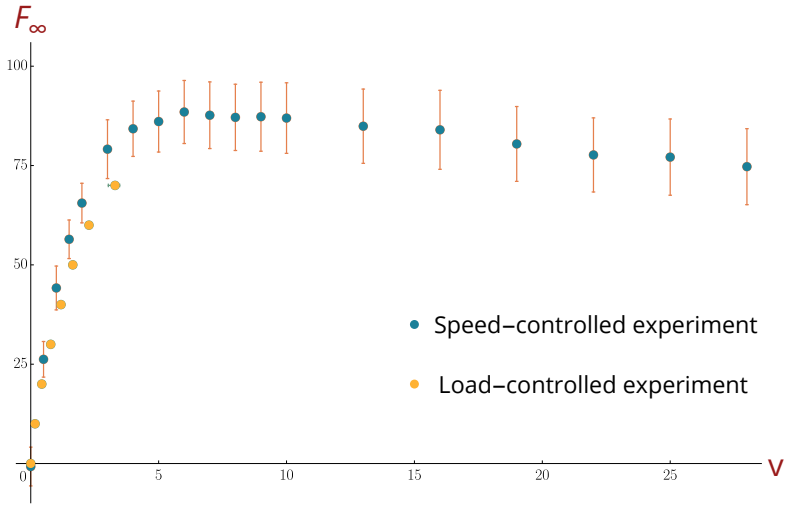

Figure 6.11: Juxtaposition of the load-velocity curve of the system in speed-controlled experiments (in blue, see figure 6.4) and load-controlled experiments (in yellow, see figure 6.10).

Corrected version of figure 5.14.

7 General Conclusion and Perspectives

7.1 General Conclusion

In this manuscript, we devised a mathematical model to describe the mechanical behaviour of fibre networks.

The system described by the model is a generic fibre network represented by rigid fibre elements sliding with respect to one another and interacting via spring-like cross-bridges. We approach this system in a one-dimensional interaction as is suitable for a local description of the network or for a system featuring unidimensional fibre bundles. We are interested specifically in the case where the connecting cross-bridges can attach and detach stochastically to specific binding points along the fibre.

To inform the model, we use reaction rate or Kramers theory [72, 73] to describe rates of attachment and detachment of cross-bridge heads as a function of distance to the closest binding site. Attachment and detachment rates are significant quantities because when multiplied by a time interval, the give probabilities of attachment and detachment which can be used in a stochastic simulation of the fibre system.

All this work is performed for fibres exhibiting a periodic arrangement of binding sites which allow for the mechanical description of a uni-dimensional infinite fibre system.

Next, we give the blueprint to perform simulations of the mechanical model. We examine two loading scenarios: one where the displacement of the fibre is fixed, called a hard device,

the other where the total system load is fixed, called a soft device. For the hard device, a straightforward fixed step algorithm is adopted, for which the system moves only at increments of this time step. In the case of the soft device, since no movement occurs in the system between attachment / detachment events, we implement the Stochastic Simulation Algorithm [100, 101], which skips in time between transition events. Furthermore, we show that these waiting times correspond to that of competing Poisson processes with a parameter equal to the sum of the rates of all competing transition events.

We then examine the results of these simulations under varying loading conditions. Under a hard device, the fibre system gives a load response which resembles a viscoelastic response, with a transient, quasi-linear increase in force which peaks then falls to a steady-state which exhibits large fluctuations around the steady-state value. Sampling the mean steady-state value, that is the F_∞, for a given prescribed velocity allows us to derive the load-velocity curve of the hard device system. The load velocity curve is shown to be non-monotonous, first increasing quasi-linearly with the prescribed velocity and then following a slower decay at high velocities. By examining the attachment state of the system in more detail, we show that this non-monotonicity is the result of two competing effects: the initial increase in load is due to cross-bridges being attached at a higher stretch state, whereas the eventual load decrease is due to the general ripping effect at high speeds, where the total fraction of attached cross-bridges decreases at high velocities.

Next, we investigate the transient state of the simulation. Looking at the distribution of cross-bridge elongation shows that the transient quasi-linear state is the result of ballistic transport of the cross-bridge heads, where the initial uniform distribution of elongation is simply translated in space towards higher elongation. The end of the transient state and the onset of steady-state is marked by the detachment and reattachment of a significant number of cross-bridge heads at smaller elongations.

Meanwhile, the soft device simulation shows a quasi-linear ramp response to prescribed load without any transient regime. The total displacement s_{tot} can be linearly fitted to provide a movement velocity in response to the prescribed load. This allows us to chart a velocity-load curve that is analogous to the one in the hard device. The velocity-load curve shows monotonously increasing velocity as prescribed loading grows, up until the point where total detachment of the two fibres start occurring during the simulation. The total detachment at high velocities means that only the low speed branch of the load-velocity curve can be explored by the soft device. Our results show that the low velocity branch of the soft device velocity-load curve is consistent with the one of the load-velocity curve of the hard device.

Next, we examine the effect of binding site spacing on the behaviour of the system. Our results show that generally, the load-velocity curve values increases when the periodicity d decreases. Part of this increase is due to a steric effect, which indiscriminately increases the load F when d decreases. When we eliminate the steric effect however, we see that all curves above a threshold value of d collapse into a single master curve and for d under the threshold value, we see a general increase in the load-velocity curve when d decreases. We interpret this as the influence of the number of relevant binding site neighbours. For d above the threshold value, the number of relevant neighbours is 0, so all force-velocity curve behave the same way, irrespective of d. For d below the threshold value, decreasing d brings more relevant binding site per unit length and more attachment probability, thus increasing the value of the load-velocity curve.

Finally, the system is loaded cyclically in the hard device configuration, where the sliding velocity is flipped periodically. All cycling configurations exhibit an evolution toward a limit cycle, which is established gradually when the cycling occurs rapidly and immediately when the cycling is slower.

7.2 Perspectives

In this section, we suggest a few directions which future work can take to expand upon the work presented herein.

First, further parametric study of the system can be performed. In particular the parametric study can be adapted to a biological system of interest such as the tendon at the tissue level or actin bundles at the microscopic level. This adaptation can be done by adjusting the values of parameters such as cross-link stiffness or binding site spacing to realistic values for the corresponding biological system.

Next, the hard device system can be used to explore the high velocity branch of the velocity-load curve. One would start the experiment in hard device at high sliding velocities and change the experiment control to a soft device mode. This would allow us to check whether a branching or an instability of the velocity-load curve can occur at high velocities.

In the case of cyclic solicitation, we suggest the following additional experiments. First, taking fibre buckling into account by stopping fibre movement in soft device when the experienced load f becomes negative. Second, a study of cycle reversibility can be performed to check whether the system moves away from the limit cycle once reached or not.

The final long-term goal of our work would be the construction of a fibre-level behaviour law which would then be used to simulate an ensemble of connected fibres.

Bibliography

[1] Peter Fratzl and Richard Weinkamer. "Nature's hierarchical materials". In: *Progress in Materials Science* 52.8 (2007), pp. 1263–1334. DOI: 10.1016/j.pmatsci.2007.06.001. arXiv: 34548501731.

[2] Peter Fratzl. "Cellulose and collagen: from fibres to tissues". In: *Current Opinion in Colloid and Interface Science* 8.1 (Mar. 2003), pp. 32–39. DOI: 10.1016/S1359-0294(03)00011-6.

[3] Dietrich Fengel and Gerd Wegener. *Wood: chemistry, ultrastructure, reactions.* 2011.

[4] Tomomi Saito, Itaru Uchida, and Masatsune Takeda. "Skeletal growth of the deep-sea hexactinellid sponge Euplectella oweni, and host selection by the symbiotic shrimp Spongicola japonica (Crustacea: Decapoda: Spongicolidae)". In: *Journal of Zoology* 258.4 (2002), pp. 521–529. DOI: 10.1017/S0952836902001681.

[5] C. Levi et al. "A remarkably strong natural glassy rod: the anchoring spicule of theMonorhaphis sponge". In: *Journal of Materials Science Letters* 8.3 (Mar. 1989), pp. 337–339. DOI: 10.1007/BF00725516.

[6] S. Weiner and H. D. Wagner. "THE MATERIAL BONE: Structure-Mechanical Function Relations". In: *Annual Review of Materials Science* 28.1 (Aug. 1998), pp. 271–298. DOI: 10.1146/annurev.matsci.28.1.271.

[7] Jae-Young Rho, Liisa Kuhn-Spearing, and Peter Zioupos. “Mechanical properties and the hierarchical structure of bone”. In: *Medical Engineering and Physics* 20.2 (Mar. 1998), pp. 92–102. DOI: 10.1016/S1350-4533(98)00007-1.

[8] P. Fratzl et al. “Structure and mechanical quality of the collagen–mineral nano-composite in bone”. In: *J. Mater. Chem.* 14.14 (2004), pp. 2115–2123. DOI: 10.1039/B402005G.

[9] Karen J. Hodgens et al. “Structural relations between collagen and mineral in bone as determined by high voltage electron microscopic tomography”. In: *Microscopy Research and Technique* 33.2 (2002), pp. 192–202. DOI: 10.1002/(sici)1097-0029(19960201)33:2<192::aid-jemt9>3.3.co;2-t.

[10] William J. Landis. “A study of calcification in the leg tendons from the domestic Turkey”. In: *Journal of Ultrastructure and Molecular Structure Research* 94.3 (Mar. 1986), pp. 217–238. DOI: 10.1016/0889-1605(86)90069-8.

[11] William J Landis and Frederick H Silver. “The structure and function of normally mineralizing avian tendons”. In: *Comparative Biochemistry and Physiology Part A: Molecular and Integrative Physiology* 133.4 (Dec. 2002), pp. 1135–1157. DOI: 10.1016/S1095-6433(02)00248-9.

[12] P. Fratzl et al. “Mineralized Microstructure of Calcified Avian Tendons: A Scanning Small Angle X-ray Scattering Study”. In: *Calcified Tissue International* 72.5 (May 2003), pp. 567–576. DOI: 10.1007/s00223-002-1031-8.

[13] Peter Fratzl et al. “Fibrillar Structure and Mechanical Properties of Collagen”. In: 122 (1997), pp. 119–122. DOI: 10.1006/jsbi.1998.3966.

[14] R.M. Alexander. “Energy-saving mechanisms in walking and running”. In: *Journal of Experimental Biology* 160.1 (1991), pp. 55–69.

[15] Chavaunne T. Thorpe et al. “The interfascicular matrix enables fascicle sliding and recovery in tendon, and behaves more elastically in energy storing tendons”. In: *Journal of the Mechanical Behavior of Biomedical Materials* 52 (Dec. 2015), pp. 85–94. DOI: 10.1016/J.JMBBM.2015.04.009.

[16] R. Puxkandl et al. “Viscoelastic properties of collagen: Synchrotron radiation investigations and structural model”. In: *Philosophical Transactions of the Royal Society B: Biological Sciences* 357.1418 (2002), pp. 191–197. DOI: 10.1098/rstb.2001.1033.

[17] Y. Goulam Houssen et al. “Monitoring micrometer-scale collagen organization in rat-tail tendon upon mechanical strain using second harmonic microscopy”. In: *Journal of Biomechanics* 44.11 (July 2011), pp. 2047–2052. DOI: 10.1016/j.jbiomech.2011.05.009.

[18] Einat Raz and Yoram Lanir. “Recruitment Viscoelasticity of the Tendon”. In: *Journal of Biomechanical Engineering* 131.11 (Oct. 2009), p. 111008. DOI: 10.1115/1.3212107.

[19] Stéphane Bancelin et al. “Ex vivo multiscale quantitation of skin biomechanics in wild-type and genetically-modified mice using multiphoton microscopy”. In: *Scientific Reports* 5.November (2015), p. 17635. DOI: 10.1038/srep17635.

[20] Stéphane Bancelin. “Imagerie Quantitative du Collagène par Génération de Seconde Harmonique”. PhD thesis. Ecole Polytechnique, 2013, p. 223.

[21] Arnab Bhattacharjee and Manju Bansal. “Collagen Structure: The Madras Triple Helix and the Current Scenario”. In: *IUBMB Life (International Union of Biochemistry and Molecular Biology: Life)* 57.3 (Mar. 2005), pp. 161–172. DOI: 10.1080/15216540500090710.

[22] Laurent Bozec and Michael Horton. "Topography and Mechanical Properties of Single Molecules of Type I Collagen Using Atomic Force Microscopy". In: *Biophysical Journal* 88.6 (June 2005), pp. 4223–4231. DOI: 10.1529/biophysj.104.055228.

[23] D.J. Hulmes et al. "Radial packing, order, and disorder in collagen fibrils". In: *Biophysical Journal* 68.5 (May 1995), pp. 1661–1670. DOI: 10.1016/S0006-3495(95)80391-7.

[24] Naoki Sasaki and Shingo Odajima. "Elongation mechanism of collagen fibrils and force-strain relations of tendon at each level of structural hierarchy". In: *Journal of Biomechanics* 29.9 (Sept. 1996), pp. 1131–1136. DOI: 10.1016/0021-9290(96)00024-3.

[25] Yu-Long Sun et al. "Stretching type II collagen with optical tweezers". In: *Journal of Biomechanics* 37.11 (Nov. 2004), pp. 1665–1669. DOI: 10.1016/j.jbiomech.2004.02.028.

[26] Markus J. Buehler. "Atomistic and continuum modeling of mechanical properties of collagen: Elasticity, fracture, and self-assembly". In: *Journal of Materials Research* 21.8 (Aug. 2006), pp. 1947–1961. DOI: 10.1557/jmr.2006.0236.

[27] M. J. Buehler. "Nature designs tough collagen: Explaining the nanostructure of collagen fibrils". In: *Proceedings of the National Academy of Sciences* 103.33 (Aug. 2006), pp. 12285–12290. DOI: 10.1073/pnas.0603216103.

[28] Markus J. Buehler. "Nanomechanics of collagen fibrils under varying cross-link densities: Atomistic and continuum studies". In: *Journal of the Mechanical Behavior of Biomedical Materials* 1.1 (Jan. 2008), pp. 59–67. DOI: 10.1016/j.jmbbm.2007.04.001.

[29] Bruce Alberts et al. *Molecular Biology of the Cell*. sixth edit. Garland Science, 2015.

[30] Jonathon Howard. *Mechanics of Motor Proteins and the Cytoskeleton*. Sinauer Associates, 2001, p. 367.

[31] Thomas D. Pollard and Robert D. Goldman. *The Cytoskeleton*. 2017, p. 391.

[32] S. Heins et al. "The rod domain of NF-L determines neurofilament architecture, whereas the end domains specify filament assembly and network formation". In: *The Journal of Cell Biology* 123.6 (Dec. 1993), pp. 1517–1533. DOI: 10.1083/jcb.123.6.1517.

[33] Melanie Hohenadl et al. "Desmin Filaments Studied by Quasi-Elastic Light Scattering". In: *Biophysical Journal* 77.4 (Oct. 1999), pp. 2199–2209. DOI: 10.1016/S0006-3495(99)77060-8.

[34] Masaki Inagaki et al. "Regulation of assembly-disassembly of intermediate filaments in vitro." In: *Cell Structure and Function* 14.3 (1989), pp. 279–286. DOI: 10.1247/csf.14.279.

[35] R. D. Fraser and T. P. MacRae. "Molecular structure and mechanical properties of keratins". In: *Symposia of the Society for Experimental Biology* (1980).

[36] Julien Berro et al. "Attachment Conditions Control Actin Filament Buckling and the Production of Forces". In: *Biophysical Journal* 92.7 (Apr. 2007), pp. 2546–2558. DOI: 10.1529/biophysj.106.094672.

[37] Markus Harasim et al. "Direct Observation of the Dynamics of Semiflexible Polymers in Shear Flow". In: *Physical Review Letters* 110.10 (Mar. 2013), p. 108302. DOI: 10.1103/PhysRevLett.110.108302.

[38] Laurent Blanchoin et al. “Actin Dynamics, Architecture, and Mechanics in Cell Motility”. In: *Physiological Reviews* 94.1 (Jan. 2014), pp. 235–263. DOI: 10.1152/physrev.00018.2013.

[39] Vérane Achard et al. “A “Primer”-Based Mechanism Underlies Branched Actin Filament Network Formation and Motility”. In: *Current Biology* 20.5 (Mar. 2010), pp. 423–428. DOI: 10.1016/j.cub.2009.12.056.

[40] Orkun Akin and R. Dyche Mullins. “Capping Protein Increases the Rate of Actin-Based Motility by Promoting Filament Nucleation by the Arp2/3 Complex”. In: *Cell* 133.5 (May 2008), pp. 841–851. DOI: 10.1016/j.cell.2008.04.011.

[41] Mark J. Dayel et al. “In Silico Reconstitution of Actin-Based Symmetry Breaking and Motility”. In: *PLoS Biology* 7.9 (Sept. 2009). Ed. by Thomas Pollard, e1000201. DOI: 10.1371/journal.pbio.1000201.

[42] A. Kawska et al. “How actin network dynamics control the onset of actin-based motility”. In: *Proceedings of the National Academy of Sciences* 109.36 (Sept. 2012), pp. 14440–14445. DOI: 10.1073/pnas.1117096109.

[43] Danijela Vignjevic, John Peloquin, and Gary G. Borisy. “In Vitro Assembly of Filopodia-Like Bundles”. In: 2006, pp. 727–739. DOI: 10.1016/S0076-6879(06)06057-5.

[44] Danijela Vignjevic et al. “Formation of filopodia-like bundles in vitro from a dendritic network”. In: *The Journal of Cell Biology* 160.6 (Mar. 2003), pp. 951–962. DOI: 10.1083/jcb.200208059.

[45] Ekta Seth Chhabra and Henry N. Higgs. “The many faces of actin: matching assembly factors with cellular structures”. In: *Nature Cell Biology* 9.10 (Oct. 2007), pp. 1110–1121. DOI: 10.1038/ncb1007-1110.

[46] Daniel A. Fletcher and R. Dyche Mullins. “Cell mechanics and the cytoskeleton”. In: *Nature* 463.7280 (Jan. 2010), pp. 485–492. DOI: 10.1038/nature08908.

[47] Margaret L. Gardel et al. “Chapter 19 Mechanical Response of Cytoskeletal Networks”. In: 2008, pp. 487–519. DOI: 10.1016/S0091-679X(08)00619-5.

[48] Simone Köhler, Volker Schaller, and Andreas R. Bausch. “Collective Dynamics of Active Cytoskeletal Networks”. In: *PLoS ONE* 6.8 (Aug. 2011). Ed. by Daniel J. Muller, e23798. DOI: 10.1371/journal.pone.0023798.

[49] Céline Revenu et al. “The co-workers of actin filaments: from cell structures to signals”. In: *Nature Reviews Molecular Cell Biology* 5.8 (Aug. 2004), pp. 635–646. DOI: 10.1038/nrm1437.

[50] B. Wagner et al. “Cytoskeletal polymer networks: The molecular structure of cross-linkers determines macroscopic properties”. In: *Proceedings of the National Academy of Sciences* 103.38 (Sept. 2006), pp. 13974–13978. DOI: 10.1073/pnas.0510190103.

[51] David S. Courson and Ronald S. Rock. “Actin Cross-link Assembly and Disassembly Mechanics for α-Actinin and Fascin”. In: *Journal of Biological Chemistry* 285.34 (Aug. 2010), pp. 26350–26357. DOI: 10.1074/jbc.M110.123117.

[52] K.E. Kasza et al. “Actin Filament Length Tunes Elasticity of Flexibly Cross-Linked Actin Networks”. In: *Biophysical Journal* 99.4 (Aug. 2010), pp. 1091–1100. DOI: 10.1016/j.bpj.2010.06.025.

[53] R. K. Meyer. “Bundling of actin filaments by alpha-actinin depends on its molecular length”. In: *The Journal of Cell Biology* 110.6 (June 1990), pp. 2013–2024. DOI: 10.1083/jcb.110.6.2013.

[54] K. M. Schmoller, O. Lieleg, and A. R. Bausch. "Cross-Linking Molecules Modify Composite Actin Networks Independently". In: *Physical Review Letters* 101.11 (Sept. 2008), p. 118102. DOI: 10.1103/PhysRevLett.101.118102.

[55] D.H. Wachsstock, W.H. Schwartz, and T.D. Pollard. "Affinity of alpha-actinin for actin determines the structure and mechanical properties of actin filament gels". In: *Biophysical Journal* 65.1 (July 1993), pp. 205–214. DOI: 10.1016/S0006-3495(93)81059-2.

[56] D.H. Wachsstock, W.H. Schwarz, and T.D. Pollard. "Cross-linker dynamics determine the mechanical properties of actin gels". In: *Biophysical Journal* 66.3 (Mar. 1994), pp. 801–809. DOI: 10.1016/S0006-3495(94)80856-2.

[57] Jérémie Barral and Pascal Martin. "The physical basis of active mechanosensitivity by the hair-cell bundle". In: *Current Opinion in Otolaryngology and Head and Neck Surgery* 19.5 (Oct. 2011), pp. 369–375. DOI: 10.1097/MOO.0b013e32834a8c33.

[58] Changsong Yang and Tatyana Svitkina. "Filopodia initiation". In: *Cell Adhesion and Migration* 5.5 (Sept. 2011), pp. 402–408. DOI: 10.4161/cam.5.5.16971.

[59] Changsong Yang and Tatyana Svitkina. "Visualizing branched actin filaments in lamellipodia by electron tomography". In: *Nature Cell Biology* 13.9 (Sept. 2011), pp. 1012–1013. DOI: 10.1038/ncb2321.

[60] J. Howard and J.F. Ashmore. "Stiffness of sensory hair bundles in the sacculus of the frog". In: *Hearing Research* 23.1 (Jan. 1986), pp. 93–104. DOI: 10.1016/0378-5955(86)90178-4.

[61] Keith Burridge and Erika S. Wittchen. "The tension mounts: Stress fibers as force-generating mechanotransducers". In: *The Journal of Cell Biology* 200.1 (Jan. 2013), pp. 9–19. DOI: 10.1083/jcb.201210090.

[62] Pirta Hotulainen and Pekka Lappalainen. "Stress fibers are generated by two distinct actin assembly mechanisms in motile cells". In: *The Journal of Cell Biology* 173.3 (May 2006), pp. 383–394. DOI: 10.1083/jcb.200511093.

[63] Damien Laporte et al. "α-Actinin and fimbrin cooperate with myosin II to organize actomyosin bundles during contractile-ring assembly". In: *Molecular Biology of the Cell* 23.16 (Aug. 2012). Ed. by Yu-Li Wang, pp. 3094–3110. DOI: 10.1091/mbc.e12-02-0123.

[64] Ulrich S. Schwarz and Margaret L. Gardel. "United we stand – integrating the actin cytoskeleton and cell–matrix adhesions in cellular mechanotransduction". In: *Journal of Cell Science* 125.13 (July 2012), pp. 3051–3060. DOI: 10.1242/jcs.093716.

[65] Colleen T. Skau et al. "Actin Filament Bundling by Fimbrin Is Important for Endocytosis, Cytokinesis, and Polarization in Fission Yeast". In: *Journal of Biological Chemistry* 286.30 (July 2011), pp. 26964–26977. DOI: 10.1074/jbc.M111.239004.

[66] Manuel Théry et al. "Cell distribution of stress fibres in response to the geometry of the adhesive environment". In: *Cell Motility and the Cytoskeleton* 63.6 (June 2006), pp. 341–355. DOI: 10.1002/cm.20126.

[67] Sari Tojkander et al. "A Molecular Pathway for Myosin II Recruitment to Stress Fibers". In: *Current Biology* 21.7 (Apr. 2011), pp. 539–550. DOI: 10.1016/j.cub.2011.03.007.

[68] George Bell. "Models for the Specific Adhesion of Cells to Cells". In: *Science* 200 (1978), pp. 618–627.

[69] Ulrich S. Schwarz and Samuel A. Safran. “Physics of adherent cells”. In: *Reviews of Modern Physics* 85.3 (Aug. 2013), pp. 1327–1381. DOI: 10.1103/RevModPhys.85.1327.

[70] E. A. Evans and D. A. Calderwood. “Forces and Bond Dynamics in Cell Adhesion”. In: *Science* 316.5828 (May 2007), pp. 1148–1153. DOI: 10.1126/science.1137592.

[71] E. Evans and K. Ritchie. “Dynamic strength of molecular adhesion bonds”. In: *Biophysical Journal* 72.4 (1997), pp. 1541–1555. DOI: 10.1016/S0006-3495(97)78802-7.

[72] Peter Hänggi, Peter Talkner, and Michal Borkovec. “Reaction-rate theory: Fifty years after Kramers”. In: *Reviews of Modern Physics* 62.2 (1990), pp. 251–341. DOI: 10.1103/RevModPhys.62.251.

[73] H.A. Kramers. “Brownian motion in a field of force and the diffusion model of chemical reactions”. In: *Physica* 7.4 (1940), pp. 284–304. DOI: 10.1016/S0031-8914(40)90098-2.

[74] T. Erdmann and U. S. Schwarz. “Impact of receptor-ligand distance on adhesion cluster stability”. In: *European Physical Journal E* 22.2 (2007), pp. 123–137. DOI: 10.1140/epje/e2007-00019-8. arXiv: 0612457 [cond-mat].

[75] T. Erdmann and U. S. Schwarz. “Stability of Adhesion Clusters under Constant Force”. In: *Physical Review Letters* 92.10 (Mar. 2004), p. 108102. DOI: 10.1103/PhysRevLett.92.108102.

[76] Thorsten Erdmann. “Stochastische Dynamik von Adhäsionsclustern unter Kraft”. In: *Dissertation* April 2005 (2005).

[77] Thorsten Erdmann and Ulrich S. Schwarz. "Stochastic dynamics of adhesion clusters under shared constant force and with rebinding". In: *The Journal of Chemical Physics* 121.18 (Nov. 2004), pp. 8997–9017. DOI: 10.1063/1.1805496.

[78] N. G. van Kampen. *Stochastic Processes in Physics and Chemistry*. Elsevier, 1992.

[79] T. A. J. Duke. "Molecular model of muscle contraction". In: *Proceedings of the National Academy of Sciences* 96.6 (Mar. 1999), pp. 2770–2775. DOI: 10.1073/pnas.96.6.2770.

[80] Andrew F Huxley. "Muscle structure and theories of contraction". In: *Prog. Biophys. Biophys. Chem* 7 (1957), pp. 255–318.

[81] Thomas Guérin et al. "Coordination and collective properties of molecular motors: theory". In: *Current Opinion in Cell Biology* 22.1 (Feb. 2010), pp. 14–20. DOI: 10.1016/j.ceb.2009.12.012.

[82] S. Klumpp and R. Lipowsky. "Cooperative cargo transport by several molecular motors". In: *Proceedings of the National Academy of Sciences* 102.48 (Nov. 2005), pp. 17284–17289. DOI: 10.1073/pnas.0507363102.

[83] Huajian Gao, Jin Qian, and Bin Chen. "Probing mechanical principles of focal contacts in cell-matrix adhesion with a coupled stochastic-elastic modelling framework." In: *Journal of the Royal Society, Interface / the Royal Society* 8.62 (2011), pp. 1217–1232. DOI: 10.1098/rsif.2011.0157.

[84] Jin Qian and Huajian Gao. "Soft Matrices Suppress Cooperative Behaviors among Receptor-Ligand Bonds in Cell Adhesion". In: *PLoS ONE* 5.8 (Aug. 2010). Ed. by Markus J. Buehler, e12342. DOI: 10.1371/journal.pone.0012342.

[85] Jin Qian, Jizeng Wang, and Huajian Gao. "Lifetime and Strength of Adhesive Molecular Bond Clusters between Elastic Media". In: *Langmuir* 24.4 (Feb. 2008), pp. 1262–1270. DOI: 10.1021/la702401b.

[86] Jin Qian et al. “Lifetime and Strength of Periodic Bond Clusters between Elastic Media under Inclined Loading”. In: *Biophysical Journal* 97.9 (Nov. 2009), pp. 2438–2445. DOI: 10.1016/j.bpj.2009.08.027.

[87] Erin M Craig et al. “Model for adhesion clutch explains biphasic relationship between actin flow and traction at the cell leading edge”. In: *Physical Biology* 12.3 (May 2015), p. 035002. DOI: 10.1088/1478-3975/12/3/035002.

[88] Margaret L. Gardel et al. “Traction stress in focal adhesions correlates biphasically with actin retrograde flow speed”. In: *The Journal of Cell Biology* 183.6 (Dec. 2008), pp. 999–1005. DOI: 10.1083/jcb.200810060.

[89] Ying Li, Prabhakar Bhimalapuram, and Aaron R Dinner. “Model for how retrograde actin flow regulates adhesion traction stresses”. In: *Journal of Physics: Condensed Matter* 22.19 (May 2010), p. 194113. DOI: 10.1088/0953-8984/22/19/194113.

[90] Manoj Srinivasan and Sam Walcott. “Binding site models of friction due to the formation and rupture of bonds: State-function formalism, force-velocity relations, response to slip velocity transients, and slip stability”. In: *Physical Review E* 80.4 (Oct. 2009), p. 046124. DOI: 10.1103/PhysRevE.80.046124.

[91] Benedikt Sabass and Ulrich S Schwarz. “Modeling cytoskeletal flow over adhesion sites: competition between stochastic bond dynamics and intracellular relaxation”. In: *Journal of Physics: Condensed Matter* 22.19 (May 2010), p. 194112. DOI: 10.1088/0953-8984/22/19/194112.

[92] A. E. Filippov, J. Klafter, and M. Urbakh. “Friction through Dynamical Formation and Rupture of Molecular Bonds”. In: *Physical Review Letters* 92.13 (Mar. 2004), p. 135503. DOI: 10.1103/PhysRevLett.92.135503.

[93] A. Schallamach. “A theory of dynamic rubber friction”. In: *Wear* 6.5 (Sept. 1963), pp. 375–382. DOI: 10.1016/0043-1648(63)90206-0.

[94] Benjamin L. Bangasser and David J. Odde. “Master Equation-Based Analysis of a Motor-Clutch Model for Cell Traction Force”. In: *Cellular and Molecular Bioengineering* 6.4 (Dec. 2013), pp. 449–459. DOI: 10.1007/s12195-013-0296-5. arXiv: NIHMS150003.

[95] Clarence E. Chan and David J. Odde. “Traction Dynamics of Filopodia on Compliant Substrates”. In: *Science* 322.5908 (Dec. 2008), pp. 1687–1691. DOI: 10.1126/science.1163595.

[96] Pierre Sens. “Rigidity sensing by stochastic sliding friction”. In: *EPL (Europhysics Letters)* 104.3 (2013), p. 38003. DOI: 10.1209/0295-5075/104/38003. arXiv: arXiv:1310.8165v1.

[97] M Caruel. “Mechanics of Fast Force Recovery in striated muscles”. In: (2012).

[98] M. Caruel, J.-M. Allain, and L. Truskinovsky. “Mechanics of collective unfolding”. In: *Journal of the Mechanics and Physics of Solids* 76 (2015), pp. 237–259. DOI: 10.1016/j.jmps.2014.11.010.

[99] Matthieu Caruel, J.-M. Allain, and Lev Truskinovsky. “Muscle as a Metamaterial Operating Near a Critical Point”. In: *Physical Review Letters* 110.24 (June 2013), p. 248103. DOI: 10.1103/PhysRevLett.110.248103. arXiv: 1305.5094.

[100] R Erban, J Chapman, and P Maini. “A practical guide to stochastic simulations of reaction-diffusion processes”. In: *arXiv preprint arXiv:0704.1908* (2007), p. 35. arXiv: 0704.1908.

[101] Daniel T. Gillespie. “Exact stochastic simulation of coupled chemical reactions”. In: *The Journal of Physical Chemistry* 81.25 (Dec. 1977), pp. 2340–2361. DOI: 10.1021/j100540a008.

[102] Samuel Karlin and Howard E. Taylor. *A First Course in Stochastic Processes: Second Edition*. Elsevier, 2012, pp. 1–557. DOI: 10.1016/C2009-1-28569-8.

[103] Luc Devroye. "Chapter 4 Nonuniform Random Variate Generation". In: *Handbooks in Operations Research and Management Science*. Vol. 13. C. 2006, pp. 83–121. DOI: 10.1016/S0927-0507(06)13004-2.

[104] Joseph R. Lakowicz. *Principles of Fluorescence Spectroscopy*. Ed. by Joseph R. Lakowicz. third edit. Boston, MA: Springer US, 2006. DOI: 10.1007/978-0-387-46312-4.

[105] Barbara Lynch. "Multiscale biomechanics of skin : experimental investigation of the role of the collagen microstructure". PhD thesis. Ecole Polytechnique, 2015, p. 196.

université PARIS-SACLAY
ÉCOLE DOCTORALE
INTERFACES
Approches Interdisciplinaires : Fondements, Applications et Innovation

Titre : Mécanique multi-échelles des tissus mous

Mots clés : tissus mous; mécanique; réseaux de fibres; microstructure; simulation stochastique; physique statistique

Résumé : Les réseaux de fibre sont une structure omniprésente dans les tissus biologiques, aussi bien au niveau macroscopique, où ils sont l'ingrédient principal des tissus mous, qu'au niveau microscopique, en tant que constituants des structures collagèniques ou du cytosquelette. L'objectif de ce travail de thèse est de proposer un modèle basé sur la microstructure physique des réseaux de fibres afin d'obtenir une compréhension du comportement mécanique des réseaux de fibres biologiques. Le modèle est basé sur une description de fibres glissant les unes par rapport aux autres et interagissant via des ponts qui se comportent comme des ressorts. Ces ponts peuvent s'attacher et se détacher de manière stochastique avec un taux de détachement qui dépend de la force subie. Comparé aux modélisations existantes, notre travail met en jeu une configuration en glissement dynamique des fibres, ainsi que des sites d'attachement discrets ne permettant l'attachement qu'à des endroits localisés de la fibre. Le détachement des ponts est basé sur la diffusion thermique hors d'un puit de potentiel suivant la théorie de Kramers. Cette théorie donne un contexte physique à la dynamique du détachement ainsi qu'une dépendance naturelle du détachement au chargement via l'inclinaison du paysage énergétique par la force de chargement. Le modèle donne deux modes de contrôle du système : un contrôle à vitesse imposée, appelé système dur, et un contrôle à force imposée, appelé système mou. Notre travail permet également de visualiser le comportement du système à travers une simulation stochastique. Les simulations offrent deux algorithmes, chacun adapté à la méthode de contrôle du système, en système dur ou mou et respectant la causalité dans chacun des modes. Les résultats de la simulation sont explorés via la visualisation des données sortantes de la simulation, qui servent de support pour l'investigation paramétrique du comportement du modèle et ancrent l'interprétation physique des résultats. En particulier, l'influence de l'espacement des sites d'attachement du système, un point caractéristique du modèle, est examiné. De même, nous explorons l'effet de chargements complexes (transitoires, cycliques, etc.) qui représentent les chargements physiologiques des tissus fibreux.

Title : Multi-scale mechanics of soft tissues

Keywords : soft tissues, mechanics; fiber networks; microstructure; stochastic simulation; statistical mechanics

Abstract : Fibre networks are ubiquitous structures in biological tissues, both at the macroscopic level being the main ingredient in soft tissues and at the microscopic level, as constituents of collagen structures or the cytoskeleton. The goal of this work is to propose a model based on the physical microstructure of fibre networks in order to provide an understanding of the mechanical behaviour of biological fibre networks. The current model starts from fibres sliding with respect to one another and interacting via spring-like cross-bridges. These cross-bridges can attach and detach stochastically with a load-dependent detachment rate. Compared to existing modelling approaches, this work features a dynamic sliding configuration for the interacting fibres and discrete binding sites which permit attachment on localised spaces of the fibre. The detachment of cross-bridges is based on thermal diffusion out of an energy well, following the Kramers rate theory. This theory provides a physical background to the detachment dynamics as well as a natural load dependency in the tilting of the energy landscape by the load force. The model provides two modes by which the depicted system may be driven: an imposed velocity driving, called a hard device and an imposed load driving, called a soft device. The work also provides a way of visualising the behaviour of the model by performing a stochastic simulation. The simulations provided present two algorithms, each tailored to represent the driving of the system, whether in hard or soft device, respecting the causality in each of the driving mode. Simulation results are explored via data visualisation of simulation output. These visualisation serve as an entry point into parametric investigation of the model behaviour and anchor the interpretation of the results into physical systems. In particular, the influence of binding site spacing, one of the key features of the model, is investigated. We also investigate the effects of complex loading paths (transitory, cyclic, etc.) which can be associated to the physiological loadings fibrous tissues.

Université Paris-Saclay
Espace Technologique / Immeuble Discovery
Route de l'Orme aux Merisiers RD 128 / 91190 Saint-Aubin, France